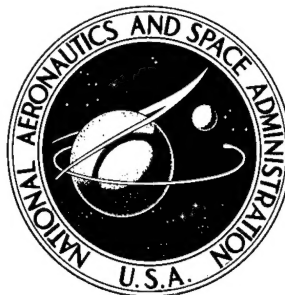


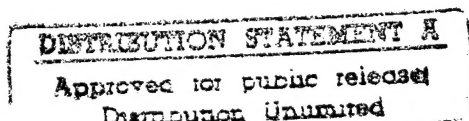
6/11/70
Keep

NASA TECHNICAL NOTE



NASA TN D-5833

NASA TN D-5833



APPROXIMATE ANALYTICAL MODELS
FOR LANDING ENERGY ABSORPTION,
INCLUDING THE EFFECT OF
PENETRATION BY THE PAYLOAD
INTO ITS CRUSHABLE CASING

by Robert W. Warner
Ames Research Center
Moffett Field, Calif. 94035

19960503 100

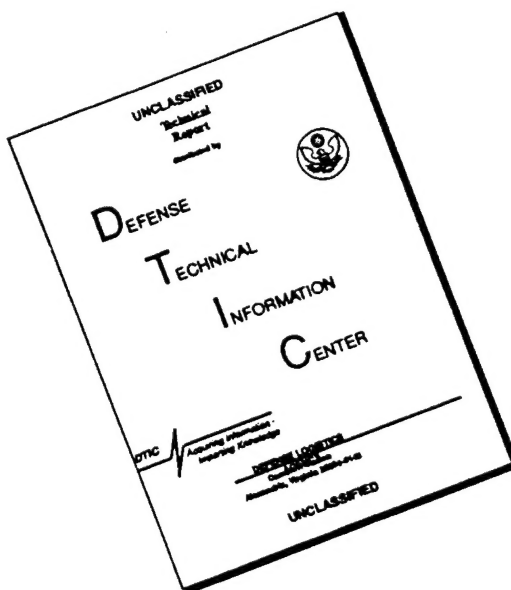
DTIC QUALITY INSPECTED 1

NATIONAL AERONAUTICS AND SPACE ADMINISTRATION • WASHINGTON, D. C. • JUNE 1970

DEPARTMENT OF DEFENSE
PLASTICS TECHNICAL EVALUATION CENTER
PICATINNY ARSENAL, DENV. N. J.

PLASTEC/4284

DISCLAIMER NOTICE



THIS DOCUMENT IS BEST QUALITY AVAILABLE. THE COPY FURNISHED TO DTIC CONTAINED A SIGNIFICANT NUMBER OF PAGES WHICH DO NOT REPRODUCE LEGIBLY.

1. Report No. NASA TN D-5833		2. Government Accession No.		3. Recipient's Catalog No.	
4. Title and Subtitle APPROXIMATE ANALYTICAL MODELS FOR LANDING ENERGY ABSORPTION, INCLUDING THE EFFECT OF PENETRATION BY THE PAYLOAD INTO ITS CRUSHABLE CASING				5. Report Date June 1970	
				6. Performing Organization Code	
7. Author(s) Robert W. Warner				8. Performing Organization Report No. A-3335	
9. Performing Organization Name and Address NASA Ames Research Center Moffett Field, Calif. 94035				10. Work Unit No. 124-08-05-08-00-21	
				11. Contract or Grant No.	
12. Sponsoring Agency Name and Address National Aeronautics and Space Administration Washington, D. C., 20546				13. Type of Report and Period Covered Technical Note	
				14. Sponsoring Agency Code	
15. Supplementary Notes					
16. Abstract <p>Two approximate analytical models are defined for a landing configuration in which a spherical payload can sometimes penetrate into its crushable casing. Results for both models are found to agree reasonably well with two previous experimental measurements. Design examples are presented for an impact velocity of 300 ft per sec. These are based on choices of zero or "perfect" payload bonding, and of either a balsa-like or honeycomb-like class of crushable material. The greatest difference between the models for these examples is a 29-percent discrepancy in the required maximum crushing stress. A particular pair of examples gives the unexpected result that penetration can provide a decrease in crushable material weight by a factor greater than 4 when the honeycomb-like class of material is required without penetration, but the more efficient balsa-like class is feasible with penetration.</p>					
17. Key Words Suggested by Author Landing impact energy absorption Planetary landing (unmanned) Structural mechanics Materials, metallic Materials, nonmetallic				18. Distribution Statement Unclassified - Unlimited	
19. Security Classif. (of this report) Unclassified		20. Security Classif. (of this page) Unclassified		21. No. of Pages 93	
				22. Price* \$ 3.00	

*For sale by the Clearinghouse for Federal Scientific and Technical Information
Springfield, Virginia 22151

TABLE OF CONTENTS

	<u>Page</u>
NOTATION	v
SUMMARY	1
INTRODUCTION	1
OUTLINE OF THEORY	2
Properties of Typical Crushable Material	2
Summary of Fundamental Assumptions and Limitations	3
Summary of Analytical Development	5
DESIGN PROCEDURES FOR SPHERICAL GEOMETRY	6
General Design Conditions	6
Design Procedure for Simplified Model Without Payload Penetration	9
Design Procedure for Simplified Model With Payload Penetration	11
Specialization of Design Procedures for Simplified Model to Materials of Figure 5.	13
Computer Procedures	14
Design Procedure for Detailed Model With and Without Payload Penetration	15
DESIGN RESULTS AND DISCUSSION FOR SIMPLIFIED AND DETAILED MODELS HAVING SPHERICAL GEOMETRY	16
Description of Design Examples and Most General Results	16
Effect of Payload Radius (and Payload Packaging Density) for Balsa-like and Honeycomb-like Materials Without Payload Penetration	17
Effect of Payload Penetration	18
Comparison With Previous Analytical Models	20
Comparison With Previous Experiments	21
Alternate Models	22
CONCLUDING REMARKS	23
APPENDIX A - DEVELOPMENT OF BASIC EQUATIONS	25
GENERAL GOVERNING EQUATIONS	25
GOVERNING EQUATIONS FOR ZERO SHEAR DEFORMATION, UNIFORM COMPACTING STRAIN, AND UNIFORM MATERIAL DENSITY	28
EVALUATION OF VOLUME AND STRESS INTEGRALS FOR SPHERICAL GEOMETRY	32
Dimensionless Governing Equations for Spherical Geometry, With Termination Conditions	37
Simplifications for Constant Mass, Infinitely Thin Crushed Material, and/or Constant Penetration Resistance	41
APPENDIX B - SAMPLE CALCULATION FOR DESIGN BY SIMPLIFIED MODEL WITHOUT PAYLOAD PENETRATION	45

TABLE OF CONTENTS - Concluded

	<u>Page</u>
APPENDIX C - SAMPLE CALCULATION FOR DESIGN BY SIMPLIFIED MODEL WITH PAYLOAD PENETRATION	49
APPENDIX D - COMPUTER PROCEDURES FOR THE GOVERNING EQUATIONS WITH SPHERICAL GEOMETRY	52
BASIC COMPUTER PROCEDURE	52
SEARCH FOR OVERALL RADIUS R	54
SEARCH FOR OVERALL RADIUS R AND CRUSHING STRESS σ_0	55
APPENDIX E - EXACT INTEGRATION FOR A CLASS OF IMPACT PROBLEMS WITH VARIABLE MASS BUT WITHOUT PAYLOAD PENETRATION	58
REFERENCES	60
TABLE 1.- NUMERICAL RESULTS FOR $U_0 = 300$ FT/SEC, $\epsilon_d = 0.7$, $\epsilon_m = 0.8$, AND $n_{p_{max}} \leq 2000$	62
FIGURES	65

NOTATION

A	dummy integration variable for area
A_{c1}	surface area between the mass of material compacted by the landing surface and the mass of uncrushed crushable material
A_{c1h}	horizontal planar projection of A_{c1}
A_{po}	surface area of lower portion of payload over which shear and/or normal stresses act to decelerate payload
A_{poh}	horizontal planar projection of A_{po} and, in the absence of shear effects, A_{p1}
A_{p1}	surface area between the mass of material compacted by the payload and the mass of uncrushed crushable material
A_{sh}	horizontal cross-sectional area in the volume V_c of figures 3 and 4 (the volume that would lie beneath the landing surface if there had been no crushing)
b	dimensional dummy integration variable used in equation (A27); $\equiv \sqrt{R^2 - r^2}$
b_p	dimensional dummy integration variable used in equation (A29); $\equiv \sqrt{R_p^2 - r_p^2}$
e	dimensionless variable describing the relative motion of payload penetration; defined as $\frac{q_p - q}{\epsilon_k R_p}$ in equation (A39)
e_{max}	maximum value of e during payload penetration
$F_{c1}(y)$	identical to $F_{c1}(z)$ if $\frac{R_p}{R} y$ is substituted for z
$F_{c1}(z)$	dimensionless vertical crushing force acting over area A_{c1} and tending to decelerate the mass above A_{c1} ; defined in equation (A36)
$F_{po}(e)$	dimensionless vertical crushing force acting over area A_{p1} and tending to decelerate the mass above A_{p1} ; defined in equation (A45)
g	general symbol for acceleration due to gravity
g_e	value of g on earth (32.17 ft/sec ² herein)
g_L	value of g at the landing site (12.3 ft/sec ² herein)

h_c	local height of the volume which would lie beneath the landing surface if there had been no crushing; the local height of V_c ; see figures 2, 3, and 4
h_{c1}	local height of the compacted volume of material compacted by the landing surface; the local height of m_{c1} ; defined in equation (A12); see figures 2, 3, and 4
h_{p1}	local height of the compacted volume of material compacted by the payload; the local height of m_{p1} ; defined in equation (A12); see figures 2, 3, and 4
$J_{m\sigma}$	defined in equation (17) as $\left(\frac{g_e(\text{SEA})}{U_o^2}\right)\left(\frac{\epsilon_d}{\epsilon_m}\right)\left(\frac{m_{co}}{m_{po} + m_{co}}\right)$
j	dummy integration variable for z in equations (A37) and (A49)
K_p	defined in equation (A39) as $\frac{\pi R_p^2 \sigma_o}{m_{po} n_{md} g_e}$
K_R	defined in equation (A33) as $\frac{\pi R^2 \sigma_o}{m_{po} n_{md} g_e}$
L	distance between the fictitious compacted region determined by ϵ_d on the landing surface and that on the payload (or the payload itself, in the absence of penetration); evaluated in equation (5)
ℓ	variable used as $d\ell$ to define a length element of a rod of crushable material; used in developing equation (A11)
m_{co}	original mass of uncrushed crushable material; see figures 2(a), 3(a), and 4(a)
m_{c1}	mass of material compacted by the landing surface; mass of V_{c1} ; see figures 2 through 4
m_{po}	mass of payload; see figures 2 through 4
m_{p1}	mass of material compacted by the payload; see figures 2(c), 3(c), 4(c)
\dot{m}_{p1}	first time derivative of m_{p1}
$m(z)$	dimensionless mass defined in equation (A34) as $\frac{m_{po} + m_{co} - m_{c1}}{m_{po}}$
$m_{cr}(y,e)$	dimensionless mass defined in equation (A44) as $\frac{m_{co} - m_{c1} - m_{p1}}{m_{po}}$

$m_{pen}(e)$	dimensionless mass defined in equation (A42) as $\frac{m_{po} + m_{p1}}{m_{po}}$
N_{RU}	defined in equation (23) as $\frac{R_p}{R} \left(1 + \frac{U_o^2}{2\epsilon_d n_{pmax} g_e R_p} \right)$
N_{mu}	defined in equation (24) as $\frac{1 + (m_{co}/m_{po})}{[1 + (U_o^2/2\epsilon_d n_{pmax} g_e R_p)]^2}$
$N_{m\sigma}$	defined in equation (25) as $\frac{W_{co}}{(\rho_{cm} g_e) \pi R_p^3}$ (see also eq. (26) for payload penetration with the simplified design)
n_{des}	desired value of n_{pmax}
n_{md}	maximum permissible value of n_{pmax} (2000 herein)
n_p	g loading with $n_p g_e$ as the payload deceleration
n_{pmax}	maximum value of n_p that occurs during impact stroke
q	absolute displacement of uncrushed crushable material after initial contact with landing surface; see figures 2 through 4
\dot{q}, \dot{q}_p	first time derivatives of q and q_p
\ddot{q}, \ddot{q}_p	second time derivatives of q and q_p
q_p	absolute displacement of payload after initial contact between crushable material and landing surface; $q_p = q$ in absence of payload penetration; see figures 2 through 4
q_{max}, q_{pmax}	values of q and q_p at end of impact stroke
q_s	value of q ($q = q_p$) at which payload penetration occurs or would occur if unbonded
R	overall radius for spherical system
R_p	payload radius for spherical system
r	polar radial coordinate of point in A_{c1} , where coordinate is measured in a horizontal cross section for spherical geometry; see figure 4(b) and equation (A25)
r_p	polar radial coordinate of point in A_{p1} , where coordinate is measured in a horizontal cross section for spherical geometry; see figure 4(c)

SEA	specific energy absorption; energy absorbed per unit weight of the absorber; defined in equation (8) in terms of the variables used herein
s	dimensionless dummy integration variable used in equation (A36); $\equiv \frac{b}{R}$
s _p	dimensionless dummy integration variable used in equation (A45); $\equiv \frac{b_p}{R_p}$
t	time; used for time derivative interchangeably with dot
U	velocity of the uncrushed crushable material; defined in equation (A16) as $\dot{q} \equiv \frac{dq}{dt}$
U ₀	value of U at the instant the crushable material hits the landing surface (300 ft/sec herein)
V _c	volume that would lie beneath the landing surface if there had been no crushing; shown in figures 3 and 4; defined in equation (A14)
V _{cmax} , V _{c1max}	maximum values of V _c and V _{c1} , that is, the values reached at the end of the impact stroke
V _{c1}	compacted volume of material compacted by the landing surface; the volume of m _{c1}
V _p	volume swept out by the payload as a result of the relative motion of penetration; defined in equation (A14)
V _{p1}	compacted volume of material compacted by the payload; the volume of m _{p1}
v	dimensionless velocity of the uncrushed crushable material; defined in equation (A54) as $\frac{dq/dt}{\sqrt{n_{md}g_e R_p}} \equiv \frac{U}{\sqrt{n_{md}g_e R_p}} \equiv \frac{dy}{dx} \equiv w \sqrt{\frac{R}{R_p}}$
v ₀	value of v at the instant the crushable material hits the landing surface
v _p	dimensionless velocity of the payload; defined in equation (A54) as $\frac{dq_p/dt}{\sqrt{n_{md}g_e R_p}} \equiv \epsilon_k \frac{de}{dx} + \frac{dy_p}{dx} \equiv \frac{dy_p}{dx}$
v _s	value of v at the start of payload penetration, if any

W_{co}	original earth weight of uncrushed crushable material, $m_{co}g_e$
W_{po}	earth weight of payload, $m_{po}g_e$
w	dimensionless velocity of the uncrushed crushable material; defined in equation (A33) as $\frac{U}{\sqrt{n_{md}g_e R}}$
w_0	value of w at the instant the crushable material hits the landing surface
w_s	value of w at the start of payload penetration, if any
x	dimensionless time; defined in equation (A39) as $t \sqrt{\frac{n_{md}g_e}{R_p}}$
y	dimensionless displacement defined in equation (A39) as $\frac{q}{R_p} \equiv z \frac{R}{R_p}$
y_p	dimensionless payload displacement defined in equation (A54) as $\frac{q_p}{R_p} \equiv \epsilon_k e + y$
y_{max}, y_{pmax}	values of y and y_p at end of impact stroke
y_s	value of y at the start of payload penetration, if any
z	dimensionless displacement defined in equation (A33)
z_a	value of z at $n_p = n_{pmax}$
z_{max}	value of z at end of impact stroke
z_{pmax}	$\frac{q_{pmax}}{R}$
z_s	value of z at the start of payload penetration, if any
α	angle between normal to stressed area and direction of maximum normal crushing stress
β	$\frac{n_{pmax}}{n_{des}} - 1$
ϵ	compacting strain of crushable material; more detailed definition given following equation (1)

ϵ_d	fictitious value of ϵ_k assumed for design purposes; always less than ϵ_m
ϵ_k	compacting strain when it is uniform throughout hypothetical crushable material; ϵ_k determines the surface for stress evaluation and can be specialized in governing equations for simplifying approximations
ϵ_m	value of ϵ_k for actual crushable material (0.8 herein)
θ_p	angle shown in figure 4(c) and used in derivation of equation (A28)
ξ	dummy integration variable for y
ρ_{ck}	uniform density of hypothetical crushable material in swept-out volumes such as V_c in figure 4; ρ_{ck} can be specialized as zero to neglect variable mass without implying a massless crushable casing
ρ_{cm}	uniform density of actual crushable material
ρ_p	payload packaging density; defined in equation (A43) as $\frac{m_{po}}{(4/3)\pi R_p^3}$
ρ_{pR}	defined in equation (A35) as $\frac{m_{po}}{(4/3)\pi R^3}$
σ	"mostly normal" and "mostly static" crushing stress of crushable material, averaged over maximum possible stroke prior to compacting
σ_o	maximum of σ as defined in equations (2) and (A24)
σ_{po}	normal stress on the payload prior to penetration
σ_{pok}	σ_{po} under assumption $\sigma_{po} = \sigma_{pok} = \text{constant}$
σ_v	vertical component of σ
σ_v'	dynamic value of σ_v as defined following equation (A7)
σ_{vpo}	vertical component of normal stress on the payload
ϕ	angle shown in figure 4(b) and used in derivation of equation (A27)
ϕ_p	angle shown in figure 4(c) and used in derivation of equation (A28)

APPROXIMATE ANALYTICAL MODELS FOR LANDING ENERGY ABSORPTION,
INCLUDING THE EFFECT OF PENETRATION BY THE PAYLOAD
INTO ITS CRUSHABLE CASING

Robert W. Warner

Ames Research Center

SUMMARY

Two approximate analytical models are defined for a landing configuration in which a spherical payload can sometimes penetrate into its crushable casing. Results for both models are found to agree reasonably well with two previous experimental measurements. Design examples are presented for an impact velocity of 300 ft/sec. These are based on choices of zero or "perfect" payload bonding, and of either a balsa-like or honeycomb-like class of crushable material. The greatest difference between the models for these examples is a 29-percent discrepancy in the required maximum crushing stress. A particular pair of examples gives the unexpected result that penetration can provide a decrease in crushable material weight by a factor greater than 4 when the honeycomb-like class of material is required without penetration, but the more efficient balsa-like class is feasible with penetration.

INTRODUCTION

One means proposed for providing information on lunar and planetary surfaces consists of an unmanned instrumentation system that is hard landed (with or without terminal guidance) but designed to survive the impact. For such a landing, a crushable casing is one means for absorbing landing energy so the payload can survive and transmit information during and after the impact. The advantage of this approach depends greatly on how light the crushable casing can be made for a given impact velocity.

Various aspects of the design of crushable casings have been investigated in references 1 through 9, but without including the effect of penetration by the payload into the casing. The primary purpose of the present paper is to evaluate that effect analytically. For this purpose, fairly general equations of motion are derived for the payload and the crushable material. These equations are then specialized for two approximate analytical models in which the payload and casing are spherical. The analytical models will be used in a number of design examples so that the effect of payload penetration can be evaluated and also one model compared with the other. The two models will also be compared with earlier models that do not permit penetration and with the test results of reference 10 and a private communication.¹

¹Donald R. Cundall, December 1967.

OUTLINE OF THEORY

Properties of Typical Crushable Material

Material properties are an essential input to the theoretical development. A typical crushable material for landing impact energy absorption has a stress-strain curve similar to curve ABCDE in figure 1(a). The material is elastic from point A to point B, and there is rebound between points D and E. (The rebound should be as small as possible.) Between points B and D there is a large volume change; and the crushing stress is relatively constant, with an average value σ indicated by the horizontal dotted line in figure 1(a). Point C, where the crushing stress begins to rise abruptly, is called the compacting strain ϵ and ranges from 0.6 for close-packed crushable materials to nearly 1.0 for open crushable structures.

The area enclosed by the stress-strain curve ABCDE is the energy absorbed per unit volume of crushable material. This energy is maximized for a maximum permissible crushing stress (which determines the maximum landing vehicle deceleration for a given configuration) if the stress-strain curve approaches a rectangle. Hence the material is not strained beyond point D in figure 1(a), where the stress is equal to the prior maximum (point B), even though the stress could go higher as shown. If the initial peak at B is too high to approximate a rectangle, it can sometimes be reduced by precrushing. A less desirable alternative is to accept the stress-strain curve but modify the load-deflection curve by changing the shape of the crushable material.

Stress-strain and load-deflection curves for balsa wood, plastic foam, and honeycomb are given in references 11 through 14. These curves have been determined by dynamic crushing tests and by nearly static tests of specimens having uniform cross sections. Figure 1(b) is a sketch of a crushing test in which the specimen is compressed uniformly across the cross section by a plate, and figure 1(c) shows a test in which the specimen is penetrated by a plunger. In both tests, the material crushes in layers at a loaded surface, which may be at either end of the specimen in the case of the plate loading.

It should be noted that a certain (exaggerated) amount of material is shown trailing outboard of the plunger in figure 1(c) due to shear resistance. This shear effect, as well as friction, causes a difference in the crushing loads of figures 1(b) and 1(c). In the case of balsa wood, however, reference 7 indicates that this difference is small, while reference 13 indicates that it ranges from 5 to 15 percent (for a range of plunger sizes).

It should also be noted that dynamic and nearly static crushing tests give different results. In fact, references 11 and 13 suggest ratios of static to dynamic crushing stress from 0.69 to 0.73 for various materials. Since the maximum velocity in the dynamic tests was 108 ft/sec, the dynamic effect is probably not due to variable mass (i.e., the accumulation of crushed material at a loaded surface) but rather due to damping and dynamic buckling (i.e., coupling between vertical and horizontal velocity). Unfortunately, the effects of higher velocities on damping and dynamic buckling are not established for the present materials.

Summary of Fundamental Assumptions and Limitations

In contrast to the typical material just discussed, the material assumed for theoretical analysis has a perfectly rectangular stress-strain curve (a so-called "rigid plastic" shape). This curve is represented by the dashed lines in figure 1(a). It is shown bounded by the compacting strain ϵ and the average crushing stress σ of the typical material. In this case, the energy absorbed per unit volume will not match that of the typical material perfectly, but the boundaries of the rectangle can be adjusted slightly if need be.

There are a number of other analytical assumptions that pertain to the crushable material, and there are several that do not. For convenience, all fundamental assumptions and limitations are listed in the present section as follows:

1. Rebound is assumed absent.
2. It is assumed that the effects of shear resistance, end fixity, and Poisson's ratio are adequately incorporated in the analysis because of their presence in the crushing tests that determine the so-called "mostly normal" and "mostly static" crushing stress (σ , σ_0 , and σ_v ; see Notation).
3. The "mostly normal" and "mostly static" crushing stress σ is also assumed to incorporate the dynamic effects of damping and dynamic buckling. This means that dynamic tests should be used to determine σ (or static dynamic ratios, such as those deduced earlier from references 11 and 13, should be applied). The velocities in the dynamic tests should not be large enough, however, to cause significant variable-mass effects, which are incorporated (when desired) in the present equations of motion.
4. Shear deformations, such as the trailing of material outboard of the plunger in figure 1(c), are neglected.
5. Separate vertical rods of material are assumed to crush vertically in the energy-absorbing process.
6. The material is assumed to compress to the same compacted strain along any axis, regardless of the axis of maximum normal crushing stress.
7. It is assumed that each particle in the uncrushed crushable material is moving at the same vertical velocity at a given instant and that the crushed material also has a uniform particle velocity, but a different one from that of the uncrushed material. This implies the following corollary assumptions:
 - a. Each successive layer of crushable material undergoes a jump in velocity as it moves from the uncrushed to the crushed region.

- b. The elastic stress waves that established the uniform velocities must travel far faster than those velocities (i.e., the uniform velocities are subsonic).
 - c. The deformation waves resulting from the elastic stress waves must be small enough not to affect the uniform velocities.
8. For landing geometries in which there is doubt as to where the crushing by layers will start, it is assumed to start at the impacted end of the crushable material (in keeping with experimental observations, except at certain impact velocities too low to be of interest). Thus, if figures 1(b) and 1(c) were considered to represent impact tests, the location shown for the crushed material requires that the material has been impacted by the plate or the plunger. If the crushable material had impacted the landing surface in figure 1(c), with the plunger resting on top of the material, there would have to be some crushing at the landing surface in conjunction with the plunger penetration (or "payload penetration").
 9. It is assumed that there is no section of crushable material weak enough to permit penetration by any crushable material (i.e., penetration by anything but the payload). The validity of this assumption is investigated in a later section.
 10. The density of the crushable material is assumed uniform in the uncrushed condition.
 11. The compacting strain of the crushable material is assumed uniform.
 12. Pure vertical translation is assumed.
 13. The analysis neglects all ringing and focusing of stress waves.
 14. A weightless exterior cover for the crushable material is assumed that is strong enough to prevent shattering of the crushable material. (For comparison with the experimental results of Cundall and of reference 10, however, the mass of the cover employed is assumed uniformly dispersed throughout the crushable material.)
 15. When there is payload penetration, that is, relative motion between the payload and the crushable material, the two are assumed perfectly unbonded. This rules out the interesting design possibility of penetration despite bonding and means there is no need to include the effect of tensile stresses over the upper surface of the payload.
 16. It is assumed that the landing surface is perfectly flat and perfectly rigid.
 17. Perfect rigidity is assumed for the payload.

Summary of Analytical Development

The general vertically symmetrical landing geometry without tipover or horizontal velocity is illustrated in figures 2 and 3, which are used for developing the governing equations and for the definition of terms. (Note that with gravity terms being small, "vertical" can be any direction that is both parallel to the resultant impact velocity and normal to the landing surface.) In figure 2 the major limiting assumption is the absence of shear deformation (i.e., there is no compacted material dragged outboard of the payload and no compacted material lifted off the landing surface).

Evaluation of the stress integrals and variable masses in the governing equations is greatly facilitated by introducing the compressive compacting strain ϵ and assuming that it is uniform throughout the crushable material, that is,

$$\epsilon = \epsilon_k = \text{constant} \quad (1)$$

Figure 3 shows the general vertically symmetrical landing geometry for zero shear deformation and the assumption of equation (1). The latter assumption is illustrated by the fact that h_{p1} is constant and m_{c1} is a foreshortened image of V_c .

Figure 4 specializes the geometry to concentric spheres (although most of the resulting simplifications would be realized as well by concentric spherical segments).² It is further assumed that the crushable material has a specific direction for maximum normal crushing stress, that the material has been segmented and oriented to make that direction radial, and that stressed areas with normals differing by an angle α from that radial direction feel normal stresses σ determined by the law

$$\sigma = \sigma_0 \cos \alpha, \quad \alpha < 90^\circ \quad (2)$$

where the restriction $\alpha < 90^\circ$ is required since the load has to be transferred from the lower to the upper hemisphere of crushable material, and where the restriction is automatically met in all calculations for nonzero payload radius. (See ref. 5 for alternate anisotropic relationships.)

Governing equations corresponding to the summary just given are developed in appendix A. They are specialized for various combinations of the following independent assumptions:

1. Neglect of variable mass effect. In this assumption the accumulation of crushed casing material on the payload and/or the landing surface is neglected. The assumption is accomplished by setting $\rho_{ck} = 0$.

²The spheres were selected because of their ability to absorb impact energy in any direction (i.e., to handle unoriented impacts). Such impacts may occur due to aerodynamically unstable landing configurations, a strong lateral wind with a steep landing surface, or terminal guidance failure or absence.

2. Neglect of built-up material effect. In this assumption stresses are evaluated at the surface of infinitely thin sheets of crushed material rather than built-up volumes. The assumption is accomplished by setting $\epsilon_k = 1$.
3. Neglect of variable resistance to payload penetration. In this assumption the stress and force on the payload retain their initial penetration value for the entire penetration stroke. The assumption is accomplished by setting $F_{po}(e) = 1$.

Appendix A is presented because a relatively complete theoretical development, including variable mass, built-up material, and payload penetration, is needed in the literature. The development is relegated to an appendix because the details are not needed to understand the rest of the report. If the reader wishes to locate a specific result or derivation, he can refer to the various subdivisions of appendix A listed in the Table of Contents.

DESIGN PROCEDURES FOR SPHERICAL GEOMETRY

General Design Conditions

The zero-velocity termination conditions defining the end of impact are equations (A46) and (A47). For a minimum weight design, the termination conditions should occur when the payload or the compacted material built up on it (in the case of payload penetration) touches the compacted material built up on the landing surface, that is, when the sphere of radius R_p touches the region mc_1 in figure 4(b) or when the two compacted regions touch in figure 4(c). The size of the compacted regions is based on the true material compacting strain ϵ_m . The quantity ϵ_m is identical to the ϵ_k of equation (1) except for the optional use of fictitious values for ϵ_k in the equations of motion of appendix A. If a margin of safety is desired, larger compacted regions can be envisioned on the basis of a fictitious design compacting strain called ϵ_d , where

$$\epsilon_d < \epsilon_m \quad (3)$$

If L is defined as the distance between the fictitious compacted regions at the end of the impact stroke, or between one such region and the payload, then the design condition for contact is

$$L = \frac{L}{R} = \frac{L}{R_p} = 0 \quad (4)$$

where R_p is the payload radius and R the overall radius. With ϵ_k replaced by ϵ_d , it can be deduced from equations (A12) and figure 4 that

$$L = R - R_p - \frac{q_{pmax}}{\epsilon_d} \quad (5)$$

where $q_{p_{\max}}$ is the maximum absolute payload displacement during impact.

If q_{\max} is the corresponding displacement of the uncrushed crushable material, then $q_{p_{\max}} = q_{\max}$ in the absence of payload penetration. When

$L > 0$, the process is physically realizable, although not a minimum weight design for the present spherical geometry. When $L < 0$, the process is not physically realizable; but cases for $L < 0$ may be recorded in the process of seeking $L = 0$.

A second design condition, having a less obvious relation to minimum weight design, is concerned with the maximum design deceleration $n_{md}g_e$, where g_e is the acceleration due to gravity on earth and n_{md} the maximum design g loading. If $n_{p_{\max}}g_e$ is the actual payload maximum deceleration, the design condition is

$$\frac{n_{p_{\max}}}{n_{md}} \leq 1 \quad (6)$$

For certain types of energy absorbing material or structure, the minimum weight design calls for

$$\frac{n_{p_{\max}}}{n_{md}} = 1 \quad (7)$$

For other types, any value of $n_{p_{\max}}/n_{md}$ satisfying equation (6) may yield a minimum weight design, with the critical parameter being a property of the crushable casing (such as σ_0).

The quantity $n_{p_{\max}}/n_{md}$ in equations (6) and (7) is the maximum of the quantity n_p/n_{md} in equations (A32) and (A41). (See also eqs. (A48), (A51), (A55), and (A59) for various specializations.) If variable mass and built-up material are neglected in the analysis (by setting $\rho_{ck} = 0$ and $\epsilon_k = 1$, respectively), then $n_{p_{\max}}$ occurs at $q = q_p = R/2$ in the absence of payload penetration, providing q or q_p becomes that large.

A minimum weight design is sought for a given payload mass, m_{po} , payload radius, R_p , impact velocity, U_0 , design compacting strain, ϵ_d , and maximum permissible g loading, n_{md} , with the material choice being arbitrarily limited to two classes of crushable material. Where equation (7) gives the minimum weight design, the quantities to be determined are the overall radius, R , the maximum normal stress, σ_0 , and the density, ρ_{cm} , of the crushable material (from which the weight can be calculated). If the optimization permits equation (6), then a property such as σ_0 must be specified; and R and ρ_{cm} remain to be determined (with $n_{p_{\max}}$ a by-product). In either case, the determination requires that a relation between σ_0 and ρ_{cm} be known for the crushable material, thereby effectively reducing the number of unknowns by one.

The required relation between σ_0 and ρ_{cm} can be determined experimentally for a variety of materials and stated directly as in reference 2 (p. 259). It is common, however, to introduce a parameter for which values are widely known, namely, the specific energy absorption (SEA) which is defined as

$$SEA \equiv \epsilon_m \left(\frac{\sigma_0}{\rho_{cm} g_e} \right) \quad (8)$$

and which should generally be as large as possible. The relation between σ_0 and ρ_{cm} can be expressed by giving SEA in terms of σ_0 . With $\sigma = \sigma_0$ and $\epsilon = \epsilon_m$, the product $\sigma_0 \epsilon_m$ is the area enclosed by the dashed lines in figure 1(a), which is the energy absorbed per unit volume. Dividing this product by $\rho_{cm} g_e$ gives equation (8) and shows SEA to be the energy absorbed per unit mass.

Figure 5 shows the variation of SEA with σ_0 for a balsa-like class of material and a honeycomb-like class of material (neglecting glue-joint weight and the effects of high impact velocity and low temperature). The equation for SEA in terms of σ_0 given for the balsa-like material in figure 5 is

$$\left. \begin{aligned} SEA &= 24,000 \text{ ft-lb/lb} , & 800 \text{ psi} \leq \sigma_0 \leq 1,200 \text{ psi} \\ SEA &= \frac{7.49 \times 10^6}{\sigma_0^{0.81}} \text{ ft-lb/lb} , & 1,200 \text{ psi} \leq \sigma_0 \leq 1,800 \text{ psi} \end{aligned} \right\} \quad (9)$$

The balsa-like material is balsa in the sense that the second of equations (9) is deduced from the curve fit of reference 2 (p. 259) which closely approximates the data therein for solid balsa of various densities. The material is considered to be only balsa-like, however, because the first of equations (9) and the dashed portion of the balsa-like curve in figure 5 are assumed to be valid for a hypothetical cored balsa (for which cores of material are removed in the radial direction). The assumption is that roughly one-third of the material can be removed from the lightest (lowest density) solid balsa, giving a σ_0 range from 800 to 1,200 psi, without reducing the SEA by introducing significant buckling, end effects, and/or Poisson's ratio effects; and this assumption seems reasonable. It should be noted that the only corroborative case where SEA decreases with increasing σ_0 in reference 4 is for dry balsa (0-percent moisture), atmospheric pressure, and an ambient temperature of approximately 78° F.

The curve for the honeycomb-like material is presented in figure 5 so that results can be deduced for lower SEA values and also for the relatively common case where SEA increases with increasing σ_0 . The equation given in figure 5 is

$$SEA = 478.5 \sigma_0^{0.446} \text{ ft-lb/lb} , \quad 600 \text{ psi} \leq \sigma_0 \leq 1700 \text{ psi} \quad (10)$$

The material is called honeycomb-like rather than a specified honeycomb because equation (10) is deduced from a curve fit in reference 2 (p. 259) that rather loosely fits data for several types of aluminum and fiberglass honeycomb having a variety of densities. It should be noted that reference 2 makes no mention as to whether equations (9) and (10) incorporate the dynamic effects of damping and dynamic buckling (see item 3 in "Summary of Fundamental Assumptions and Limitations").

Design Procedure for Simplified Model Without Payload Penetration

For the analytical model labeled "simplified" in the present report, it is assumed that variable mass can be neglected (setting $\rho_{ck} = 0$), that built-up material can also be neglected ($\epsilon_k = 1$), that gravity forces are insignificant ($g = 0$), and that the resistance to payload penetration is constant ($F_{po}(e) = 1$). Under the first three of these assumptions (with the last required only for penetration), equations (A55) and (A62) apply (in a simplified form with $g = 0$) and the division of the latter by the former gives (with definitions from eq. (A54))

$$\frac{v_o^2}{n_p/n_{md}} = \frac{U_o^2}{n_{pge}R_p} = \frac{y_{max}^2 \left\{ (R/R_p) - [(2/3)y_{max}] \right\}}{y[(R/R_p) - y]} \quad (11)$$

Equation (A55) is a parabola with $n_{p_{max}}$ at $y = (R/R_p)/2$. Hence, for the present restrictive case, $n_{p_{max}ge}$ is the acceleration at y_{max} as long as $y_{max} \leq (R/R_p)/2$. If $y_{max} \geq (R/R_p)/2$, $n_{p_{max}ge}$ is the acceleration at $y = (R/R_p)/2$. Thus equation (11) can be expressed in terms of $n_{p_{max}}$ as

$$\frac{U_o^2}{n_{p_{max}ge}R_p} = \frac{y_{max} [1 - (2/3)(R_p/R)y_{max}]}{1 - (R_p/R)y_{max}}, \quad y_{max} \leq \frac{1}{2} \frac{R}{R_p} \quad (12)$$

$$\frac{U_o^2}{n_{p_{max}ge}R_p} = 4 \frac{R_p}{R} y_{max}^2 \left(1 - \frac{2}{3} \frac{R_p}{R} y_{max} \right), \quad y_{max} \geq \frac{1}{2} \frac{R}{R_p} \quad (13)$$

If equations (12) and (13) are multiplied through by R_p/R and if the first of equations (A54) is used (giving $y_{max} = z_{max}(R/R_p)$) the result is

$$\frac{U_o^2}{n_{p_{max}ge}R} = \frac{z_{max} [1 - (2/3)z_{max}]}{1 - z_{max}}, \quad z_{max} \leq \frac{1}{2} \quad (14)$$

$$\frac{U_o^2}{n_{p_{\max}} g_e R} = 4 z_{\max}^2 \left(1 - \frac{2}{3} z_{\max} \right), \quad z_{\max} \geq \frac{1}{2} \quad (15)$$

Equations (14) and (15), which are applicable only in the absence of payload penetration, are plotted in figure 6 as z_{\max} versus $U_o^2/(n_{p_{\max}} g_e)R$. Figure 6 can be used to determine $z_{\max} \equiv q_{\max}/R$ on the basis of U_o , R , and $n_{p_{\max}}$; and the payload radius R_p simply has to be small enough not to interfere with q_{\max} .

An interesting feature in figure 6 is that z_{\max} is determined with no knowledge of σ_o , m_{co} , or m_{po} . Once z_{\max} is known, however, m_{co} can be found for a given m_{po} and σ_o according to

$$m_{co} = \frac{2\pi\sigma_o R^3}{U_o^2} z_{\max}^2 \left(1 - \frac{2}{3} z_{\max} \right) - m_{po} \quad (16)$$

as derived from equations (A62) and (A39) with $g = 0$. It is still not necessary to know R_p . For a minimum weight design, however, R_p must be known or determined; and equation (4) must be satisfied according to the definition in equation (5). In addition, the SEA, as defined in equation (8), may be known instead of σ_o . When equations (4), (5), and (8), with $z_{\max} \equiv q_{\max}/R = q_{p_{\max}}/R$ and $m_{co} = (4/3)\pi\rho_{cm}(R^3 - R_p^3)$, are introduced into equation (16), the result is

$$J_{m\sigma} = \frac{g_e(\text{SEA})}{U_o^2} \left(\frac{\epsilon_d}{\epsilon_m} \right) \left(\frac{m_{co}}{m_{po} + m_{co}} \right) = \frac{1 - (z_{\max}/\epsilon_d) + [(z_{\max}/\epsilon_d)^2/3]}{z_{\max} [(1/2) - (z_{\max}/3)]} \quad (17)$$

where the symbol $J_{m\sigma}$ is introduced for convenience. Equation (17) can be used to determine m_{co} for a given z_{\max} (which implies knowledge of U_o and g_e as indicated in fig. 6) if ϵ_d , ϵ_m , SEA, and m_{po} are known (with ϵ_m actually canceling the same quantity in SEA). In figure 7, equation (17) is plotted for $\epsilon_d = 0.7, 0.8$, and 0.9 . The three cross-plotted values of R_p/R serve as a reminder that figure 7 represents a design for which contact would occur between the payload and the compacted material if that material had a compacting strain of ϵ_d instead of ϵ_m (see the sketch, fig. 7).

In the absence of payload penetration, figures 6 and 7 are sufficient for the simplified model if R is given and R_p is to be determined. If R_p is given, figures 6 and 7 remain useful as a check and as a means of determining z_{\max} , but two different figures, based on R_p , are more useful for the original design. The first of these is determined by introducing equations (4) and (5) into equations (13) and (12) as a substitute for $y_{\max} \equiv q_{\max}/R_p = q_{p_{\max}}/R_p$, yielding

$$\frac{U_o^2}{n_{p_{\max}} g_e R_p} = \frac{4\epsilon_d^2 [1 - (R_p/R)]^2 \left\{ 1 - (2/3)\epsilon_d [1 - (R_p/R)] \right\}}{R_p/R}, \quad 0 < \frac{R_p}{R} \leq 1 - \frac{1}{2\epsilon_d} \quad (18)$$

$$\frac{U_o^2}{n_{p_{\max}} g_e R_p} = \frac{\epsilon_d [1 - (R_p/R)] \left\{ 1 - (2/3)\epsilon_d [1 - (R_p/R)] \right\}}{(R_p/R) \left\{ 1 - \epsilon_d [1 - (R_p/R)] \right\}}, \quad 1 - \frac{1}{2\epsilon_d} \leq \frac{R_p}{R} \leq 1 \quad (19)$$

Equations (18) and (19) are plotted for $\epsilon_d = 0.7, 0.8, \text{ and } 0.9$ in figure 8.

Figure 9 is the companion to figure 8 and is found by using equations (4) and (5) to define a replacement for $z_{\max} \equiv q_{\max}/R = q_{p_{\max}}/R$ in equation (17). The R_p/R found in figure 8 then determines $J_{m\sigma}$ in figure 9, and $J_{m\sigma}$ determines m_{co} as before. The sketches in figures 8 and 9 show the same design configuration as that in figure 7, leaving figure 6 as the only one for which contact is not required for compacted material based on ϵ_d .

Design Procedure for Simplified Model With Payload Penetration

Payload penetration was not permitted in figures 6 through 9 (because of a hypothetical perfect bond). If penetration is now permitted (because of the total absence of bonding), the first step is to determine whether it will occur. It will occur if the design without penetration gives

$$z_{\max} > z_s \quad (20)$$

where z_s is the dimensionless displacement at which the area of material being crushed becomes large enough to cause sufficient deceleration for penetration. The quantity z_s is defined by equation (A58) as modified by the change of variable, $y_s = z_s(R/R_p)$. The modified equation, plotted in figure 10, is

$$\left(\frac{R_p}{R} \right)^2 \left(1 + \frac{m_{co}}{m_{po}} \right) = 2z_s(1 - z_s) \quad (21)$$

The curve is cut off at $z_s = 0.5$, which is the maximum value at which penetration can occur for the present approximation (as seen by the maximum force in eq. (A52)). Figure 10, while not ultimately essential for design purposes, is useful as a check, and the magnitude of z_s is significant in evaluating the importance of penetration or potential penetration.

The first of the two main design figures for penetration is based partly on the first of equations (A59) and the last of equations (A39) with $g = 0$ and $n_p = n_{p_{\max}} = \text{constant}$. This yields, as expected for the present assumptions,

$$n_{p_{\max}} = \frac{\pi R_p^2 \sigma_o}{m_{po} g_e} \quad (22)$$

Equation (22) is used, together with equation (21), equation (A64) for $g = 0$, the last of equations (A39), the first and second of equations (A54), and equations (4) and (5) for $z_{p_{\max}} \equiv q_{p_{\max}}/R$, to identify the variable N_{RU} as follows:

$$N_{RU} \equiv \frac{R_p}{R} \left(1 + \frac{U_o^2}{2 \epsilon_d n_{p_{\max}} g_e R_p} \right) = 1 - \frac{z_s}{\epsilon_d} \left[\frac{1 - (4/3) z_s}{2(1 - z_s)} \right] \quad (23)$$

The purpose in isolating N_{RU} is to obtain a single unknown (R_p/R) in terms of z_s and ϵ_d , with a factor that is a function of known quantities (U_o , ϵ_d , $n_{p_{\max}}$, g_e , R_p). The next step is to isolate a variable for m_{co}/m_{po} without R_p/R . This is accomplished by dividing equation (21) by the square of equation (23). The resulting variable, called N_{mu} , is

$$N_{mu} \equiv \frac{1 + (m_{co}/m_{po})}{\left[1 + (U_o^2 / 2 \epsilon_d n_{p_{\max}} g_e R_p) \right]^2} = \frac{2 z_s (1 - z_s)}{\left(1 - (z_s / \epsilon_d) \left\{ [1 - (4/3) z_s] / 2(1 - z_s) \right\} \right)^2} \quad (24)$$

Figure 11 is a plot of N_{RU} versus N_{mu} for $\epsilon_d = 0.7, 0.8$, and 0.9 . The plot is constructed by selecting numbers for z_s between 0 and 0.5 and calculating the corresponding values of N_{RU} and N_{mu} according to equations (23) and (24). A relationship between R and m_{co} is established in figure 11 in terms of the known quantities U_o , ϵ_d , $n_{p_{\max}}$, g_e , R_p , and m_{po} (in contrast to fig. 8 without penetration, where R can be determined from known quantities and used in determining m_{co} in fig. 9). The sketch in figure 11 shows the design condition implicit in equations (4) and (5) for penetration, namely, contact between the two regions of compacted material if ϵ_m were replaced by ϵ_d .

A definition and a volume density relationship are useful at this point, namely:

$$N_{m\sigma} \equiv \frac{W_{po} (m_{co}/m_{po})}{(\rho_{cm} g_e) \pi R_p^3} \equiv \frac{W_{co}}{(\rho_{cm} g_e) \pi R_p^3} \equiv \frac{m_{co}}{\rho_{cm} \pi R_p^3} = \frac{4}{3} \left[\left(\frac{R}{R_p} \right)^3 - 1 \right] \quad (25)$$

where W_{po} and W_{co} are the original weights of the payload and crushable material, respectively. Equation (25) is plotted in figure 12; it is useful

with or without payload penetration and does not depend on any assumptions. For the case of payload penetration, however, and for the special assumptions of the simplified design, equation (22) applies and can be substituted into equation (25) with equation (8) to give

$$N_{m\sigma} = \frac{SEA}{n_{pmax} \epsilon_m R_p} \left(\frac{m_{co}}{m_{po}} \right) \quad (26)$$

With equation (26), m_{co}/m_{po} can be determined from $N_{m\sigma}$ without knowing ρ_{cm} . Thus figure 12 becomes the companion for figure 11 in an iterative design procedure for payload penetration. The procedure is simply to select an initial value for m_{co}/m_{po} , calculate N_{mu} in terms of m_{co}/m_{po} and known quantities, determine N_{RJ} from figure 11, evaluate R_p/R in terms of N_{RJ} and known quantities, determine $N_{m\sigma}$ from figure 12, calculate a second value of m_{co}/m_{po} in terms of $N_{m\sigma}$ and known quantities, and repeat the process until two values of m_{co}/m_{po} agree to the accuracy permitted by the figures.

The iterative procedure just described could have been avoided, of course, by combining equations (21) through (26) into a polynomial for z_s . This polynomial could be solved for selected parametric values of $U_o^2/2\epsilon_d n_{pmax} g_e R_p$ and $SEA/n_{pmax} \epsilon_m R_p$, together with values of ϵ_d such as those selected for the iterative charts, and R_p/R and m_{co}/m_{po} could be determined accordingly. Such a procedure was avoided, however, because of the strong likelihood that a reasonably limited group of parametric values would not have sufficiently broad applicability.

Specialization of Design Procedures for Simplified Model to Materials of Figure 5

Regardless of whether penetration is absent or present, it is apparent that all of the design figures (6 through 12) are essentially independent of the material or structure selected for energy absorption. To calculate m_{co} from figures 7, 9, and 12, however, an SEA has to be selected. With m_{co} and R determined by the figures and R_p known in advance, ρ_{cm} can be calculated (with the aid of fig. 12 if desired); and σ_o can then be found for the selected SEA according to equation (8). All this implies the assumption that a material having the calculated properties is available or that a corresponding structure can be constructed.

For the comparison purposes of this paper, however, the materials are restricted to a choice between the two classes described in figure 5. With figures 6 through 12 having been constructed independently of figure 5 (in the interest of generality), the use of figure 5 imposes a trial-and-error (or transcendental) solution for those designs in which payload penetration is absent. The trial-and-error solution is aided by incorporating equations (8) and (25) into equation (17) to yield

$$SEA = \frac{\epsilon_m J_{m\sigma}}{(g_e \epsilon_d / U_o^2) - (J_{m\sigma} W_{po} / \sigma_o N_{m\sigma} \pi R_p^3)} \quad (27)$$

On the basis of given values of ϵ_m , g_e , ϵ_d , U_0 , W_{po} , R_p , and n_{pmax} , plus values of $J_{m\sigma}$ and $N_{m\sigma}$ determined according to figures 8, 9, and 12, the quantities $\epsilon_m J_{m\sigma}$, $g_e \epsilon_d / U_0^2$, and $J_{m\sigma} W_{po} / N_{m\sigma} \pi R_p^3$ in equation (27) can be calculated in advance. Equation (27) and figure 5 then become the basis for the numerical solution.

A sample calculation for the trial-and-error solution just described is given in appendix B. It should be noted that the trail and error of appendix B would have been eliminated if the SEA had been constant - despite variations in σ_0 , as for the balsa-like curve in figure 5 when $\sigma_0 < 1,200$ psi. There is, however, another type of trial and error that occurs when a specific value of σ_0 , rather than n_{pmax} , is sought. In this case, calculations like those in appendix B (but without the σ_0 - SEA trials) must be performed for successive selections of n_{pmax} until σ_0 approaches the desired value.

If (in contrast to appendix B) payload penetration is present, the use of the specific materials in figure 5 does not impose a trial-and-error solution. The reason is that the unknown m_{co} does not appear in equation (22). In addition, the simplicity of equation (22) means that either σ_0 or n_{pmax} can be selected without requiring trial and error.

A sample calculation for the iterative penetration procedure described earlier is given in appendix C for the balsa-like material of figure 5. Only three iterations are needed in appendix C because of a fortunate initial guess of m_{co}/m_{po} . The initial guess was based for all calculations on other penetration cases or prior examples without penetration, and the worst guess required five iterations. When a penetration design is not feasible, either the σ_0 value of equation (22) will be beyond the range of figure 5, or the iterations will move off the curves of figures 11 and 12.

Computer Procedures

A set of three computer procedures has been programmed to evaluate the governing equations of the impact problem for spheres (eqs. (A32), (A37), and (A41)) in accordance with the appropriate termination conditions (eqs. (A46) and (A47)) and the appropriate design conditions (eqs. (4), (6), and (7)). These procedures are described in appendix D. They can be used to check the simplified model designs or to initiate simplified designs and other designs based on more complicated models.

Specifically, of the three computer procedures, two are designs in that they automatically iterate initial guesses to determine required crushable casing parameters. One of the two design procedures varies the overall radius R and the material maximum crushing stress σ_0 to achieve a desired acceleration, as indicated by equation (6) or equation (7), and a desired ratio of stroke to available stroke, as suggested by equation (4). This program is applicable only in the absence of payload penetration. The other design varies only R for a selected σ_0 (fixed material once SEA or a plot of

SEA versus σ_0 is selected) and achieves only the desired stroke ratio. It applies both with and without penetration.

Penetration requires only a search for R since σ_0 is essentially determined in that case regardless of R or the stroke. The reason becomes apparent when the first of equations (A41) is modified at the start of penetration ($e = de/dx = 0$) by equations (A45), (A42), and the last of equations (A39) to give the expected result

$$n_{p_{\max}} \approx -\frac{g}{g_e} + \frac{\pi R_p^2 \sigma_0}{m_{po} g_e} \quad (28)$$

where the approximate equality sign is used because $n_{p_{\max}}$ differs slightly from the value at the start of penetration for the detailed model (by at most one part in a thousand for the present examples). Equation (28) determines σ_0 for a given $n_{p_{\max}}$ regardless of R or the stroke.

The third computer procedure can also be used with or without penetration but is not programmed to iterate and produce a design. Hence it can be used only to check a given configuration.

It should be noted that all three programs permit SEA to be selected arbitrarily or calculated (after σ_0 is selected) according to equations (9) and (10) for the materials considered herein.

Design Procedure for Detailed Model With and Without Payload Penetration

The detailed model is the second of the two approximate analytical models. Where the simplified model had $\rho_{ck} = 0$, $\epsilon_k = 1$, $g = 0$, and $F_{po}(e) = 1$, the detailed model has $\rho_{ck} = \rho_{cm}$, $\epsilon_k = \epsilon_m$, $g = g_L$, and from equation (A45),

$$F_{po}(e) = 2 \int_0^1 \frac{(e s_p + 1) s_p ds_p}{\sqrt{2e s_p + e^2 + 1}}$$

The $\rho_{ck} = \rho_{cm}$ equation means that the detailed model incorporates variable mass (accumulating on the payload and/or the landing surface) according to the crushable material density, and $\epsilon_k = \epsilon_m$ implies a finite volume of compacted material instead of an infinitely thin sheet to determine the surface for stress evaluation. The equation $g = g_L$ simply incorporates a negligibly small gravity term for completeness, and the integral for $F_{po}(e)$ permits a calculated deviation from a constant resistance to penetration.

While the computer procedures described in the previous subsection constitute an alternative to figures 5 through 12 for the simplified model, they constitute the only design procedure presented herein for the detailed model. Of course, figures 5 through 12 remain useful as starting points for the computer iterations.

DESIGN RESULTS AND DISCUSSION FOR SIMPLIFIED AND DETAILED MODELS HAVING SPHERICAL GEOMETRY

Description of Design Examples and Most General Results

Thirteen examples have been calculated by the simplified and detailed analytical models described in the previous section. The impact velocity U_0 is taken to be 300 ft/sec for all examples, the material compacting strain ϵ_m to be 0.8, the design compacting strain ϵ_d to be 0.7, and the payload maximum g loading $n_{p_{max}}$ to be 2000 or less. The examples vary in the given payload weight W_{po} , the given payload radius R_p , the presence or absence of a hypothetical perfect bonding, and/or the given material. All examples are based on a choice between two classes of crushable material - the balsa-like and honeycomb-like materials defined in equations (9) and (10) and shown in figure 5. The desired value of $n_{p_{max}}$ (for which the label n_{des} is used where needed) is given for some examples and the maximum crushing stress σ_0 for others.

The results for all examples are presented in table 1 in terms of the presence or absence of penetration, the value of $n_{p_{max}}$ (if not given) or of σ_0 (if not given), the crushable material density ρ_{cmge} , the specific energy absorption SEA, the stroke-to-potential-start-of-penetration ratio $q_{p_{max}}/q_s$, the overall radius R , the crushable material weight W_{co} , the total weight $W_{co} + W_{po}$, and the dimensionless unused stroke L/R . When L/R is negative, the payload would go too far (slightly, for the present examples) and cause excessive accelerations if it were not for the stroke margin of safety given by the use (in defining L/R) of the fictitious design compacting strain ϵ_d rather than the material value ϵ_m .

The resulting quantities just listed are presented for the simplified and detailed models in table 1; the corresponding ratios of detailed to simplified results are presented when the results are numerical. It is apparent from the W_{co} ratios that the simplified model has the lower W_{co} .

An important ground rule for the ratios of table 1 is that either the σ_0 ratio or the $n_{p_{max}}$ ratio is required to be essentially unity. The choice is made, after the simplified model has been calculated, in favor of the lightest resulting detailed model. This gives the best weight ratio, that is, the ratio closest to unity.

In view of this choice, it is not surprising that the worst σ_0 or $n_{p_{max}}$ ratios (of detailed to simplified results) are farther from unity than the worst weight ratios. In fact, the worst ratio of all is 1.2917 for σ_0 in case 1 (except for L/R , where numbers approach zero, fortunately). This ratio, although not excessively different from unity, represents a large enough difference in required material (within the honeycomb-like category of case 1) that a designer would wish to know whether the simplified model is numerically more realistic than the detailed model or vice versa.

In a footnote of table 1 it is noted that the simplified results are "chart" results (derived from figs. 5 through 12) except for the L/R column and cases 7 and 12, which are automatic computer results. The two cases (both without penetration) were added after the computer design programs became available and were calculated by those programs for convenience.

The simplified results determined by the chart method have been checked by the computer checking program (as opposed to a design program). The derived computer quantities $n_{p_{max}}$ and $q_{p_{max}}/q_s$ had a maximum error of 1 percent relative to the chart method, and the derived computer quantity L/R was close to zero (ranging from -0.001781 to 0.001163 with an average of -0.000194) as compared to a zero chart value. Slightly larger differences between the chart method and the computer checking method occurred for W_{co} and $W_{co} + W_{po}$, but these differences resulted purely from errors in calculating crushable material volumes in the chart method. The chart and computer results combined to form smooth plots for the simplified model, as seen in figures 13 and 14.

All numerical results from table 1 are plotted in figures 13 and 14 except for $W_{co} + W_{po}$ (which is considered less important than W_{co}), L/R (which is often sporadically variable in sign), cases 3, 5, and the detailed model for case 2 (which will be discussed later). Note that the curves for the simplified and detailed models are roughly parallel (and only slightly curved) over their mutual abscissa range. Hence trends are the same for the two models. Even the crossover in figure 14(d) for $q_{p_{max}}/q_s$ without payload penetration is almost parallel and thus maintains the trend with only a slight comparison reversal between models.

Effect of Payload Radius (and Payload Packaging Density) for Balsa-like and Honeycomb-like Materials Without Payload Penetration

Crushable casing properties and performance are presented in figure 13 (with and without penetration) as functions of payload radius R_p (with four numbers attached for payload packaging density ρ_{pge}) for honeycomb-like material, a payload weight of 100 lb, and an $n_{p_{max}}$ value of 2000. The corresponding cases in table 1 are 1, 4, 6, and 7 without penetration and case 2 (simplified model only) with penetration.

In the absence of payload penetration, figures 13(a), 13(b), and 13(c) show that an increasing R_p (decreasing ρ_{pge}) causes W_{co} , SEA, R, σ_o , and ρ_{cmge} to increase (with $n_{p_{max}}$ held at the maximum permissible value of 2000, which minimizes W_{co} according to preliminary calculations). The potential penetration ratio $q_{p_{max}}/q_s$ exists only for the simplified model at $R_p = 0.6$ ft (among the plotted points), indicating penetration to be impossible for the other cases. Between the two models, the simplified model has the lower W_{co} (slightly), the lower SEA, the higher R, the lower σ_o , and the lower ρ_{cmge} . The lower ρ_{cmge} is the only apparent reason for the lower

W_{co} . It results from the lower σ_0 , which is made possible by the fact that the simplified model sees a higher average stress for a given σ_0 than does the detailed model.

Somewhat similar curves are shown in figure 14 for balsa-like material and a payload weight of 450 lb (the cases from table 1 being 8, 10, 12, and 13 without penetration, and 9 and 11 with penetration). It should be noted that the 450-lb payload, in contrast to the lighter payload, permits the use of the efficient balsa-like material without causing excessive decelerations in the absence of penetration. When penetration is absent, results are presented for the lowest σ_0 considered, namely, 800 psi. According to preliminary calculations, this σ_0 value gives minimum weight results for the balsa-like material (cored when σ_0 is less than 1200 psi), as opposed to $n_{p_{max}} = 2000$ for the honeycomb-like material. The stress of 800 psi determines SEA as 24,000 ft-lb/lb and ρ_{cmge} as 3.84 lb/ft³. Figures 14(a), 14(b), 14(c), and 14(d) then show that an increasing R_p (decreasing ρ_{pge}) causes W_{co} , R , and $n_{p_{max}}$ to increase but causes $q_{p_{max}}/q_s$ to decrease (decreasing the likelihood of penetration, as expected for increasing R_p). Note that the $q_{p_{max}}/q_s$ of 0.730 at $R_p = 1.6$ ft is the only case where penetration is impossible because $q_{p_{max}}/q_s$ is less than one. A comparison of the simplified and detailed models indicates that the former has the lower W_{co} , the lower R , and the higher $n_{p_{max}}$. The $q_{p_{max}}/q_s$ curves have a shallow crossover (in the absence of payload penetration), and $q_{p_{max}}/q_s$ does not exist for the detailed model at $R_p = 1.6$ ft.

This absence of $q_{p_{max}}/q_s$ for the detailed model when it exists for the simplified model has been a recurring theme without penetration, as seen in table 1, and indicates that the detailed model is the least susceptible to penetration. The reason for this is the relatively low maximum g loadings, $n_{p_{max}}$, for the detailed model in figure 14(c).

Effect of Payload Penetration

The data for payload penetration in figures 13 and 14 are limited by the fact that penetration often does not occur even when the payload is unbonded (see the $q_{p_{max}}/q_s$ column in table 1 for case 2 with the detailed model and for cases 4, 6, 7, and 13 with both models). It is seen in figure 13 for honeycomb-like material, that penetration reduces W_{co} , increases SEA and σ_0 , decreases R , increases ρ_{cmge} , and decreases $q_{p_{max}}/q_s$ for the simplified model at $R_p = 0.6$ ft. The impossibility of penetration for the plotted abscissas higher than $R_p = 0.6$ ft means that the W_{co} curve for the higher R_p values could have been combined with the penetration point at $R_p = 0.6$ ft to form a W_{co} curve for an unbonded payload, with an obviously beneficial effect.

The W_{co} benefit due to penetration at $R_p = 0.6$ ft results from the increase in SEA and σ_0 and the corresponding decrease in R . These

quantities can change because the honeycomb-like material is allowed to change within its class to maintain $n_{p_{\max}} = 2000$ for penetration (which gives the lowest W_{CO} , according to preliminary calculations, as it did without penetration).

In figures 14(a) and 14(d) for balsa-like material, it is apparent that payload penetration increases W_{CO} and decreases $q_{p_{\max}}/q_s$ for both models at $R_p = 1.0$ ft and $R_p = 1.2$ ft when SEA, σ_0 , and ρ_{cmge} are held constant at 24,000 ft-lb/lb, 1,200 psi, and 5.76 lb/ft³, respectively (where $\sigma_0 = 1,200$ psi defines the elbow of the SEA curve in fig. 5 and gives the minimum W_{CO} according to preliminary calculations). The overall radius R is shown in figure 14(b) to be increased by penetration at $R_p = 1.0$ ft and decreased at $R_p = 1.2$ ft; the apparent contradiction between the R and W_{CO} effects of penetration is resolved by recalling that the lowest W_{CO} without penetration was for a lower ρ_{cmge} , namely 3.84 lb/ft³, than for penetration. In figure 14(c) the effect of penetration on $n_{p_{\max}}$ is seen to be the same for the two models at $R_p = 1.0$ ft but different at $R_p = 1.2$ ft.

The W_{CO} effect of penetration indicates that a perfect payload bonding would be desirable for the cored balsa-like material at $R_p = 1.0$ ft and $R_p = 1.2$ ft. In the event that such a bonding is not feasible or trustworthy, however, the case of an unbonded payload must be considered. Hence undefined, wavy-line transitions between penetration and no penetration are shown in figures 14(a), 14(b), and 14(c), but not in figure 14(d) (due to lack of space). The most important of these transitions is for W_{CO} in figure 14(a). If the W_{CO} transition were specified in the area of the wavy line, it would define a curve for an unbonded payload since the wavy line skips over $R_p = 1.4$ ft, where bonding is required to prevent penetration at $\sigma_0 = 800$ psi.

Stresses between 800 and 1200 psi (the minimum weight value for penetration) will presumably be useful in the transition. Thus a variety of specified transitions will be possible. For an unbonded payload, it would be desirable to seek a minimum W_{CO} in the transition region for a single σ_0 at which penetration is ready to begin at the end of the stroke; but this is beyond the scope of the present report. The reasonable assumption, however, is that such a minimum W_{CO} exists and indicates an important design trade-off for cored balsa, a point where a further increase in payload packaging density (the abscissa of fig. 14(a)) is undesirable.

The most important effects of payload penetration discussed so far have been a decrease of W_{CO} for the honeycomb-like material and an increase of W_{CO} for the balsa-like material. Both comparisons have been based on material variations for minimum weight within the categories. If these variations are not allowed, penetration can always be expected to increase W_{CO} .

Except for the roughly 7-percent decrease in W_{CO} for the honeycomb-like material at $R_p = 0.6$ ft, there has been no advantage of penetration reported up to this point. If, however, a design is permitted to change from the honeycomb-like category to the balsa-like category, then a major

penetration advantage occurs in the present examples for the 100-lb payload. Specifically, a comparison of case 1 ($R_p = 0.6$ ft with $n_{p_{max}} = 2000$, honeycomb-like, no penetration) and case 3 ($R_p = 0.6$ ft, $\sigma_o = 1200$ psi, balsa-like, penetration) from table 1 shows a weight saving due to penetration by a factor greater than 3 in W_{co} and greater than 2 in $W_{co} + W_{po}$. In addition, a comparison of case 4 ($R_p = 0.7$ ft with $n_{p_{max}} = 2000$, honeycomb-like, no penetration) and case 5 ($R_p = 0.7$ ft, $\sigma_o = 902.4$ psi at $n_{p_{max}}$ limit of 2000, balsa-like, penetration) shows a weight saving due to penetration by a factor greater than 4 in W_{co} and almost 3 in $W_{co} + W_{po}$. Presumably, a still more impressive comparison would have occurred at $R_p = 0.8$ ft except that a penetration design could not be achieved for $n_{p_{max}} \leq 2000$.

The honeycomb-like material is used in the comparisons when penetration is absent. The reason is that the balsa-like material, having the higher SEA over the same stress range (fig. 5), is considerably lighter than the honeycomb-like material. In fact, with the force determined by the stress range, the balsa-like material provides so little mass that the g loading exceeds the limit of 2000 for the 100-lb payload; and the heavier honeycomb-like material is required in the absence of payload penetration. (Note that this is not true for the 450-lb payload.)

When penetration is permitted, however, for the balsa design by removal of the hypothetical perfect bonding between the top of the payload and the crushable material, then the only stresses acting on the payload are the crushing stresses at the bottom of the payload. This reduces the force sufficiently that the payload maximum g loading can be held to 2000 even for the balsa-like material with the 100-lb payload. The high SEA of the balsa-like material then produces the large weight saving due to penetration.

Note that this weight saving applies for the selected classes of material; it would obviously be decreased if the honeycomb-like material were replaced by an intermediate class just heavy enough to bring $n_{p_{max}}$ down to 2000 without penetration. The possible availability of such a class is indicated by the less efficient balsa reported in references 4 and 5. These balsas may be made still less efficient, in the sense of being heavier, by glue joints or by the addition of weights (a required weight being the cover for the crushable material).

Thus the large weight saving due to penetration is clearly restricted to the presently selected materials. It is obviously, however, a phenomenon worth considering. The fact that a heavy honeycomb material is still being considered in recent design studies is indicated in references 5, 8, and 9; and the g loading issue raised herein is emphasized in reference 5.

Comparison With Previous Analytical Models

The foregoing results apply to the specific analytical models considered here; and a question arises as to their validity. They can be

considered valid in one sense if they constitute a logical analytical extension of a reasonably standard body of theory having at least a limited experimental verification. The extended analytical models can then be compared with future experiments to establish experience factors as well as means of improving the models.

The logical extension of standard theory is considered first, with the limited experimental verification to follow. As pointed out in the Introduction, the present analytical models extend a significant amount of prior work (e.g., refs. 1 through 9) to include the effect of payload penetration. The summary of assumptions and limitations given under "Outline of Theory" is the same as the assumptions in references 1 through 9, where stated, except for a few variations on the assumption of equation (2).³

With the fundamental assumptions the same, it is no surprise that the basic equation of motion (with the anisotropy relation removed) is the same for the present simplified model without penetration as for comparable models (mass assumed constant, infinitely thin disk of crushed material, gravity neglected) in references 1 through 9, where stated. For the present detailed model, the most nearly comparable and completely described prior model is given in reference 2. The two models are identical except that the model of reference 2 has a uniform and isotropic crushing stress instead of the particular radial distribution of equation (2). In appendix E, it is shown that such a crushing stress converts the fundamental equation (A19) into equation (E7), which agrees exactly with the fundamental equation (1-4) in appendix A of reference 2.

The analytical extension to include payload penetration is logical for the detailed model in the sense that no fundamental assumptions are added to the list given under "Outline of Theory." For the simplified model, the assumption is added that the force resisting penetration is constant, but it has already been pointed out that this is true for the detailed model to one part in a thousand or less, for the examples considered herein.

Comparison With Previous Experiment

The applicable experimental information known to the author is limited to two configurations, one tested at an impact velocity of 374 ft/sec (ref. 10) and the other at roughly 220 ft/sec (footnote 1). The latter velocity actually represents an average of velocities ranging from 215 to 225 ft/sec for four nearly identical tests. At the higher impact velocity, only a single test is considered because the exterior cover for the model in that test was the only one (out of four) sufficiently strong and resilient to prevent model disintegration.

³These variations in anisotropy can be important for various crushable materials, as pointed out in reference 5. It may be desirable to consider the standard theory as incorporating the variations of reference 5, with the assumption of equation (2) considered as an example for evaluating the effect of penetration. If, however, it is desired to have only one anisotropy relation for a standard theory, then the assumption of equation (2) is desirable since it is simple and widely used.

The tests just described demonstrated the existence of payload penetration, depending on the efficiency of the payload bonding. They also indicated that both the detailed and simplified models provide reasonable (within 10 to 30 percent) estimates of measured impact deceleration and stroke. There are not enough data to determine which model is quantitatively better.

Alternate Models

The analytical models considered here are manifestly only two out of many possibilities. Even with attention restricted to the present computer programs, it would be possible to investigate separately the effects of the limitations calling for $\rho_{ck} = 0$ and $\epsilon_k = 1$, rather than both together (the assumptions of $g = 0$ and $F_{po}(e) = 1$ being trivial). It would also be possible to set $\rho_{ck} = 0$ in the present programs for integration of the equation of motion but not for evaluation of the acceleration. The programs could be modified to incorporate various levels of bonding (rather than just zero or perfect bonding), various levels of shear resistance, and rational methods of incorporating the weight and strength of the glue joints and exterior cover. (Note that any SEA changes due to glue joints or freezing of the crushable material could be incorporated by changing fig. 5 and the corresponding equations defining the material.)

Two alternate models have been briefly investigated; a full investigation would require changes in the machine programs or the design charts. In one, called the "hemisphere" model, the payload and the entire upper hemisphere are able to penetrate as a unit, regardless of bonding, because of low resistance to cross-grain crushing in the equatorial plane. In the other, called the "shear-plug" model, the payload and the cylinder (with rounded ends) directly above it are able to penetrate as a unit, again regardless of bonding, because of low shear resistance over the cylinder walls.

The investigation of the hemisphere model indicates that the payload and upper hemisphere would have started to penetrate below the maximum g loadings for almost all cases in table 1, and would have done so more readily than the isolated payload for the detailed and simplified models, provided that the cross-grain crushing strength is 8 percent of the end grain value. Hemisphere penetration is calculated even at 18 percent (ref. 3 for balsa) for several cases. At 8 and 14 percent, however, it is also calculated for the high-speed (374 ft/sec) experimental configuration at a g loading of 3000 to 4000 (ref. 10); yet there was no evidence of hemisphere penetration (i.e., of exterior cover wrinkling at the equator). Thus, 18 percent may be the most nearly correct figure, particularly when the glue joints are considered. In any event, the hemisphere model is of interest.

For the shear-plug model, on the other hand, there is no possibility of shear-plug penetration at the g loadings under consideration according to calculations based on a measured shear strength. This model would be of interest only for much higher g loadings (say, greater than 3000) and/or much lower shear strengths (less than 145 psi).

Finally, a question remains as to the effect of payload radius R_p when densities (including payload packaging density) and stresses remain the same, that is, a question as to the effect of scaling. Except for the trivial gravity force, the equations of motion indicate (for a nondimensionalization different from that of appendix A) that geometric scaling should apply, with U_0 and SEA unaffected, with $n_{p_{max}} \sim 1/R_p$, $R \sim R_p$, and $W_{co} \sim R_p^3$. These scaling conditions, then, can be used to extend the present results. They can also be used to check numerical results whenever two cases scale each other. In the present examples, only cases 3 and 9 should roughly scale each other, as indeed they do.

CONCLUDING REMARKS

The governing equations for the landing impact of a rigid payload protected by a crushable casing, including the possibility of penetration by the payload into the casing, have been developed for a general vertically symmetrical landing. The general equations have been specialized for zero shear resistance, a constant compacting strain, and uniform density of the crushable casing. They have also been specialized for a spherical payload and casing, with the latter having its highest crushing stress in the radial direction. For the spherical configuration, two approximate analytical models have been defined: (1) a detailed model with no additional assumptions but requiring an automatic computer program; and (2) a simplified model utilizing either the computer program or design charts but requiring the assumptions of infinitely thin sheets of crushed material, constant mass in the equations of motion, zero acceleration due to gravity, and a constant resistance to payload penetration. When specialized to prevent penetration, the simplified model (or slight variations thereof) has been widely employed in previous work; and the specialization of the detailed model for a uniform and isotropic crushing stress without penetration has been shown to have the same basic equation as an earlier model. Results for the two models are in reasonable agreement with two previous measurements, having impact velocities of 220 and 374 ft/sec.

Thirteen examples have been presented for each of the two analytical models. The examples are for an impact velocity of 300 ft/sec, a maximum permissible g loading of 2000, payload weights of 100 and 450 lb, payload radii ranging from 0.6 to 1.6 ft, payload packaging densities ranging from 26.23 to 110.5 lb/ft³, a choice of zero or "perfect" bonding between the payload and the crushable material, and a choice of a selected balsa-like or honeycomb-like class of crushable material. Overall radii resulting from the designs range from 1.81 ft to about 3.45 ft, and the resulting crushable material weights vary from a little over 124 lb to almost 763 lb. The following conclusions are drawn from the examples:

1. The simplified model has the lower crushable material weight of the two models, the greatest difference being approximately 15 percent for an example without payload penetration.

2. The greatest difference between the two models is a 29 percent discrepancy in the maximum crushing stress determined by a design example without penetration for the honeycomb-like class of material.
3. In the absence of payload penetration, the crushable material weight and the overall radius increase with increasing payload radius, that is, with decreasing payload packaging density.
4. For the honeycomb-like class of material and the 100-lb payload (with the maximum g loading held at 2000 to minimize weight) payload penetration does not exist for the detailed model. For the simplified model, however, penetration slightly reduces both the crushable material weight and the overall radius at the lowest payload radius, 0.6 ft, the only radius among those tried for which penetration exists with honeycomb. This advantage of penetration means that bonding should be avoided with the present honeycomb-like material, for which the specific energy absorption increases with crushing stress (a variation more common even for balsa than that for the present balsa-like class).
5. For the balsa-like class of material (with a payload weight of 450 lb), penetration drastically increases the crushable material weight at the lowest payload radius (1.0 ft) and slightly increases it at the next lowest radius (1.2 ft). This combines with nonpenetration results to give a minimum-weight radius for an unbonded payload between 1.2 and 1.6 ft and a corresponding minimum-weight payload packaging density between 26.33 and 62.15 lb/ft³.
6. An impressive benefit of payload penetration is a decrease in crushable material weight by a factor greater than 4, which occurs for the 100-lb payload with a radius of 0.7 ft when the (selected) honeycomb-like class of material is required without penetration (by the g loading ceiling of 2000), but when the more efficient balsa-like class is feasible with penetration.

Ames Research Center
National Aeronautics and Space Administration
Moffett Field, Calif., 94035, Jan. 12, 1970

APPENDIX A

DEVELOPMENT OF BASIC EQUATIONS

GENERAL GOVERNING EQUATIONS

Figure 2 shows a fairly general landing geometry at the start of impact and at two later instants of time during impact. The only shape requirement is symmetry about two mutually perpendicular vertical planes, and this requirement is made for compatibility with the assumption of pure vertical translation. The crushing strength and density of the crushable material are also required to be symmetrical but otherwise generally variable. The landing surface is assumed to be perfectly flat and rigid. The payload is assumed to be perfectly rigid and is considered unbonded to the crushable material in determining the start of relative motion (if any), herein referred to as "payload penetration."

The analysis begins with the phase of impact shown in figure 2(b). In this phase, the crushable material has begun to crush against the landing surface, but payload penetration has not begun. Hence,

$$q_p = q \quad (A1)$$

where q_p and q are the absolute displacements of the payload and the uncrushed crushable material, respectively, as shown in figure 2(b). The equation of motion for the constant payload mass m_{po} is written as:

$$m_{po} \ddot{q} = m_{po} g - \int_{A_{po}} \int \sigma_{vpo} dA \quad (A2)$$

where \ddot{q} is the second time derivative of q , g the local acceleration due to gravity, σ_{vpo} the vertical component of normal stress on m_{po} , and A_{po} the area over which the stress acts.¹

The equation of motion is now written for the variable mass $m_{co} - m_{c1}$ of uncrushed crushable material in figure 2(b) under the assumption that each particle in $m_{co} - m_{c1}$ is moving at the same vertical velocity \dot{q} at a given instant. The equation is

¹Note that the vertical component of shear stress on the payload could have been added to σ_{vpo} in equation (A2) and in the later equations containing σ_{vpo} . There are, however, no σ_{vpo} terms in the major governing equations except for the equation that determines the existence of payload penetration. When penetration is about to start, the most important stresses are σ_{vpo} values that are almost large enough to crush the material (in its strongest direction if it has one and has been deployed to utilize the fact). Shear stresses are negligible by comparison and are often incorporated in the tests to determine the crushing strength.

$$(m_{co} - m_{c1})\ddot{q} = (m_{co} - m_{c1})g + \int_{A_{po}} \int \sigma_{vpo} dA - \int_{A_{c1}} \int \sigma_v dA \quad (A3)$$

where σ_v is the vertical component of the "mostly static" and "mostly normal" stress capable of deforming the crushable material plastically over the area A_{c1} . The term "mostly static" implies the assumptions that the damping force is incorporated and that the coupling between vertical and horizontal velocity, or dynamic buckling effect, is also incorporated. The term "mostly normal" implies the incorporation of a small shear stress. (See the discussion of figs. 1(b) and 1(c) under "Properties of Typical Crushable Material.") The area A_{c1} is the intersection between $m_{co} - m_{c1}$ and the mass of crushed material m_{c1} in figure 2(b). The crushed material is assumed to have been compacted sufficiently to deliver the required crushing stress σ_v ; and successive layers of material are transferred from $m_{co} - m_{c1}$ to m_{c1} at the boundary A_{c1} as they undergo plastic deformation. (Such a process is observed experimentally in the crushing of plastic foam, balsa parallel to its grain, and honeycomb parallel to its axis.)

The assumption of a uniform (though time variable) vertical velocity \dot{q} throughout $m_{co} - m_{c1}$ has two implications besides the crushing by layers just described. First, the elastic stress waves that establish a uniform \dot{q} must obviously travel at speeds far greater than \dot{q} (i.e., \dot{q} must be a low subsonic value). Second, the deformation waves associated with the elastic stress waves must be small enough not to affect the magnitude of \dot{q} .

Equations of motion could also be written for m_{c1} in figure 2 and for the elemental layer of mass being transferred to m_{c1} . These equations would determine dynamic stresses in the sense of variable mass, however, and are not needed since σ_v is assumed to be a measured quantity.

Equations (A2) and (A3) can be used to determine whether payload penetration occurs and, if so, at what displacement. If both equations are solved for $\ddot{q} - g$ and the results equated and rearranged, the result is:

$$\int_{A_{po}} \int \sigma_{vpo} dA = \frac{m_{po}}{m_{po} + m_{co} - m_{c1}} \int_{A_{c1}} \int \sigma_v dA \quad (A4)$$

where $m_{po} + m_{co} - m_{c1}$ is the total time-dependent mass at velocity \dot{q} in the absence of payload penetration. Equation (A4) is the only major governing equation containing σ_{vpo} ; the neglect or incorporation of shear stresses is justified in footnote 1 of this appendix.

If equation (A4) is considered formally solved for σ_{vpo} , payload penetration cannot begin until those stresses become large enough to cause plastic failure, that is, become a σ_v distribution. This will occur only if the geometry, masses, and impact conditions are such that the displacement q becomes large enough to bring A_{c1} up to the necessary size. It can be

seen in equation (A4) that the following quantities tend to prevent or postpone payload penetration: a large payload bearing area A_{po} , a small payload mass m_{po} , a large total mass $m_{po} + m_{co} - m_{cl}$, and a small bearing area of compacted material A_{cl} .

Equations (A2) and (A3) can be added to give the major governing equation:

$$(m_{po} + m_{co} - m_{cl})\ddot{q} = (m_{po} + m_{co} - m_{cl})g - \int_{A_{cl}} \int \sigma_v dA \quad (A5)$$

This is the simplest equation of motion to apply during the impact period prior to payload penetration. It does not contain σ_{vpo} (see footnote 1 of this appendix).

If equation (A4) shows that payload penetration has begun, the geometry of figure 2(c) applies. The constant payload mass m_{po} is then positioned by the coordinate q_p so that equation (A2) becomes:

$$m_{po}\ddot{q}_p = m_{po}g - \int_{A_{po}} \int \sigma_{vpo} dA \quad (A6)$$

The mass m_{p1} in figure 2(c) consists of compacted crushable material. The velocity \dot{q}_p of m_{po} is assumed to apply uniformly throughout m_{p1} . Hence, the equation of motion for m_{p1} can be written:

$$m_{p1}\ddot{q}_p = m_{p1}g + \int_{A_{po}} \int \sigma_{vpo} dA - \int_{A_{p1}} \int \sigma_v^1 dA \quad (A7)$$

where A_{p1} is the intersection between m_{p1} and the variable mass $m_{co} - m_{cl} - m_{p1}$ of uncrushed crushable material, and σ_v^1 differs from the "mostly static" crushing vertical component σ_v acting over A_{p1} only because the elemental layer of mass dm_{p1} is transferred to m_{p1} .

The equation of motion for dm_{p1} becomes, with the definitions just given:

$$dm_{p1} \left(\frac{\dot{q}_p - \dot{q}}{dt} \right) = \int_{A_{p1}} \int \sigma_v^1 dA - \int_{A_{p1}} \int \sigma_v dA$$

or

$$(\dot{q}_p - \dot{q})\dot{m}_{p1} = \int_{A_{p1}} \int \sigma_v^1 dA - \int_{A_{p1}} \int \sigma_v dA \quad (A8)$$

where $\dot{m}_{p1} \equiv dm_{p1}/dt$, where the higher-order quantity gdm_{p1} has been neglected, and where \dot{q}_p and \dot{q} represent the final and initial velocities of dm_{p1} .

Equations (A6), (A7), and (A8) can be added to give

$$(m_{po} + m_{p1})\ddot{q}_p + (\dot{q}_p - \dot{q})\dot{m}_{p1} = (m_{po} + m_{p1})g - \int_{A_{p1}} \int \sigma_v dA \quad (A9)$$

A second major equation of motion defines the forces on the variable mass $m_{co} - m_{c1} - m_{p1}$ of uncrushed crushable material in figure 2(c). Under the assumption that each particle in $m_{co} - m_{c1} - m_{p1}$ is moving at the same vertical velocity \dot{q} , this equation is

$$(m_{co} - m_{c1} - m_{p1})\ddot{q} = (m_{co} - m_{c1} - m_{p1})g + \int_{A_{p1}} \int \sigma_v dA - \int_{A_{c1}} \int \sigma_v dA \quad (A10)$$

where A_{p1} is defined as in equations (A7) and (A8) and A_{c1} is defined analogously to that in equation (A3).

Equations (A9) and (A10) define the motion during payload penetration since all quantities can be defined in terms of q and q_p and their derivatives. The two major governing equations are coupled in the most general case by the $\dot{q}_p - \dot{q}$ term, the dependence of \dot{m}_{p1} on $\dot{q}_p - \dot{q}$, and the dependence of m_{p1} and of σ_v over A_{p1} on $q_p - q$. Equations (A9) and (A10) do not contain σ_{vp0} .

GOVERNING EQUATIONS FOR ZERO SHEAR DEFORMATION, UNIFORM COMPACTING STRAIN, AND UNIFORM MATERIAL DENSITY

Although figure 2 does not show any shear deformation, the equations derived so far would apply even if such deformation were present. The specification of σ_v , however, requires knowledge of the location of the surfaces A_{c1} and A_{p1} , and shear deformation is ruled out at this point to retain the simple surfaces implied by figure 2. Then A_{c1} and A_{p1} are determined by the height variables h_{c1} and h_{p1} , where h_{c1} is the local height of m_{c1} in figures 2(b) and 2(c) and where h_{p1} is the local height of m_{p1} in figure 2(c). If shear deformation had been considered, there would be a trailing of material to make m_{p1} wider than m_{po} and a possible lifting off the ground of the edges of m_{c1} .

The actual lengths of h_{p1} and h_{c1} are evaluated in terms of a readily measurable variable ϵ . This variable is defined as the compressive compacting strain of the crushable material ("compacting strain" is the strain at which the crushing stress rises abruptly from a relatively constant value for a test specimen of uniform cross section). The effect of the direction of maximum strength is ignored under the assumption that the material will compress to the same compacted strain along any axis.

The use of ϵ is made feasible by the assumption that the energy absorbing process consists of the vertical crushing of separate vertical rods of material. Then h_c in figures 2(b) and 2(c) is the total shortening deformation of a rod having an initial length of $h_c + h_{c1}$, and $q_p - q$ is the corresponding deformation of a rod having an initial length of $q_p - q + h_{p1}$, where h_{p1} is the local height of m_{p1} in figure 2(c). Since the variable $\epsilon d\ell$ is (by the definition of strain) the total shortening deformation of each successive rod element $d\ell$ to be crushed, it is seen that

$$\left. \begin{aligned} q_p - q &= \int_0^{q_p - q + h_{p1}} \epsilon d\ell \\ h_c &= \int_0^{h_c + h_{c1}} \epsilon d\ell \end{aligned} \right\} \quad (A11)$$

Under the assumption of uniform compacting strain ($\epsilon = \epsilon_k = \text{constant}$), the equations just derived can easily be solved for h_{p1} and h_{c1}

$$\left. \begin{aligned} h_{p1} &= \frac{1 - \epsilon_k}{\epsilon_k} (q_p - q) \\ h_{c1} &= \frac{1 - \epsilon_k}{\epsilon_k} h_c \end{aligned} \right\} \quad (A12)$$

The effects of equations (A12) for the constant ϵ_k can be seen in figure 3, which is otherwise identical to figure 2. In figures 3(b) and 3(c), the mass m_{c1} has become a foreshortened image of the volume V_c , which would lie beneath the landing surface if there had been no crushing; and the height h_{p1} of the mass m_{p1} has become constant in figure 3(c).

The next limitation to be imposed in the analysis is that of uniform density of the crushable material prior to crushing. Then m_{p1} and m_{c1} in equations (A4), (A5), (A9), and (A10) become:

$$\left. \begin{aligned} m_{p1} &= \rho_{ck}(V_{p1} + V_p) \\ m_{c1} &= \rho_{ck}(V_{c1} + V_c) \end{aligned} \right\}$$

where V_{p1} is the volume of m_{p1} , V_p the volume swept out by m_{p0} during payload penetration, and V_{c1} the volume of m_{c1} . When V_{p1} is related to V_p and V_{c1} to V_c according to equations (A12), the masses m_{p1} and m_{c1} become

$$\left. \begin{aligned} m_{p1} &= \rho_{ck} \left(V_p \frac{1 - \epsilon_k}{\epsilon_k} + V_p \right) = \frac{\rho_{ck} V_p}{\epsilon_k} \\ m_{c1} &= \rho_{ck} \left(V_c \frac{1 - \epsilon_k}{\epsilon_k} + V_c \right) = \frac{\rho_{ck} V_c}{\epsilon_k} \end{aligned} \right\} \quad (A13)$$

The relations between the volumes V_p and V_c and the displacements q and q_p can be determined by the following volume formulas:

$$\left. \begin{aligned} V_p &= A_{poh}(q_p - q) \\ V_c &= \int_0^q A_{sh} dh_c \end{aligned} \right\} \quad (A14)$$

where A_{poh} is the horizontal planar projection of A_{p0} and A_{p1} , and A_{sh} is a horizontal cross section in V_c .

Another useful set of relations involves the stresses. The stress integrals in the major governing equations (A4), (A5), (A9), and (A10) can be written

$$\left. \begin{aligned} \int_{A_{p0}} \int \sigma_{vpo} dA &= \int_{A_{poh}} \int \sigma_{po} dA \\ \int_{A_{c1}} \int \sigma_v dA &= \int_{A_{c1h}} \int \sigma dA \\ \int_{A_{p1}} \int \sigma_v dA &= \int_{A_{poh}} \int \sigma dA \end{aligned} \right\} \quad (A15)$$

where σ_{po} is the normal stress on the payload prior to penetration, σ is the normal crushing stress on any surface, and A_{clh} is the horizontal planar projection of A_{cl} . For integration of the right-hand sides of equations (A15), the normal stresses must be evaluated at the intersections between the curved surfaces (A_{po} , A_{cl} , A_{pl}) and vertical lines through the centroids of the elements dA in the horizontal planar surfaces (A_{poh} , A_{clh} , A_{poh}).

A final useful relation is the following change of variable:

$$U \equiv \dot{q} \equiv \frac{dq}{dt} \quad (A16)$$

With equation (A16)

$$\ddot{q} \equiv \frac{d\dot{q}}{dt} \equiv \frac{dU}{dt} = U \frac{dU}{dq} = \frac{1}{2} \frac{d(U^2)}{dq} \quad (A17)$$

Equations (A13) for uniform density and uniform compacting strain, together with the volume equations (A14) and the stress equations (A15), are now introduced into the basic governing equations. In addition, one of the governing equations is reduced to first order by equation (A17). Thus equation (A4), which determines the start of payload penetration (if any), becomes:

$$\int_{A_{poh}} \int \sigma_{po} dA = \frac{m_{po} \int_{A_{clh}} \int \sigma dA}{m_{po} + m_{co} - (\rho_{ck}/\epsilon_k) \int_0^q A_{sh} dh_c} \quad (A18)$$

Equation (A5), which defines the impact prior to penetration, becomes:

$$\frac{1}{2} \frac{d(U^2)}{dq} = g - \frac{\int_{A_{clh}} \int \sigma dA}{m_{po} + m_{co} - (\rho_{ck}/\epsilon_k) \int_0^q A_{sh} dh_c} \quad (A19)$$

Finally, equations (A9) and (A10) for payload penetration become:

$$\left. \begin{aligned}
 \ddot{q}_p &= g - \frac{(\rho_{ck} A_{poh} / \epsilon_k) (\dot{q}_p - \dot{q})^2 + \int_{A_{poh}} \int \sigma \, dA}{m_{po} + (\rho_{ck} A_{poh} / \epsilon_k) (q_p - q)} \\
 \ddot{q} &= g - \frac{\int_{A_{clh}} \int \sigma \, dA - \int_{A_{poh}} \int \sigma \, dA}{m_{co} - (\rho_{ck} / \epsilon_k) \int_0^q A_{sh} \, dh_c - (\rho_{ck} A_{poh} / \epsilon_k) (q_p - q)}
 \end{aligned} \right\} \quad (A20)$$

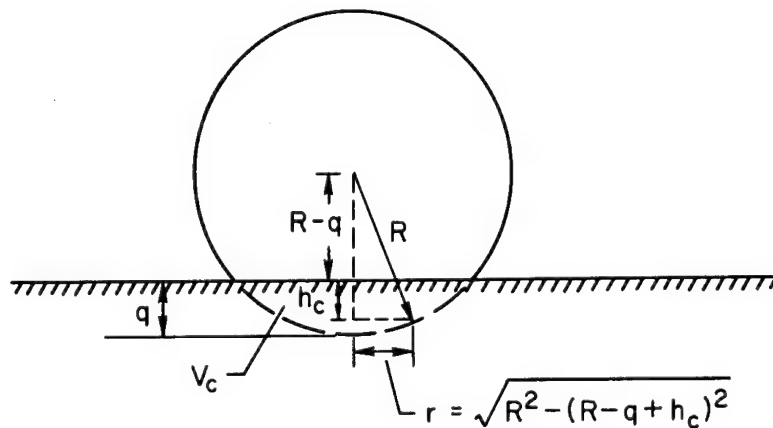
Equations (A18) through (A20) define the problem for the landing geometry of figure 3, providing the stress and volume integrals can be evaluated.

EVALUATION OF VOLUME AND STRESS INTEGRALS FOR SPHERICAL GEOMETRY

The evaluation of the volume and stress integrals is facilitated by restriction of the landing configuration to a simple shape. The sphere is particularly useful for landing packages and crushable coverings that must absorb energy from impacts in any direction. Hence, the geometry is now specialized to concentric spheres.

The spherical landing package is shown in figure 4(a) at the start of impact, in figure 4(b) during impact but prior to payload penetration, and in figure 4(c) after penetration. All angles and radial lengths are shown in a plane of maximum value.

The volume integral in equations (A18) through (A20) can be evaluated immediately on the basis of sketch (a), which is a simplification of figure



Sketch (a)

4(a) or 4(b). Thus

$$V_c \equiv \int_0^q A_{sh} dh_c = \int_0^q \pi r^2 dh_c = \pi \int_0^q [R^2 - (R - q + h_c)^2] dh_c$$

or

$$V_c \equiv \int_0^q A_{sh} dh_c = \frac{\pi}{3} q^2 (3R - q) \quad (A21)$$

It is also noted, for certain volume terms and integration areas in equations (A18) and (A20), that

$$A_{poh} = \pi R_p^2 \quad (A22)$$

as can be seen from figure 4 and the definition of A_{poh} .

One of the stress integrals can be evaluated immediately under the temporary assumption that $\sigma_{po} = \sigma_{pok} = \text{constant}$. Then, with equation (A22),

$$\int_{A_{poh}} \sigma_{po} dA = \sigma_{pok} A_{poh} = \pi R_p^2 \sigma_{pok} \quad (A23)$$

The assumption that $\sigma_{po} = \sigma_{pok}$ may be valid only when σ_{pok} approaches the normal crushing stress σ , that is, when payload penetration is approached. Fortunately, this is the only region of interest for equations (A18) and (A23).

Prior to evaluation of the stress integrals for σ , another limitation is applied to the analysis, namely,

$$\sigma = \sigma_0 \cos \alpha ; \quad \alpha < 90^\circ \quad (A24)$$

where α is the angle between the local normal to the stressed area and a radial line from the center of the spherical system (as if undeformed) through the point of stress application. (The rationale for this limitation is given immediately prior to eq. (2).)

The next step is to determine α for m_{c1} in figure 4(b) (with applicability after payload penetration as well). Any point on the surface of revolution shown by the dotted portion of the circle is defined, with the aid of sketch (a), by

$$r^2 + (R - q + h_c)^2 = R^2$$

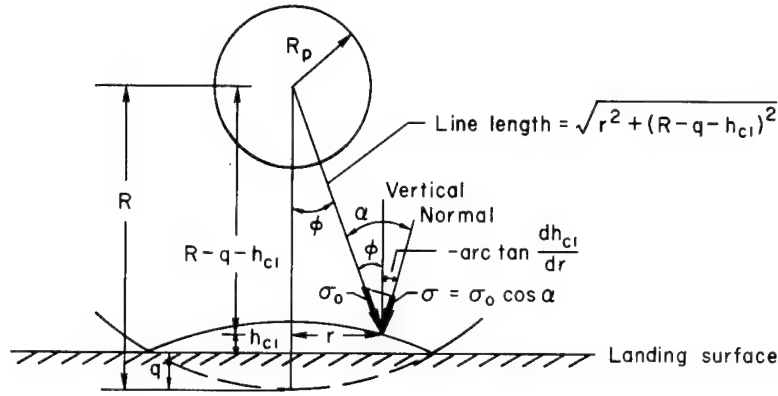
From the second of equations (A12)

(A25)

 m_{Cl} is

$$\frac{dh_{c1}}{dr} = - \frac{(1 - \epsilon_k)r}{\epsilon_k \left\{ R - q + \left[(\epsilon_k / (1 - \epsilon_k)) h_{c1} \right] \right\}} = - \frac{(1 - \epsilon_k)r}{\epsilon_k \sqrt{R^2 - r^2}}$$

Thus, with ϕ shown in figure 4(b) and from the greater detail in sketch (b),



Sketch (b)

$$\alpha = \phi - \arctan \frac{dh_{c1}}{dr} = \phi + \arctan \frac{(1 - \epsilon_k)r}{\epsilon_k \sqrt{R^2 - r^2}} \quad (A26)$$

With equation (A26) introduced into equation (A24), the normal stress on the surface A_{c1} (at height h_{c1} in fig. 4(b)) becomes:

$$\sigma = \sigma_0 \cos \left[\phi + \arctan \frac{(1 - \epsilon_k)r}{\epsilon_k \sqrt{R^2 - r^2}} \right]$$

Thus ,

$$\frac{\sigma}{\sigma_0} = \cos \phi \cos \arctan \frac{(1 - \epsilon_k)r}{\epsilon_k \sqrt{R^2 - r^2}} - \sin \phi \sin \arctan \frac{(1 - \epsilon_k)r}{\epsilon_k \sqrt{R^2 - r^2}}$$

but, in figure 4(b) and sketch (b),

$$\begin{aligned}\cos \phi &= \frac{R - q - h_{c1}}{\sqrt{r^2 + (R - q - h_{c1})^2}} \\ \sin \phi &= \frac{r}{\sqrt{r^2 + (R - q - h_{c1})^2}}\end{aligned}$$

and h_{c1} can be determined from equation (A25). Then, after some manipulation, together with

$$\int_{A_{c1h}} \int \sigma \, dA = \int_0^{\sqrt{R^2 - (R-q)^2}} \sigma 2\pi r \, dr$$

we obtain

$$\int_{A_{c1h}} \int \sigma \, dA = \sigma_0 \int_0^{\sqrt{R^2 - (R-q)^2}} \frac{2\pi[(R-q)\sqrt{R^2 - r^2} - (1 - \epsilon_k)R^2]r \, dr}{\left([(1 - \epsilon_k)^2 r^2 + \epsilon_k^2 (R^2 - r^2)] \left\{ r^2 + (1/\epsilon_k^2) [R - q - (1 - \epsilon_k)\sqrt{R^2 - r^2}]^2 \right\} \right)^{1/2}}$$

With the substitution $b \equiv \sqrt{R^2 - r^2}$, this becomes

$$\int_{A_{c1h}} \int \sigma \, dA = 2\pi\sigma_0 \int_{R-q}^R \frac{[(R-q)b - (1 - \epsilon_k)R^2]b \, db}{\left([\epsilon_k^2 - (1 - \epsilon_k)^2]b^2 + (1 - \epsilon_k)^2 R^2 \right) \left\{ R^2 - b^2 + (1/\epsilon_k^2) [R - q - (1 - \epsilon_k)b]^2 \right\}^{1/2}} \quad (A27)$$

and equation (A27) is the stress integral for the upper surface A_{c1} of m_{c1} in figure 4(b) or 4(c). The integral contains no singularities and hence can readily be evaluated numerically.

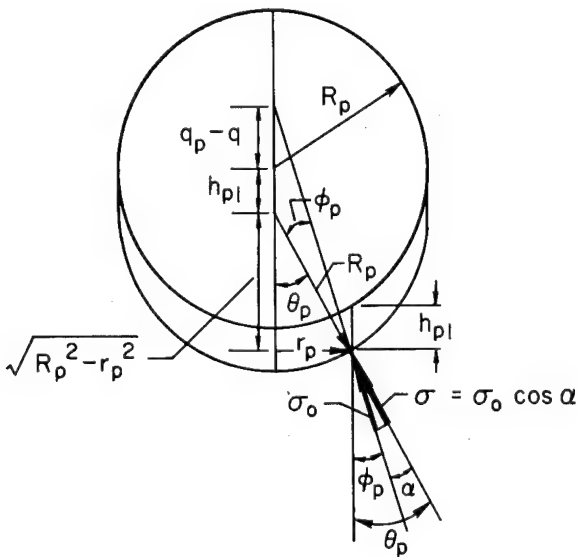
The angle α is now determined for m_{p1} in figure 4(c). Thus, with sketch (c) for detail,

$$\alpha = \theta_p - \phi_p$$

or

$$\alpha = \arcsin \frac{r_p}{R_p}$$

$$= \arctan \frac{r_p}{\sqrt{R_p^2 - r_p^2} + (q_p - q) + h_{p1}}$$



Sketch (c)

or, with the first of equations (A12),

$$\alpha = \arcsin \frac{r_p}{R_p} - \arctan \frac{r_p}{(1/\epsilon_k)(q_p - q) + \sqrt{R_p^2 - r_p^2}} \quad (A28)$$

When equation (A28) is introduced into equation (A24), the normal crushing stress σ is determined. When σ is put into $\int_{A_{poh}} \sigma dA$ with $\int_{A_{poh}} \sigma dA = \int_0^{R_p} \sigma 2\pi r_p dr_p$, the result is

$$\int_{A_{poh}} \sigma dA = \sigma_o \int_0^{R_p} \frac{2\pi [(q_p - q)/\epsilon_k] \sqrt{R_p^2 - r_p^2} + R_p^2}{R_p \sqrt{2[(q_p - q)/\epsilon_k] \sqrt{R_p^2 - r_p^2} + [(q_p - q)/\epsilon_k]^2 + R_p^2}} r_p dr_p$$

With the substitution $b_p = \sqrt{R_p^2 - r_p^2}$, this becomes

$$\int_{A_{poh}} \sigma dA = \frac{2\pi\sigma_o}{R_p} \int_0^{R_p} \frac{\{[(q_p - q)/\epsilon_k]b_p + R_p^2\}b_p db_p}{\sqrt{2[(q_p - q)/\epsilon_k]b_p + [(q_p - q)/\epsilon_k]^2 + R_p^2}} \quad (A29)$$

Equation (A29) is the stress integral for the lower surface A_{p1} of m_{p1} in figure 4(c). It can be integrated directly to give

$$\begin{aligned} \int_{A_{poh}} \sigma dA = & \frac{2\pi\sigma_o}{15R_p \left(\frac{q_p - q}{\epsilon_k}\right)^2} \left\{ \left[-2\left(\frac{q_p - q}{\epsilon_k}\right)^4 + \left(\frac{q_p - q}{\epsilon_k}\right)^2 R_p^2 + 3R_p^4 \right] \sqrt{R_p^2 + \left(\frac{q_p - q}{\epsilon_k}\right)^2} \right. \\ & \left. + \left[2\left(\frac{q_p - q}{\epsilon_k}\right)^4 - 2\left(\frac{q_p - q}{\epsilon_k}\right)^3 R_p + 2\left(\frac{q_p - q}{\epsilon_k}\right)^2 R_p^2 + 3\left(\frac{q_p - q}{\epsilon_k}\right) R_p^3 - 3R_p^4 \right] \left(R_p + \frac{q_p - q}{\epsilon_k} \right) \right\} \end{aligned} \quad (A30)$$

Since equation (A30) is indeterminate at $[(q_p - q)/\epsilon] = 0$, that is, at the start of payload penetration, the best way to evaluate $\int_{A_{poh}} \sigma dA$ is to integrate equation (A29) numerically. At $[(q_p - q)/\epsilon] = 0$, equation (A29) becomes

$$\left(\int_{A_{poh}} \int \sigma \, dA \right)_{[(q_p - q)/\epsilon] = 0} = \pi R_p^2 \sigma_o \quad (A31)$$

Comparison of equation (A31) with equations (A23) and (A24) serves as a partial check on the development of equations (A29) through (A31) since $\alpha = 0^\circ$ (or $\sigma = \sigma_o$) on the payload at the start of penetration.

Dimensionless Governing Equations for Spherical Geometry, With Termination Conditions

Governing equations that have been derived in this appendix are now made dimensionless in a form convenient for numerical solution of the impact problem with spherical geometry. Prior to payload penetration, equation (A19) applies and becomes, with equations (A21) and (A27),

$$-\frac{n_p}{n_{md}} = \frac{1}{2} \frac{d(w^2)}{dz} = \frac{g}{n_{md}g_e} - K_R \frac{F_{c1}(z)}{m(z)} \quad (A32)$$

where g_e is the acceleration due to gravity on earth, $n_p g_e$ and $n_{md} g_e$ are the actual and maximum design payload decelerations, respectively, and

$$\left. \begin{aligned} n_p g_e &= -\frac{1}{2} \frac{d}{dq} U^2 \\ w &\equiv \frac{U}{\sqrt{n_{md} g_e R}} \\ z &\equiv \frac{q}{R} \\ K_R &\equiv \frac{\pi R^2 \sigma_o}{m_{po} n_{md} g_e} \end{aligned} \right\} \quad (A33)$$

The dimensionless total mass $m(z)$ in figure 4(b) is defined by

$$m(z) \equiv \frac{m_{po} + m_{co} - m_{c1}}{m_{po}} = 1 + \frac{m_{co}}{m_{po}} - \frac{1}{4\epsilon_k} \left(\frac{\rho_{ck}}{\rho_{pR}} \right) z^2 (3 - z) \quad (A34)$$

with

$$\rho_{pR} \equiv \frac{m_{po}}{(4/3)\pi R^3} \quad (A35)$$

where $F_{c1}(z)$ is the dimensionless crushing force on $m(z)$ defined by

$$F_{c1}(z) \equiv \frac{1}{\pi R^2 \sigma_0} \int_{A_{c1h}} \int \sigma \, dA =$$

$$2 \int_{1-z}^1 \frac{[(1-z)s - 1 + \epsilon_k]s \, ds}{\left(\left\{ [\epsilon_k^2 - (1 - \epsilon_k)^2]s^2 + (1 - \epsilon_k)^2 \right\} \left\{ 1 - s^2 + (1/\epsilon_k^2)[1 - z - (1 - \epsilon_k)s]^2 \right\} \right)^{1/2}} \quad (A36)$$

with $s \equiv b/R$. Under the initial condition $w(z=0) = w_0$, equation (A32) integrates immediately to

$$w^2 = w_0^2 + 2 \int_0^z \frac{1}{2} \frac{d(w^2)}{dj} \, dj$$

$$= w_0^2 + 2 \int_0^z \left[\frac{g}{n_{md} g_e} - K_R \frac{F_{c1}(j)}{m(j)} \right] dj$$

$$= w_0^2 + \frac{2gz}{n_{md} g_e} - 2K_R \int_0^z \frac{F_{c1}(j)}{m(j)} \, dj \quad (A37)$$

Equations (A32) and (A36) apply until z reaches a value z_s , at which payload penetration (if any) starts. The start of penetration is defined by equation (A18) with equations (A23), (A34), and (A36). Thus,

$$\frac{\sigma_{pok}}{\sigma_0} = \left(\frac{R}{R_p} \right)^2 \frac{F_{c1}(z)}{m(z)} \quad (A38)$$

and penetration starts ($z = z_s$) if and when σ_{pok} reaches σ_0 (providing the payload is not attached to the crushable material).

At the start of penetration, it becomes convenient to introduce three new variables and one constant as follows:

$$\left. \begin{aligned}
 y &\equiv \frac{q}{R_p} = z \frac{R}{R_p} \\
 x &\equiv t \sqrt{\frac{n_{md} g_e}{R_p}} \\
 e &\equiv \frac{q_p - q}{\epsilon_k R_p} \\
 K_p &\equiv \frac{\pi R_p^2 \sigma_0}{m_{po} n_{md} g_e} \equiv K_R \left(\frac{R_p}{R} \right)^2
 \end{aligned} \right\} \quad (A39)$$

The initial conditions for penetration are

$$\left. \begin{aligned}
 y(x=0) &\equiv y_s \equiv z_s \frac{R}{R_p} \\
 \left(\frac{dy}{dx} \right)_{x=0} &\equiv \left(\frac{dy}{dx} \right)_s \equiv w_s \sqrt{\frac{R}{R_p}} \\
 e(x=0) &\equiv e_s = 0 \\
 \left(\frac{de}{dx} \right)_{x=0} &\equiv \left(\frac{de}{dx} \right)_s = 0
 \end{aligned} \right\} \quad (A40)$$

where w_s is the value of w determined by equation (A37) at $z = z_s$.

During penetration, equations (A20) apply, with equations (A21), (A22), (A29), (A36), and (A39). Thus

$$\left. \begin{aligned}
 -\frac{n_p}{n_{md}} &= \epsilon_k \frac{d^2 e}{dx^2} + \frac{d^2 y}{dx^2} = \frac{g}{n_{md} g_e} - \frac{(\pi R_p^3 \rho_{ck} \epsilon_k / m_{po}) (de/dx)^2 + K_p F_{po}(e)}{m_{pen}(e)} \\
 \frac{d^2 y}{dx^2} &= \frac{g}{n_{md} g_e} - \frac{K_R F_{cl}(y) - K_p F_{po}(e)}{m_{cr}(y, e)}
 \end{aligned} \right\} \quad (A41)$$

where $F_{c1}(y)$ is determined by equation (A36) with $(R_p/R)y$ substituted for z ; $m_{pen}(e)$ is the dimensionless total penetrating mass in figure 4(c) defined by

$$m_{pen}(e) \equiv \frac{m_{po} + m_{p1}}{m_{po}} = 1 + \frac{3}{4} \left(\frac{\rho_{ck}}{\rho_p} \right) e \quad (A42)$$

with

$$\rho_p \equiv \frac{m_{po}}{(4/3) \pi R_p^3} \quad (A43)$$

$m_{cr}(y,e)$ is the dimensionless crushable mass in figure 4(c) defined by

$$m_{cr}(y,e) \equiv \frac{m_{co} - m_{c1} - m_{p1}}{m_{po}} = \frac{m_{co}}{m_{po}} - \frac{1}{4\epsilon_k} \left(\frac{\rho_{ck}}{\rho_p} \right) y^2 \left(3 \frac{R}{R_p} - y \right) - \frac{3}{4} \left(\frac{\rho_{ck}}{\rho_p} \right) e \quad (A44)$$

and $F_{po}(e)$ is the dimensionless crushing force on $m_{pen}(y_p,y)$ defined by

$$F_{po}(e) \equiv \frac{1}{\pi R_p^2 \sigma_o} \int_{A_{poh}} \int \sigma \, dA = 2 \int_0^1 \frac{(e s_p + 1) s_p \, ds_p}{\sqrt{2e s_p + e^2 + 1}} \quad (A45)$$

with $s_p \equiv b_p/R_p$.

Equations (A32), (A37), (A40), and (A41) are the required governing equations and initial conditions. With rebound excluded and with no payload penetration, the impact is terminated ($z = z_{max}$) when $w = 0$. Thus

$$w(z_{max}) = 0 \quad (A46)$$

With rebound excluded but payload penetration present, the impact is terminated ($y = y_{max}$ and $y + \epsilon_k e = (y + \epsilon_k e)_{max}$) when $dy/dx = 0$ and $dy/dx + \epsilon_k (de/dx) = 0$. Since e increases monotonically with time for the present examples, the termination condition becomes

$$\left. \begin{aligned} \left(\frac{dy}{dx} \right)_{y=y_{max}} &= 0 \\ \left(\frac{de}{dx} \right)_{e=e_{max}} &= 0 \end{aligned} \right\} \quad (A47)$$

As the payload begins to penetrate the crushable material, equations (A41) are integrated simultaneously. This continues until the first of

equations (A47) is satisfied, thereby providing initial conditions for the next phase of the problem. In this next phase, the second of equations (A41) can be ignored and the first equation solved alone. The uncoupled solution of the first of equations (A41) continues until the second of equations (A47) is satisfied.

Simplifications for Constant Mass, Infinitely Thin Crushed Material, and/or Constant Penetration Resistance

The governing equations are now written with constant mass ($\rho_{ck} = 0$). Equations (A32) and (A34) are combined to give

$$-\frac{n_p}{n_{md}} = \frac{1}{2} \frac{d(w^2)}{dz} = \frac{g}{n_{md}g_e} - K_R \frac{F_{cl}(z)}{1 + (m_{co}/m_{po})} \quad (A48)$$

where $F_{cl}(z)$ is given by equation (A36). Equation (A37) becomes

$$\begin{aligned} w^2 &= w_0^2 + 2 \int_0^z \frac{1}{2} \frac{d(w^2)}{dj} dj = w_0^2 + 2 \int_0^z \left[\frac{g}{n_{md}g_e} - K_R \frac{F_{cl}(j)}{1 + (m_{co}/m_{po})} \right] dj \\ &= w_0^2 + \frac{2gz}{n_{md}g_e} - \frac{2K_R}{1 + (m_{co}/m_{po})} \int_0^z F_{cl}(j) dj \end{aligned} \quad (A49)$$

and equation (A38) gives

$$\frac{\sigma_{pok}}{\sigma_o} = \left(\frac{R}{R_p} \right)^2 \frac{F_{cl}(z)}{1 + (m_{co}/m_{po})} \quad (A50)$$

After payload penetration starts, equations (A41) apply, and $\rho_{ck} = 0$ gives

$$\left. \begin{aligned} -\frac{n_p}{n_{md}} &= \epsilon_k \frac{d^2e}{dx^2} + \frac{d^2y}{dx^2} = \frac{g}{n_{md}g_e} - K_p F_{po}(e) \\ \frac{d^2y}{dx^2} &= \frac{g}{n_{md}g_e} - \frac{K_R F_{cl}(y) - K_p F_{po}(e)}{m_{co}/m_{po}} \end{aligned} \right\} \quad (A51)$$

where $F_{cl}(y)$ is given by equation (A36) with $y(R_p/R)$ substituted for z and where $F_{po}(e)$ is given by equation (A45).

Regardless of whether $\rho_{ck} = 0$ or $\rho_{ck} \neq 0$, equation (A36) is greatly simplified by the specialization to $\epsilon_k = 1$ (infinitely thin crushed material).

Thus, for $\epsilon_k = 1$, equation (A36) can be integrated; and $z = y(R_p/R)$ can be substituted as follows:

$$\left. \begin{aligned} F_{c1}(z) &= 2z(1 - z) \\ F_{c1}(y) &= 2\left(\frac{R_p}{R}\right)y\left(1 - y\frac{R_p}{R}\right) = 2\left(\frac{R_p}{R}\right)^2 y\left(\frac{R}{R_p} - y\right) \end{aligned} \right\} \quad (A52)$$

Regardless of whether $\rho_{ck} = 0$ or $\neq 0$ and whether $\epsilon_k = 1$ or $\neq 1$, equation (A45) is greatly simplified by the assumption that the payload stress and force maintain their initial penetration values throughout the penetration stroke, that is, the assumption that $F_{po}(e)$ can be represented by $F_{po}(0)$, which is unity. Thus, the assumption has the form

$$F_{po}(e) = F_{po}(0) = 1 \quad (A53)$$

Equations (A52) and (A53) can be used individually or together in the governing equations for $\rho_{ck} \neq 0$ or for $\rho_{ck} = 0$ whenever the simplifying assumptions are appropriate.

If the assumption of equation (A53) is made (constant penetration resistance) and if $\rho_{ck} = 0$ (constant mass), equations (A41) can be decoupled by a change of variable, regardless of whether $\epsilon_k = 1$ or $\neq 1$, as can equations (A51), which are specialized for $\rho_{ck} = 0$. The governing equations (A48) through (A51) will be rewritten, however, for $\epsilon_k = 1$, that is, equations (A52), as well as the assumption of equation (A53). The change of variables is

$$\left. \begin{aligned} y &\equiv \frac{q}{R_p} \equiv z \frac{R}{R_p} \\ v &\equiv \frac{dq/dt}{\sqrt{n_{md}g_e R_p}} \equiv \frac{U}{\sqrt{n_{md}g_e R_p}} \equiv \frac{dy}{dx} \equiv w \sqrt{\frac{R}{R_p}} \\ y_p &\equiv \frac{q_p}{R_p} \equiv \epsilon_k e + y = e + y \\ v_p &\equiv \frac{dq_p/dt}{\sqrt{n_{md}g_e R_p}} \equiv \epsilon_k \frac{de}{dx} + \frac{dy}{dx} \equiv \frac{dy_p}{dx} = \frac{de}{dx} + \frac{dy}{dx} \end{aligned} \right\} \quad (A54)$$

With the first and second of equations (A54) and the first of equations (A52), as well as equation (A39), equation (A48) becomes

$$-\frac{n_p}{n_{md}} = \frac{1}{2} \frac{d(v^2)}{dy} = \frac{g}{n_{md}g_e} - 2K_p \frac{y[(R/R_p) - y]}{1 + (m_{co}/m_{po})} \quad (A55)$$

Equation (A55) integrates immediately to

$$v^2 = v_o^2 + 2 \int_0^y \frac{1}{2} \frac{d(v^2)}{d\xi} d\xi = v_o^2 + \frac{2gy}{n_{md}g_e} - \frac{2K_p y^2 [(R/R_p) - (2/3)y]}{1 + (m_{co}/m_{po})} \quad (A56)$$

The same substitution in equation (A50) gives

$$\frac{\sigma_{pok}}{\sigma_o} = \left(\frac{R}{R_p} \right)^2 \frac{2(R_p/R)y[1 - (R_p/R)y]}{1 + (m_{co}/m_{po})} \quad (A57)$$

and equations (A55) and (A56) apply until payload penetration starts at $\sigma_{pok}/\sigma_o = 1$ in equation (A57), which then becomes

$$y_s^2 - \frac{R}{R_p} y_s + \frac{1}{2} \left(1 + \frac{m_{co}}{m_{po}} \right) = 0 \quad (A58)$$

where y_s is the dimensionless displacement at the start of penetration.

After penetration begins, equations (A51) apply. They become, with equations (A52), (A53), and (A54),

$$\left. \begin{aligned} -\frac{n_p}{n_{md}} &= \frac{1}{2} \frac{d(v_p^2)}{dy_p} = \frac{g}{n_{md}g_e} - K_p \\ \frac{1}{2} \frac{d(v^2)}{dy} &= \frac{g}{n_{md}g_e} - \frac{K_p \{ 2y[(R/R_p) - y] - 1 \}}{m_{co}/m_{po}} \end{aligned} \right\} \quad (A59)$$

Equations (A59) are uncoupled. The first equation integrates immediately to

$$v_p^2 = v_s^2 + 2 \left(\frac{g}{n_{md}g_e} - K_p \right) (y_p - y_s) \quad (A60)$$

and the second to

$$v^2 = v_s^2 + 2 \left\{ \frac{g}{n_{md}g_e} + \frac{K_p}{m_{co}/m_{po}} \left[1 - \frac{R}{R_p} (y + y_s) + \frac{2}{3} (y^2 + yy_s + y_s^2) \right] \right\} (y - y_s) \quad (A61)$$

where v_s is the dimensionless velocity corresponding to y_s .

Equations (A55) through (A61) are the governing equations for infinitely thin crushed material ($\epsilon_k = 1$) and constant mass ($\rho_{ck} = 0$), with the assumption of constant penetration resistance ($F_{po}(e) = 1$) required after payload

penetration but not before. In the absence of penetration, equation (A56) can be used to determine y_{\max} by setting $v = 0$. Thus y_{\max} is the solution of the cubic equation

$$\frac{2K_p y_{\max}^2 \left[(R/R_p) - (2/3)y_{\max} \right]}{1 + (m_{co}/m_{po})} - \frac{2gy_{\max}}{n_{md}g_e} - v_o^2 = 0 \quad (A62)$$

The dimensionless velocity v_s at which penetration starts (if any) can be determined by writing equation (A56) as

$$v_s^2 = v_o^2 + \frac{2gy_s}{n_{md}g_e} - \frac{2K_p y_s^2 \left[(R/R_p) - (2/3)y_s \right]}{1 + (m_{co}/m_{po})} \quad (A63)$$

where y_s is the solution of equation (A58). Then the maximum payload dimensionless displacement $y_{p\max}$ with penetration is determined by equations (A60) and (A63) with $v_p = 0$ as

$$y_{p\max} = \frac{v_o^2 + 2K_p y_s \left(1 - \left\{ y_s \left[(R/R_p) - (2/3)y_s \right] / [1 + (m_{co}/m_{po})] \right\} \right)}{2[K_p - (g/n_{md}g_e)]} \quad (A64)$$

A similar procedure with equations (A61) and (A63) and with $v = 0$ gives y_{\max} as the solution of the cubic equation.

$$\begin{aligned} \frac{2K_p}{m_{co}/m_{po}} \left\{ \frac{2}{3} (y_{\max}^2 + y_{\max}y_s + y_s^2) - \frac{R}{R_p} (y_{\max} + y_s) + 1 \right\} (y_{\max} - y_s) \\ (y_{\max} - y_s) + \frac{2gy_{\max}}{n_{md}g_e} + v_o^2 - \frac{2K_p y_s^2 \left[(R/R_p) - (2/3)y_s \right]}{1 + (m_{co}/m_{po})} = 0 \end{aligned} \quad (A65)$$

It should be noted that $y_{p\max}$ is generally sufficient for design problems involving payload penetration and that equation (A65) for y_{\max} is included only for completeness and possible checking purposes.

APPENDIX B

SAMPLE CALCULATION FOR DESIGN BY SIMPLIFIED MODEL

WITHOUT PAYLOAD PENETRATION

Under the assumptions that $\rho_{ck} = 0$, $\epsilon_k = 1$, and $g = 0$ (simplified model), a calculation is performed in this appendix to yield a design of a crushable casing for the following conditions:

$$U_o = 300 \text{ ft/sec}$$

$$\epsilon_d = 0.7$$

$$\epsilon_m = 0.8$$

$$n_{p_{\max}} = 2000$$

$$W_{po} = m_{po}g_e = 100 \text{ lb}$$

$$R_p = 0.6 \text{ ft}$$

Payload penetration prevented by bonding
if necessary

The calculation corresponds to case 1 in table 1, as indicated by the last four of the above conditions. The calculation follows:

$$\frac{U_o^2}{(n_{p_{\max}}g_e)R_p} = \frac{(300)^2}{(2000)(32.17)(0.6)} = 2.331$$

From figure 8 for $\epsilon_d = 0.7$

$$\frac{R_p}{R} = 0.286 \quad \text{or} \quad R = \frac{0.6}{0.286} = 2.097 \text{ ft}$$

From figure 9 for $\epsilon_d = 0.7$ with $R_p/R = 0.286$,

$$J_{m\sigma} = 2.74$$

$$\text{check: } \frac{U_o^2}{(n_{p_{\max}}g_e)R} = (2.331)(0.286) = 0.6665$$

From figure 6

$$z_{\max} = \frac{q_{\max}}{R} = 0.500$$

or

$$q_{\max} = 0.500(2.097) = 1.049 \text{ ft}$$

From figure 7 for $\epsilon_d = 0.7$

$$J_{m\sigma} = 2.74 \text{ (check is perfect to 3 places; therefore use 2.74)}$$

From figure 12 with $R_p/R = 0.286$,

$$N_{m\sigma} = 55.5$$

$$\epsilon_m J_{m\sigma} = 0.8(2.74) = 2.192$$

$$\frac{g\epsilon_d}{U_o^2} = \frac{32.17(0.7)}{(300)^2} = 2.503 \times 10^{-4} \text{ ft}^{-1}$$

$$\frac{J_{m\sigma} W_{po}}{N_{m\sigma} \pi R_p^3 (144)} = \frac{(2.74)(100)}{(55.5)\pi(0.216)(144)} = 0.5053 \times 10^{-1} \text{ psi/ft}$$

From equation (27) with σ_o in psi

$$SEA = \frac{2.192}{2.503 \times 10^{-4} - (0.5053 \times 10^{-1} / \sigma_o)} \text{ ft-lb/lb}$$

Now decide which material to use in figure 5 (trial eliminates the balsa-like class, which is too strong for low payload weight). From figure 5 for honeycomb-like material,

$$\text{try } SEA = 10,400 \text{ ft-lb/lb at } \sigma_o = 1,000 \text{ psi}$$

$$SEA = \frac{2.192 \times 10^4}{2.503 - 0.5053} = 10,960 \text{ ft-lb/lb}$$

$$\text{try } SEA = 10,870 \text{ ft-lb/lb at } \sigma_o = 1,100 \text{ psi}$$

$$SEA = \frac{2.192 \times 10^4}{2.503 - 0.459} = 10,720 \text{ ft-lb/lb}$$

$$\text{try } SEA = 10,800 \text{ ft-lb/lb at } \sigma_o = 1,090 \text{ psi}$$

$$SEA = \frac{2.192 \times 10^4}{2.503 - 0.463} = 10,750 \text{ ft-lb/lb}$$

try SEA = 10,770 ft-lb/lb at $\sigma_0 = 1,080$ psi

$$SEA = \frac{2.192 \times 10^4}{2.503 - 0.468} = 10,770 \text{ ft-lb/lb}$$

therefore

$$\sigma_0 = 1,080 \text{ psi}$$

$$SEA = 10,770 \text{ ft-lb/lb}$$

From equation (8), with σ_0 in psi and SEA in ft-lb/lb

$$\rho_{cm} g_e = \frac{\epsilon_m (144 \sigma_0)}{SEA} = \frac{(0.8) (144) (1,080)}{10,770} = 11.55 \text{ lb/ft}^3$$

From equation (17)

$$\frac{m_{co}}{m_{po} + m_{co}} = \frac{J_{m\sigma} U_o^2 \epsilon_m}{g_e (SEA) \epsilon_d} = \frac{(2.74) (300)^2 (0.8)}{(32.17) (10,770) (0.7)} = 0.8135$$

$$\frac{m_{po}}{m_{co}} = \frac{1}{0.8135} - 1 = 1.229 - 1 = 0.229$$

$$\frac{m_{co}}{m_{po}} = 4.366$$

therefore

$$W_{co} = 4.366 (100) = 436.6 \text{ lb}$$

$$W_{po} + W_{co} = 100 + 436.6 = 536.6 \text{ lb}$$

Check by recalculating $\rho_{cm} g_e$. From equation (25),

$$\rho_{cm} g_e = \frac{W_{co}}{N_{m\sigma} \pi R_p^3} = \frac{436.6}{(55.5) (\pi) (0.216)} = 11.58 \text{ lb/ft}^3$$

(Check is adequate: use 11.56 lb/ft³.) Check to see if bonding is necessary to prevent payload penetration

$$\left(\frac{R_p}{R} \right)^2 \left(1 + \frac{m_{co}}{m_{po}} \right) = (0.286)^2 (5.366) = 0.4386$$

From figure 10

$$z_s = 0.325$$

$$\frac{z_{\max}}{z_s} = \frac{q_{\max}}{q_s} = \frac{q_{p\max}}{q_s} = \frac{0.500}{0.325} = 1.538 > 1.000$$

Therefore bonding is necessary to prevent payload penetration.

APPENDIX C

SAMPLE CALCULATION FOR DESIGN BY SIMPLIFIED MODEL WITH PAYLOAD PENETRATION

A sample calculation is given for an approximate design of a crushable casing under the assumptions that $\rho_{ck} = 0$, $\epsilon_k = 1$, and $g = 0$ (simplified model) together with $F_{po}(e) = 1$ for penetration. The design conditions are the following:

$$U_o = 300 \text{ ft/sec}$$

$$\epsilon_d = 0.7$$

$$\epsilon_m = 0.8$$

$$n_{p_{\max}} \leq 2000$$

$$\sigma_o = 1200 \text{ psi for balsa-like material}$$

$$W_{po} = m_{po} g_e = 450 \text{ lb}$$

$$R_p = 1.2 \text{ ft}$$

Payload penetration permitted (unbonded)

The last four conditions indicate that case 11 of table 1 is being calculated. From figure 5 for balsa-like material,

$$SEA = 24,000 \text{ ft-lb/lb}$$

From equation (8), with σ_o in psi and SEA in ft-lb/lb

$$\rho_{cm} g_e = \frac{\epsilon_m (144 \sigma_o)}{SEA} = \frac{(0.8) (144) (1,200)}{24,000} = 5.76 \text{ lb/ft}^3$$

From equation (22) with σ_o in psi (for penetration)

$$n_{p_{\max}} = \frac{\pi R_p^2 (144 \sigma_o)}{m_{po} g_e} = \frac{\pi (1.44) (144) (1,200)}{450} = 1,737$$

For iteration with figures 11 and 12, calculate

$$\frac{1}{2\epsilon_d} \left(\frac{U_o^2}{n_{p_{\max}} g_e R_p} \right) = \frac{1}{1.4} \frac{(300)^2}{(1737) (32.17) (1.2)} = 0.959$$

$$1 + 0.959 = 1.959$$

$$(1 + 0.959)^2 = 3.838$$

$$\frac{\text{SEA}}{n_{p\max} \epsilon_m R_p} = \frac{24,000}{1737(0.8)(1.2)} = 14.385$$

$$\text{first } \frac{m_{co}}{m_{po}} = 1.0 \text{ (guess)}$$

$$\text{first } N_{\mu} = \frac{1 + 1.0}{3.838} = 0.5213$$

From figure 11 for $\epsilon_d = 0.7$

$$\text{first } N_{RU} = 0.8435$$

$$\text{first } \frac{R_p}{R} = \frac{0.8435}{1.959} = 0.4306$$

From figure 12

$$\text{first } N_{m\sigma} = 15.5$$

$$\text{second } \frac{m_{co}}{m_{po}} = \frac{15.5}{14.385} = 1.078$$

$$\text{second } N_{\mu} = \frac{1 + 1.078}{3.838} = 0.5415$$

From figure 11 for $\epsilon_d = 0.7$

$$\text{second } N_{RU} = 0.838$$

$$\text{second } \frac{R_p}{R} = \frac{0.838}{1.959} = 0.4278$$

From figure 12

$$\text{second } N_{m\sigma} = 15.75$$

$$\text{third } \frac{m_{co}}{m_{po}} = \frac{15.75}{14.385} = 1.095$$

$$\text{third } N_{\mu} = \frac{1 + 1.095}{3.838} = 0.5460$$

From figure 11 for $\epsilon_d = 0.7$

$$\text{Third } N_{RU} = 0.8368$$

$$\text{Third } \frac{R_p}{R} = \frac{0.8368}{1.959} = 0.4273$$

From figure 12

$$\text{third } N_{m\sigma} = 15.75 \text{ (same as second)}$$

$$\frac{R_p}{R} = 0.4273, \quad R = \frac{1.2}{0.4273} = 2.807 \text{ ft}$$

$$\frac{m_{co}}{m_{po}} = 1.095$$

$$W_{co} = 450(1.095) = 493 \text{ lb}$$

$$W_{po} + W_{co} = 450 + 493 + 943 \text{ lb}$$

Check by recalculating $\rho_{cm} g_e$

From equation (25)

$$\rho_{cm} g_e = \frac{W_{co}}{N_{m\sigma} \pi R_p^3} = \frac{493}{(15.75)(\pi)(1.728)} = 5.767 \text{ lb/ft}^3$$

(Check is adequate: use 5.76 lb/ft³)

Check that penetration occurs for this m_{co}/m_{po} and R_p/R

$$\left(\frac{R_p}{R}\right)^2 \left(1 + \frac{m_{co}}{m_{po}}\right) = (0.4273)^2 (1 + 1.095) = 0.3825$$

From figure 10

$$z_s = 0.257$$

From equation (5) with $L = 0$

$$z_{p\max} = \epsilon_d \left(1 - \frac{R_p}{R}\right) = 0.7(0.5727) = 0.40089$$

$$\frac{z_{p\max}}{z_s} \equiv \frac{q_{p\max}}{q_s} = \frac{0.40089}{0.257} = 1.56 > 1.000$$

Therefore penetration does occur

APPENDIX D

COMPUTER PROCEDURES FOR THE GOVERNING EQUATIONS WITH SPHERICAL GEOMETRY

The computer procedures described for spherical geometry in this appendix form an essential part of the so-called "detailed" analytical model but can also be specialized for a variety of less detailed models. There are three computer procedures.

BASIC COMPUTER PROCEDURE

The first computer procedure described is the "basic" procedure. It cannot be regarded as a design since it contains no provision for automatic determination of crushable casing parameters to achieve a desired acceleration and/or a desired ratio of stroke to available stroke. The primary purpose of the basic procedure, then, is to check the adequacy of designs which have been determined by other means (for example, designs determined by the simplified model employing figs. 5 through 12).

With symbols defined in the section on notation or in parentheses, the basic procedure contains the following steps:

1. Input and print the following: case number, W_{po} , R_p , U_0 , ϵ_d , ϵ_m , n_{md} , g_e , g_L , g_m (value of g for equation of motion), g_a (value of g for acceleration ratio), ϵ_{km} (value of ϵ_k for equation of motion), ϵ_{ka} (value of ϵ_k for acceleration ratio), ϵ_{ks} (value of ϵ_k for stress ratio), $\rho_{ckm}g_e$ (value of $\rho_{ck}g_e$ for equation of motion), $\rho_{cka}g_e$ (value of $\rho_{ck}g_e$ for acceleration ratio), $\rho_{cks}g_e$ (value of $\rho_{ck}g_e$ for stress ratio), $F_{pom}(e)$ (value of $F_{po}(e)$ for equation of motion), $F_{poa}(e)$ (value of $F_{po}(e)$ for acceleration ratio). Also input and print trial values of R and σ_0 . Finally, input and print whether the payload is considered perfectly bonded or perfectly unbonded to the crushable material, whether the SEA is computed from σ_0 or selected, whether the material is considered to be balsa-like or honeycomb-like (important only if SEA computed), and the value of SEA if selected. Note that $\rho_{ckm}g_e$, $\rho_{cka}g_e$, or $\rho_{cks}g_e$ often is specified as $\rho_{cm}g_e$, to be calculated in step 2. Note also that $F_{pom}(e)$ and $F_{poa}(e)$ is specified as a constant, usually 1.00, or as the integral of equation (A45).

2. Calculate and print the following constants: ρ_{pge} (from eq. (A43) with $m_{po} = W_{po}/g_e$), SEA (from eq. (9) if calculated for balsa-like or eq. (10) if calculated for honeycomb-like), $\rho_{cm}g_e$ (from eq. (8) with factor for dimensions), W_{co} (from $W_{co} = (4/3)\pi(R^3 - R_p^3)\rho_{cm}g_e$), $W_{co} + W_{po}$, $g_m/n_{md}g_e$, $g_a/n_{md}g_e$, w_0^2 (from the first of eqs. (A33)), K_R (from the last of

eqs. (A33) with $m_{po} = W_{po}/g_e$ and a factor for dimensions), and $\rho_{pr}g_e$ (from eq. (A35) with $m_{po} = W_{po}/g_e$).

3. Generate and print values of F_{c1m} (from eq. (A36) with ϵ_{km} of step 1) and w^2 (from the equation of motion, eq. (A37), with eq. (A34) and with ϵ_{km} , g_m , and ρ_{ckm} of step 1) for selected values of z ($z \equiv q/R$). Terminate the integrations at the lowest positive value of w^2 when z is varying by increments of 0.0001. Print this value of z separately and label it $z_{p_{max}}$ without penetration. Calculate L/R according to equation (5) with $z_{p_{max}} = q_{p_{max}}/R$, print it separately, and label it L/R without penetration.

4. Generate and print values of F_{c1s} (from eq. (A36) with ϵ_{ks} of step 1) and the stress ratio σ_{pok}/σ_o (from eq. (A38) with eq. (A34) and with ϵ_{ks} and ρ_{cks} of step 1) for selected values of z . With z varying by increments of 0.0001, terminate the calculations at $z = 1.00$ or at the lowest positive value of $1 - (\sigma_{pok}/\sigma_o)$, whichever occurs at a lower z value. Print the termination value of z separately and label it z_s . Calculate $z_{p_{max}}/z_s$, print it separately, and label it $z_{p_{max}}/z_s$ without penetration.

5. Generate and print values of F_{c1a} (from eq. (A36) for ϵ_{ka} of step 1) and deceleration ratio n_p/n_{md} (from eq. (A32) with eq. (A34) and with ϵ_{ka} , g_a , and ρ_{cka} from step 1) for selected values of z . Terminate the calculations at $z_{p_{max}}$ without penetration.

6. If the payload is bonded or if $z_{p_{max}}/z_s \leq 1.00$ without penetration, terminate the program at step 5. If the payload is unbonded and if $z_{p_{max}}/z_s > 1.00$ without penetration, proceed into the penetration phase. For penetration, calculate the constant K_p according to the last of equations (A39) and calculate four initial conditions according to equations (A40).

7. Generate and print values of y , e , dy/dx , and de/dx for selected values of x ($x \equiv t/\sqrt{n_{md}g_e/R_p}$) by integrating the two simultaneous ordinary differential equations (A41), with auxiliary equations (A42) through (A45), with initial conditions described in step 6, with $F_{c1m}(y)$ determined as in step 3 when $(R_p/R)y$ is substituted for z , with $F_{pom}(e)$ being the integral of equation (A45) or a constant according to the specification in step 1, and with ϵ_{km} , g_m , and ρ_{ckm} being the values of step 1. Terminate the integration when dy/dx is zero to four or more decimal places and when successive values agree to four or more significant figures for the worst of y , e , and de/dx . The corresponding value of y is called y_{max} , and the corresponding values of e and de/dx are initial conditions for the next phase of the problem.

8. With the initial conditions just described, generate and print values of e and de/dx for selected values of x by integrating the first of equations (A41) with $d^2y/dx^2 \equiv 0$. Terminate the integration when de/dx is zero to four or more decimal places and when successive values of e agree to four or more significant figures. The corresponding value of e is called

e_{\max} . Calculate $z_{p_{\max}}$ from $z_{p_{\max}} = (R_p/R)(y_{\max} + \epsilon_{km}e_{\max})$, as deducible from equations (A39) with $z_p = q_p/R$. Also calculate L/R from equation (5), and calculate $z_{p_{\max}}/z_s$. Print $z_{p_{\max}}$, L/R , and $z_{p_{\max}}/z_s$ labeled "with penetration."

9. Generate and print values of the deceleration ratio n_p/n_{md} for selected values of x according to the first of equations (A41) with auxiliary equations (A42), (A43), and (A45). The quantity $F_{poa}(e)$ is the integral of equation (A45) or a constant according to the specification in step 1; and ϵ_{ka} , g_a , and ρ_{cka} are the values of step 1. Step 9 terminates the basic procedure when penetration is present.

SEARCH FOR OVERALL RADIUS R

The second computer procedure described is a design procedure in which σ_0 is assumed given but iterations are automatically performed to determine R for a desired ratio of stroke to available stroke. The desired ratio is unity in the present case, that is, $L/R = 0$; but the available stroke leaves a margin of safety based on the fictitious compacting strain ϵ_d .

This procedure is based partially on a modified basic procedure. The modifications include the specification of n_{des}/n_{md} (i.e., the desired value of $n_{p_{\max}}/n_{md}$) and the determination and printout of z_a (i.e., the value of z at $n_p = n_{p_{\max}}$) and β (i.e., $(n_{p_{\max}}/n_{des}) - 1$). The quantity β is calculated as a measure of the acceleration discrepancy.

The next step is to iterate the modified basic procedure just described in order to achieve a low value of L/R . As a start, the procedure is run for two values of R , the selection being based on the design charts, figures 6 through 9, or any other analytical or experimental information suggesting low values of L/R . The results are labeled $(L/R)_1$ for R_1 and $(L/R)_2$ for R_2 . Then the iteration is based on successive straight lines of the form:

$$L/R = aR + b \quad (D1)$$

For the starting values $(L/R)_1$, R_1 and $(L/R)_2$, R_2 , the first pair of straight lines from equation (D1) is

$$(L/R)_1 = a^{(1)}R_1 + b^{(1)}$$

$$(L/R)_2 = a^{(1)}R_2 + b^{(1)}$$

and the computer determines $a^{(1)}$ and $b^{(1)}$ by solving the two simultaneous equations. From equation (D1) for $L/R = 0$ (which is the desired value), the computer then determines $R^{(1)}$ as

$$R^{(1)} = -[b^{(1)}/a^{(1)}]$$

Then $R^{(1)}$ is run through the modified basic procedure to determine $(L/R)^{(1)}$. This result is combined with the two starting values, and the two having the lowest absolute values of L/R are selected for a new pair of starting values. The process is repeated until

$$|L/R| < 0.0005$$

provided that each new value of $|L/R|$ is lower than at least one of its two starting values.

If a new value of $|L/R|$ is higher than either of its starting values, the computing machine is stopped, and new starting values must be selected. This did not happen for any of the cases reported herein, all of which converged rapidly (requiring an average of 0.17 min of execute time per case without penetration and 4.55 min for the detailed model with penetration). In contrast, there was one unrelated case that did not converge. For this case, however, convergence could not have been expected. It turned out that the given impact velocity was too high for a feasible energy absorbing design with the given material, and hence too high for a solution.

SEARCH FOR OVERALL RADIUS R AND CRUSHING STRESS σ_0

The third computer procedure used herein is a search for R and σ_0 , which is simply an extension of the search for R just described (except that penetration is not included since eq. (28) determines σ_0 for penetration). In the search for R and σ_0 , both R and σ_0 are varied in an attempt not only to make $L/R = 0$ but also to make $\beta = 0$, where $\beta = 0$ when the maximum acceleration load factor $n_{p_{\max}}$ equals the desired load factor n_{des} .

This additional requirement, $\beta = 0$, makes the iterations more complicated than before although the modified basic procedure to be iterated is the same. This time the starting values are found by running the basic procedure for three combinations of R and σ_0 . Again, one of the starting values can be determined by the design charts for the simplified model, figures 6 through 9, together with modifications based on experience for other models and/or other preliminary information (such as analyses or experiments performed on similar configurations). Experience indicates that the other two starting values should be small deviations from the first in which the higher values of σ_0 correspond to the lower values of R . The starting values are labeled $(L/R)_1$ and β_1 for R_1 and σ_{01} , $(L/R)_2$ and β_2 for R_2 and σ_{02} , and $(L/R)_3$ and β_3 for R_3 and σ_{03} . The iterations are based on successive pairs of planar surfaces having the form

$$L/R = a_{L\sigma}\sigma_0 + a_{LR}R + a_L \quad (D2)$$

$$\beta = a_{\beta\sigma}\sigma_0 + a_{\beta R}R + a_\beta \quad (D3)$$

For the three sets of starting values just labeled, the first group of three planes from equation (D2) is

$$\left(\frac{L}{R}\right)_1 = a_{L\sigma}^{(1)} \sigma_{O1} + a_{LR}^{(1)} R_1 + a_L^{(1)}$$

$$\left(\frac{L}{R}\right)_2 = a_{L\sigma}^{(1)} \sigma_{O2} + a_{LR}^{(1)} R_2 + a_L^{(1)}$$

$$\left(\frac{L}{R}\right)_3 = a_{L\sigma}^{(1)} \sigma_{O3} + a_{LR}^{(1)} R_3 + a_L^{(1)}$$

and the computer solves the three simultaneous equations to determine $a_{L\sigma}^{(1)}$, $a_{LR}^{(1)}$, and $a_L^{(1)}$. Similarly, the first group of three planes from equation (D3) is

$$\beta_1 = a_{\beta\sigma}^{(1)} \sigma_{O1} + a_{\beta R}^{(1)} R_1 + a_{\beta}^{(1)}$$

$$\beta_2 = a_{\beta\sigma}^{(1)} \sigma_{O2} + a_{\beta R}^{(1)} R_2 + a_{\beta}^{(1)}$$

$$\beta_3 = a_{\beta\sigma}^{(1)} \sigma_{O3} + a_{\beta R}^{(1)} R_3 + a_{\beta}^{(1)}$$

and the computer determines $a_{\beta\sigma}^{(1)}$, $a_{\beta R}^{(1)}$, and $a_{\beta}^{(1)}$.

Then L/R and β are set equal to the desired value of 0 in equations (D2) and (D3), and the coefficients just determined are substituted to give

$$a_{L\sigma}^{(1)} \sigma_O^{(1)} + a_{LR}^{(1)} R^{(1)} = -a_L^{(1)}$$

$$a_{\beta\sigma}^{(1)} \sigma_O^{(1)} + a_{\beta R}^{(1)} R^{(1)} = -a_{\beta}^{(1)}$$

The computer then solves the two simultaneous equations and determines (hopefully) an improved pair of parameters $\sigma_O^{(1)}$ and $R^{(1)}$.

The parameters $\sigma_O^{(1)}$ and $R^{(1)}$ are introduced into the modified basic procedure to determine the corresponding values of $(L/R)^{(1)}$ and $\beta^{(1)}$. This result is combined with the three sets of starting values, and the three having the lowest values of $|L/R| + |\beta|$ are selected for new starting values. The process is repeated until

$$|L/R| < 0.0005$$

$$|\beta| < 0.0005$$

with the requirement that each new value of $|L/R| + |\beta|$ is lower than at least one of its three starting values.

The computing machine is stopped, analogously to the R search, if a new value of $|L/R| + |\beta|$ is higher than any of its starting values; and new starting values must be selected (where the selection can often be facilitated by a plot having R and σ_0 as axes with values of $|L/R| + |\beta|$ indicated by vectors or with values of L/R and β indicated by vectors). In contrast to the R search, new starting values had to be selected fairly frequently for the search for R and σ_0 (specifically, for roughly one-fourth of the cases), despite the fact that convergence was rapid when it occurred (0.7 min of execute time per case for the detailed model).

For all but one of the cases requiring a new set of starting values, convergence occurred for the second or third set. The exceptional case (not listed in table 1) was an attempt to do the detailed model by the R and σ_0 search so as to match an $n_{p_{\max}}$ of 2000 selected for the simplified model.

For the landing configuration under consideration, however, R searches for different values of σ_0 indicated that an $n_{p_{\max}}$ as high as 2000 cannot be attained with the detailed model. Hence the iterative method would have been wrong if it had converged to an $n_{p_{\max}}$ of 2000 in a search for R and σ_0 .

APPENDIX E

EXACT INTEGRATION FOR A CLASS OF IMPACT PROBLEMS WITH VARIABLE MASS BUT WITHOUT PAYLOAD PENETRATION

The class of impact problems to be considered is shown in figure 3(b). This shows a general vertically symmetrical landing geometry for zero shear resistance and uniform compacting strain with the impact to be described before payload penetration occurs (if any). Equation (A19) defines the problem, and all assumptions leading to that equation are retained.

One additional assumption is introduced, namely, a uniform and isotropic crushing stress ($\sigma = \sigma_k = \text{constant}$). Then equation (A19) becomes

$$\frac{1}{2} d(U^2) = g dq - \frac{\sigma_k (A_{c1h} dq)}{m_{po} + m_{co} - (\rho_{ck} V_c / \epsilon_k)} \quad (E1)$$

where the equation has been multiplied by dq and where V_c has been introduced according to the second of equations (A14).

The area A_{c1h} is the planar area of crushable material that is flush with the landing surface in figure 3(b), and V_c is the volume of the dotted region in figure 3(b). Hence,

$$A_{c1h} dq = dV_c \quad (E2)$$

When equation (E2) is introduced into equation (E1), each term in the latter equation becomes a total differential, and the exact integration is

$$\frac{1}{2} U^2 = gq + \frac{\epsilon_k \sigma_k}{\rho_{ck}} \log_e \left(m_{po} + m_{co} - \frac{\rho_{ck} V_c}{\epsilon_k} \right) + C \quad (E3)$$

where C is a constant of integration. This constant can be evaluated by noting that at $q = 0$, $U = U_0$, and $V_c = 0$. When the evaluated C is introduced in equation (E3), the result is

$$\frac{1}{2} (U_0^2 - U^2) = -gq + \frac{\epsilon_k \sigma_k}{\rho_{ck}} \log_e \frac{1}{1 - \left[\rho_{ck} \int_0^q A_{sh} dh_c / \epsilon_k (m_{po} + m_{co}) \right]} \quad (E4)$$

where V_c has been replaced by $\int_0^g A_{sh} dh_c$ as in the second of equations (A14).

Equation (E4) gives U in terms of q and can be simplified if the gq term is neglected (as is justified for most impacts). Then it is convenient to reintroduce V_c and let it be the only variable on the right-hand side. Thus,

$$\frac{1}{2} (U_o^2 - U^2) = \frac{\epsilon_k \sigma_k}{\rho_{ck}} \log_e \frac{1}{1 - [\rho_{ck} V_c / \epsilon_k (m_{po} + m_{co})]} \quad (E5)$$

When $U = 0$, V_c has reached its maximum value, $V_{c_{max}}$. Thus, with the natural log converted to an exponential:

$$V_{c_{max}} = \frac{\epsilon_k (m_{po} + m_{co})}{\rho_{ck}} \left[1 - e^{-(\rho_{ck} U_o^2 / 2 \epsilon_k \sigma_k)} \right] \quad (E6)$$

It is implicit in the derivation of equation (A13) that $V_c + V_{c1} = V_c / \epsilon_k$, where V_{c1} is the volume of m_{c1} in figure 3(b); and the same relationship applies for the maximum volumes. Hence, if it is desired, equation (E6) can be written

$$V_{c_{max}} + V_{c1_{max}} = \frac{m_{po} + m_{co}}{\rho_{ck}} \left[1 - e^{-(\rho_{ck} U_o^2 / 2 \epsilon_k \sigma_k)} \right] \quad (E7)$$

Equation (E7) agrees exactly with equation (1-4) in appendix A of reference 2 when notational differences are accounted for. The development in reference 2 includes shear resistance implicitly (by showing uplift of the compacted region in a figure) but counteracts the inclusion of shear by assuming A_{c1} to be a horizontal planar area and thereby rendering the shear stresses ineffective in energy absorption. Thus, with the results in agreement and the assumptions reconciled, the development of equations (E4) through (E7) becomes a partial check on the present methods as well as a set of exact results for a special case of variable mass in the absence of payload penetration.

REFERENCES

1. Bresie, Don: Practical Limits for Balsa Impact Limiters. NASA TN D-3175, 1966.
2. Research and Advanced Development Division of Avco Corporation: Conceptual Design Studies of an Advanced Mariner Spacecraft. Volume III Lander Design. RAD-TR-64-36, Contract 950896, Jet Propulsion Lab., Oct. 28, 1964.
3. Carley, W. J.: Mars Entry and Landing Capsule. NASA TM 33-236, 1965.
4. Cundall, Donald R.: Balsa-Wood Impact Limiters for Hard Landing on the Surface of Mars. AIAA/AAS Stepping Stones to Mars Meeting, Baltimore, Maryland, March 28-30, 1966, pp. 302-308.
5. Cloutier, G. J.: Landing Impact Energy Absorption Using Anisotropic Crushable Materials. J. Spacecraft Rockets, vol. 3, no. 12, Dec. 1966, pp. 1755-1761.
6. Berkowitz, Harvey M.; and Rodriguez, David A.: Dynamic Analysis and Development of Response Histories and Tradeoff Study Charts for Spherical Impact Limiters. AIAA/ASME 8th Structures, Structural Dynamics, and Materials Conf., Palm Springs, Calif., March 29-31, 1967, pp. 400-412.
7. Knoell, A. C.: Environmental and Physical Effects on the Response of Balsa Wood as an Energy Dissipator. Technical Rep. 32-944, Jet Propulsion Lab., June 15, 1966.
8. Anon.: Mars Lander Entry Studies. Volume II - System Analysis. Grumman Status Rep., Advanced Space Systems Group, March 1966.
9. Anon.: Mars Probe Final Report. Vol. II - Probe/Lander, Entry From the Approach Trajectory, Book 2 - Mission and System Specifications. Contract NAS1-5224, Avco Space Systems Div., May 11, 1966.
10. Anon.: Final Report for Impact Limiter Design, Fabrication, and Testing. Publ. UG-3934, Lunar and Planetary Programs, Space and Re-Entry Systems Div., Philco-Ford Corp., Jet Propulsion Lab. Contract 951261, Jan. 30, 1967.
11. Matlock, Hudson; Ripperger, E. A.; Turnbow, James W.; and Thompson, J. Neils: Energy Absorbing Materials and Systems. Shock and Vibration Bull., pt. II, Dec. 1957, pp. 305-323.
12. O'Bryan, Thomas C.; and Hatch, Howard G., Jr.: Limited Investigation of Crushable Structures for Acceleration Protection of Occupants of Vehicles at Low Impact Speeds. NASA TN D-158, 1959.

13. Daigle, D. L.; and Lonborg, J. O.: Evaluation of Certain Crushable Materials. Technical Rep. 32-120, Jet Propulsion Lab., Jan. 13, 1961.
14. Bernett, E. C.: Effects of Decontamination, Sterilization, and Preconditioning Treatments of Energy-Dissipating Properties of Balsa Wood. Technical Rep. 32-1022, Jet Propulsion Lab., Nov. 1, 1966.

TABLE 1.- NUMERICAL RESULTS FOR $U_0 = 300$ FT/SEC, $\epsilon_d = 0.7$, $\epsilon_m = 0.8$, AND $\eta_{p_{\max}} \leq 2000$ (a) Balsa-like and honeycomb-like material with $W_{po} = 100$ lb

Case	R_p , ft	ρ_{pge} , lb/ft ³	Bonded	Material (a)	Payload penetration		$\eta_{p_{\max}}$		σ_o , psi		$\rho_{cm} \epsilon_o$, lb/ft ³	
					Simplified (b)	Detailed (c)	Simplified (b)	Detailed (c)	Simplified (b)	Detailed (c)	Simplified (b)	Detailed (c)
1	0.6	110.5	Yes	H	No	No	1999.7	0.9985	1080	1395.0	11.560	13.294
2	.6	110.5	No	H	Yes	No	2000.4	1.0002	1228	1395.8	12.390	13.299
3	.6	110.5	No	B	Yes	Yes	1954	1.0004	1200	1200	5.76	5.7582
4	.7	69.6	No	H	No	No	1999.9	.99995	1118	1437.9	11.82	13.519
5	.7	69.6	No	B	Yes	Yes	1999.9	.99995	902.4	902.4	4.33	4.3315
6	.8	46.6	No	H	No	No	1999.9	.99995	1170	1491.4	12.125	13.796
7	.9	32.7	No	H	No	No	1999.4	1.0004	1251.5	1555.2	12.518	14.119
SEA, ft-lb/lb												
Case	Simplified (b)	Detailed (c)	q_p/q_s		R, ft		W_{co} , lb		R , ft		W_{co} , lb	
			Simplified (b)	Detailed (c)	Simplified (b)	Detailed (c)	Simplified (b)	Detailed (c)	Simplified (b)	Detailed (c)	Simplified (b)	Detailed (c)
1	10.770	12.088	1.1224	1.538	dNon-existent	2.097	2.0073	0.95722	436.6	438.33	1.0040	1.0040
2	11.420	12.091	1.0588	1.410	dNon-existent	2.006	2.0071	1.0005	407.0	438.39	1.0771	1.0771
3	24.000	24.007	1.0003	3.040	2.8774	0.94651	1.810	1.8213	1.0062	138.3	140.50	1.0159
4	10.930	12.253	1.1210	dNon-existent	2.229	2.1322	1.930	.95657	528.6	529.49	1.0017	1.0017
5	24.000	24.000	1.0000	2.466	2.3232	.94209	1.9411	1.0058	125.0	126.47	1.0118	1.0118
6	11.175	12.454	1.1145	dNon-existent	2.360	2.2595	2.3883	.95742	636.0	656.98	1.0015	1.0015
7	11.517	12.689	1.1018	dNon-existent	2.4759	2.3883	.96462	757.65	762.62	1.0066	1.0066	1.0066
$W_{co} + W_{po}$, lb												
Case	Simplified (b)	Detailed (c)	L/R		Simplified (b)		Detailed (c)		Simplified (b)		Detailed (c)	
			Simplified (b)	Detailed (c)	Simplified (b)	Detailed (c)	Simplified (b)	Detailed (c)	Simplified (b)	Detailed (c)	Simplified (b)	Detailed (c)
1	536.6	538.33	1.0032	0.001163	0.000084	0.07223	0.000084	0.07223	0.000084	0.07223	0.000084	0.07223
2	507.0	538.39	1.0619	-.001781	.000210	-.118	-.000210	-.118	-.000210	-.118	-.000210	-.118
3	238.3	240.50	1.0092	-.000087	.000156	-1.56	-.000087	.000156	-.000087	.000156	-.000087	.000156
4	628.6	629.49	1.0014	-.0000614	-.000019	.031	-.0000614	-.000019	-.0000614	-.000019	-.0000614	-.000019
5	225.0	226.47	1.0065	-.000569	.000151	.265	-.000569	.000151	-.000569	.000151	-.000569	.000151
6	736.0	736.98	1.0013	-.000983	-.000067	.068	-.000983	-.000067	-.000983	-.000067	-.000983	-.000067
7	857.65	862.62	1.0058	-.000074	.000312	-4.2	-.000074	.000312	-.000074	.000312	-.000074	.000312

(a) H = honeycomb-like; B = balsa-like.

(b) Design by simplified model employing figures 5-12 (except for cases 7 and 12 and the L/R column, which are machine computer results for simplified model) and assuming $\rho_{ck} = 0$, $\epsilon_k = 1$, $F_{po}(e) = 1$, and $g = 0$.(c) Design by detailed model employing IBM 7094 solution of equations for $\rho_{ck} = \rho_{cm}$, $\epsilon_k = \epsilon_m$, $F_{po}(e) = 2 \int_0^1 \frac{(esp + 1) s_p ds_p}{\sqrt{2esp + e^2 + 1}}$.

(d) Over a hypothetical stroke as large as the outer radius, there is no force developed which is large enough to cause penetration.

TABLE 1.- NUMERICAL RESULTS FOR $U_0 = 300$ FT/SEC, $\epsilon_d = 0.7$, $\epsilon_m = 0.8$, AND $\eta_{pmax} \leq 2000$ - Concluded

(b) Balsalike material with $W_{po} = 450$ lb

Case	R_p , ft	ρ_{pe} , lb/ft ³	Bonded	Material (a)	Payload penetration		η_{pmax}		σ_0 , psi		$\rho_{cm}e$, lb/ft ³	
					Simplified (b)	Detailed (c)	Simplified (b)	Detailed (c)	Simplified (b)	Detailed (c)	Simplified (b)	Detailed (c)
8	1.0	107.4	Yes	B	No	No	1770	1480.5	800	800	3.836	3.8400
9	1.0	107.4	No	B	Yes	Yes	1206	1206.4	1200	1200	5.76	5.7582
10	1.2	62.1	Yes	B	No	No	1840	1555.8	800	800	3.836	3.8400
11	1.2	62.1	No	B	Yes	Yes	1737	1736.8	1200	1200	5.76	5.7582
12	1.4	39.1	Yes	B	No	No	1879.8	1627.6	800	800	3.8400	3.8400
13	1.6	26.2	No	B	No	No	1910	1686.9	800	800	3.836	3.8400

Case	SEA, ft-lb/lb			q_{pmax}/q_s			R, ft			W_{co} , lb		
	Simplified (b)	Detailed (c)	Detailed Simplified	Simplified (b)	Detailed (c)	Detailed Simplified	Simplified (b)	Detailed (c)	Detailed Simplified	Simplified (b)	Detailed (c)	Detailed Simplified
8	24,000	24,000	1.0000	3.456	3.5288	1.0211	2.778	2.9044	1.0455	329.0	378.00	1.1489
9	24,000	24,007	1.0003	2.975	2.7839	.93573	2.968	2.9898	1.0073	598.2	620.49	1.0373
10	24,000	24,000	1.0000	2.184	2.1383	.97908	2.956	3.0742	1.0400	391.0	439.51	1.1241
11	24,000	24,007	1.0003	1.560	1.3483	.86429	2.807	2.8457	1.0138	493.0	514.17	1.0429
12	24,000	24,000	1.0000	1.4159	1.2090	.85387	3.1545	3.2575	1.0327	460.76	511.88	1.11095
13	24,000	24,000	1.0000	.750	Non-existent		3.356	3.4543	1.0293	539.0	597.10	1.1078

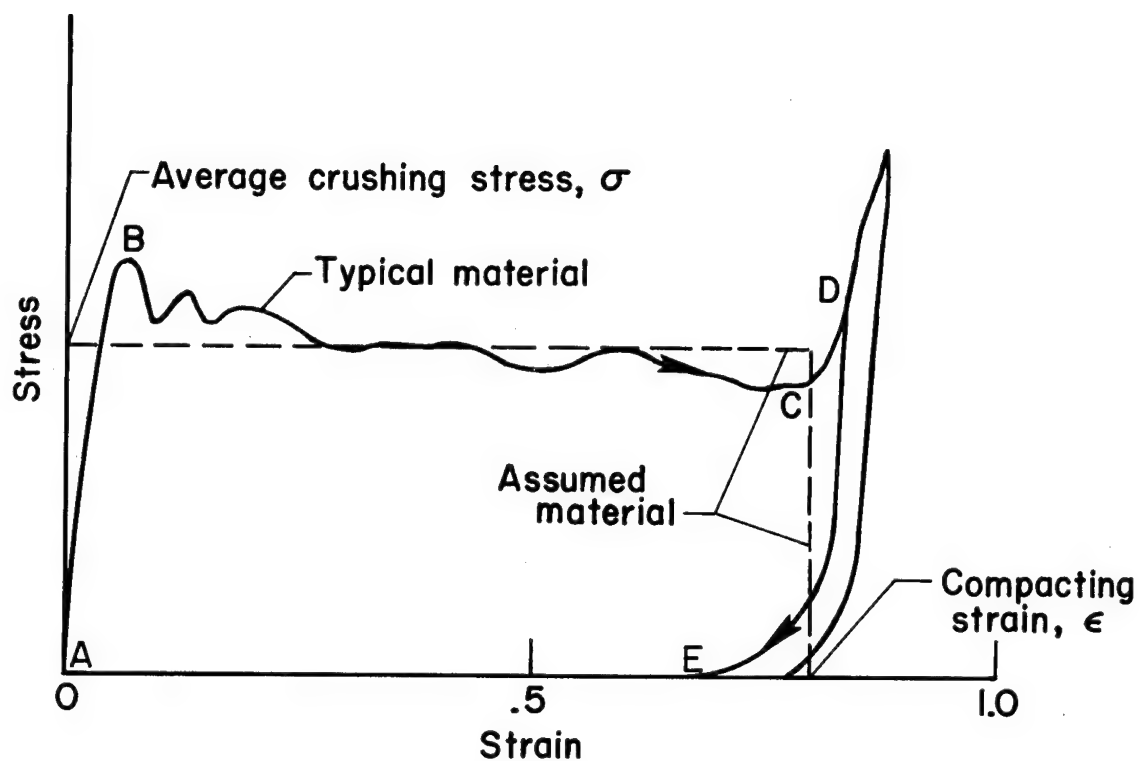
Case	$W_{co} + W_{po}$, lb			L/R		
	Simplified (b)	Detailed (c)	Detailed Simplified	Simplified (b)	Detailed (c)	Detailed Simplified
8	779.0	828.00	1.0629	0.000886	-.000162	-.183
9	1048.2	1070.5	1.0213	-.001042	.000172	-.165
10	841.0	889.51	1.0577	-.000525	-.000063	.12
11	943.0	964.17	1.0224	-.000033	.000290	-8.79
12	910.76	961.88	1.0561	.000329	-.000057	-.17
13	989.0	1047.1	1.0587	-.000329	.000383	-1.16

(a) H = honeycomb-like; B = balsalike.

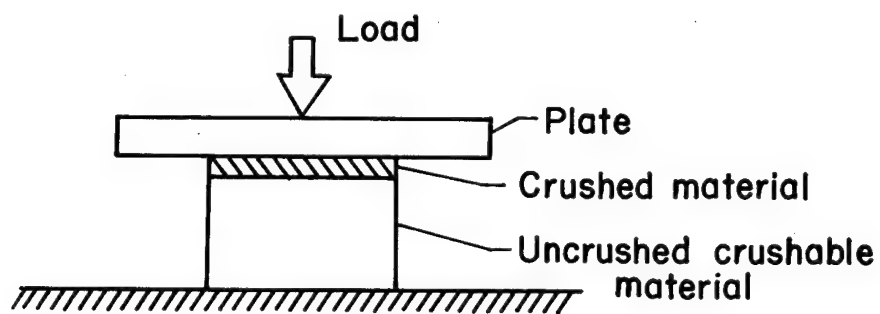
(b) Design by simplified model employing figures 5-12 (except for cases 7 and 12 and the L/R column, which are machine computer results for simplified model) and assuming $\rho_{ck} = 0$, $\epsilon_k = 1$, $F_{po}(e) = 1$, and $g = 0$.

(c) Design by detailed model employing IBM 7094 solution of equations for $\rho_{ck} = \rho_{cm}$, $\epsilon_k = \epsilon_m$, $F_{po}(e) = 2 \int_0^1 \frac{(e_s + 1)s_p ds_p}{\sqrt{2e_s p + e^2 + 1}}$.

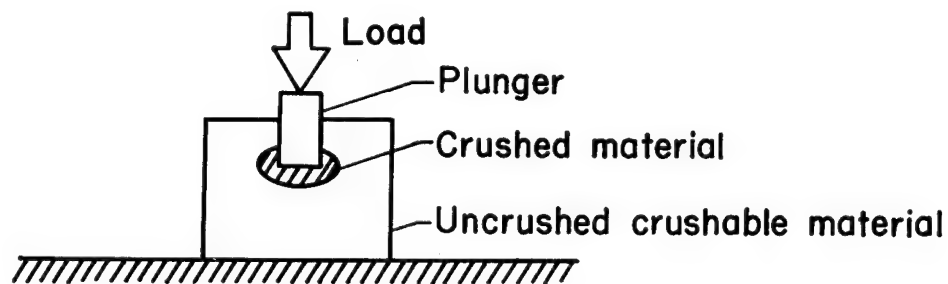
(d) Over a hypothetical stroke as large as the outer radius, there is no force developed which is large enough to cause penetration.



(a) Stress-strain curves.



(b) Crushing test with plate.

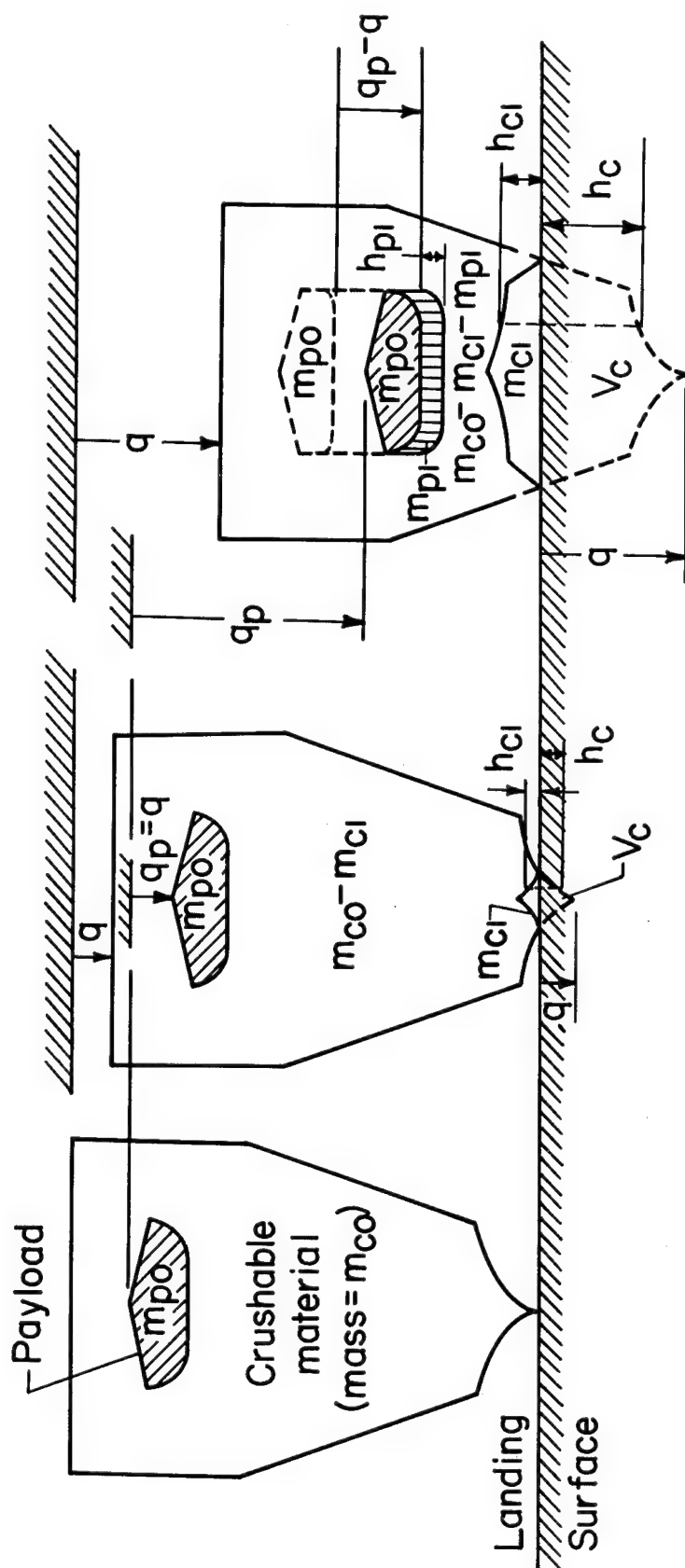


(c) Crushing test with plunger.

Figure 1.- Typical stress-strain curves and crushing tests.

(a) At the start of impact. (b) During impact, before payload penetration. (c) During impact, after payload penetration.

Figure 2.- General vertically symmetrical landing geometry for zero shear resistance.



(a) At the start of impact.

(b) During impact, before payload penetration.

(c) During impact, after payload penetration.

Figure 3.- General vertically symmetrical landing geometry for zero shear resistance and uniform compacting strain.

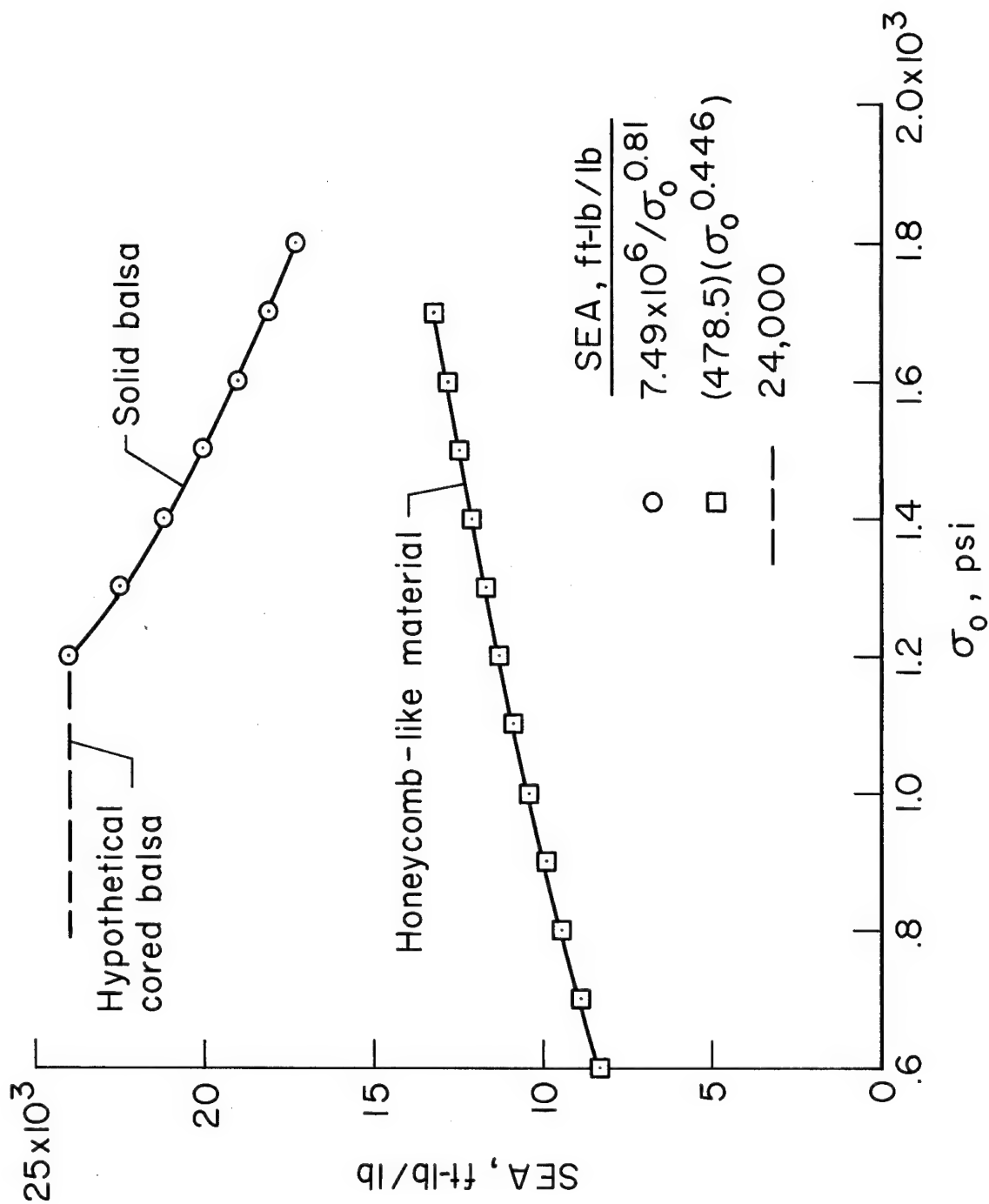


Figure 5.- SEA (for $\epsilon_m = 0.8$) vs σ_o for selected materials.

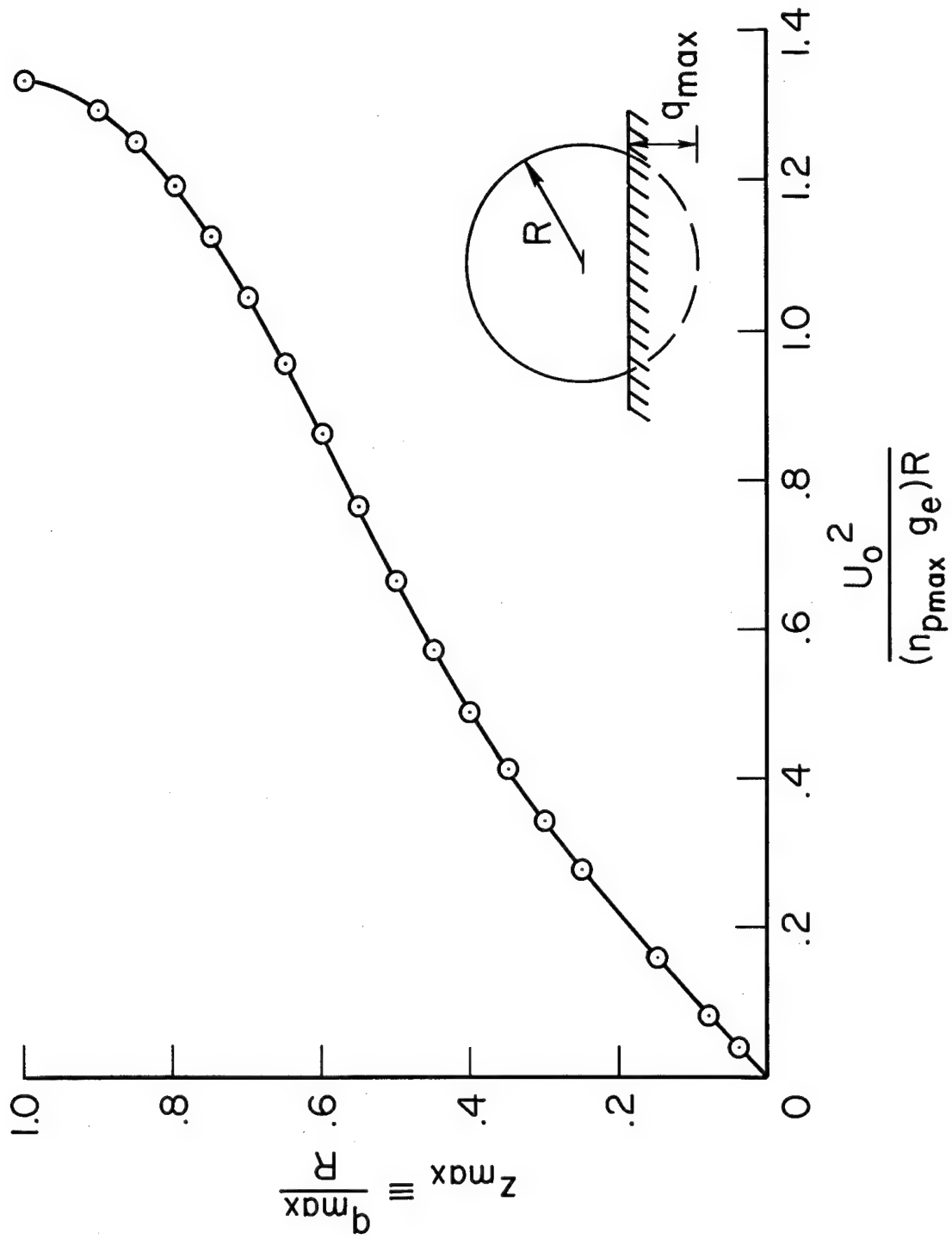


Figure 6.- Stroke design chart for simplified model without penetration when R is given.

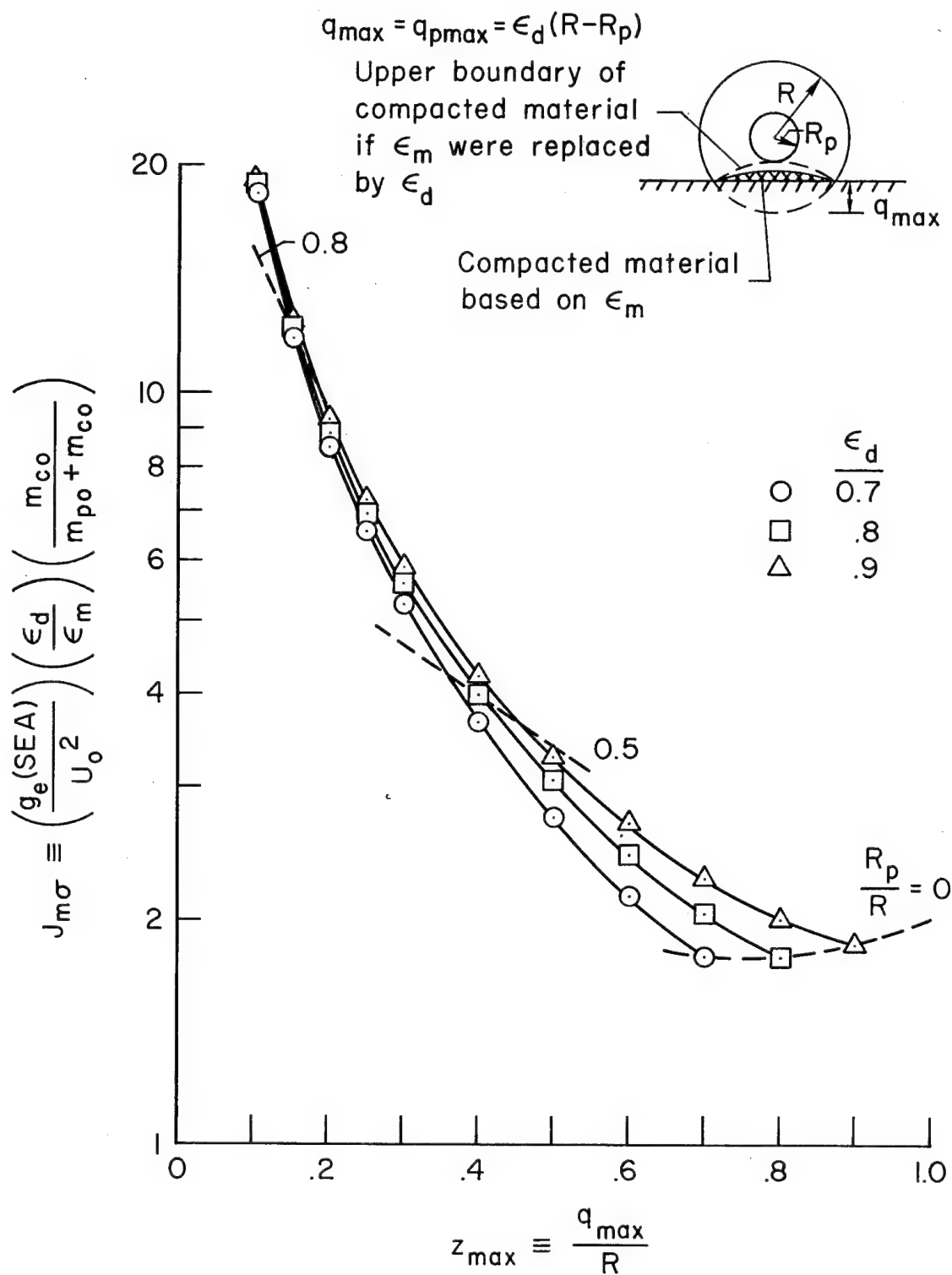


Figure 7.- Mass design chart for simplified model without penetration when R is given.

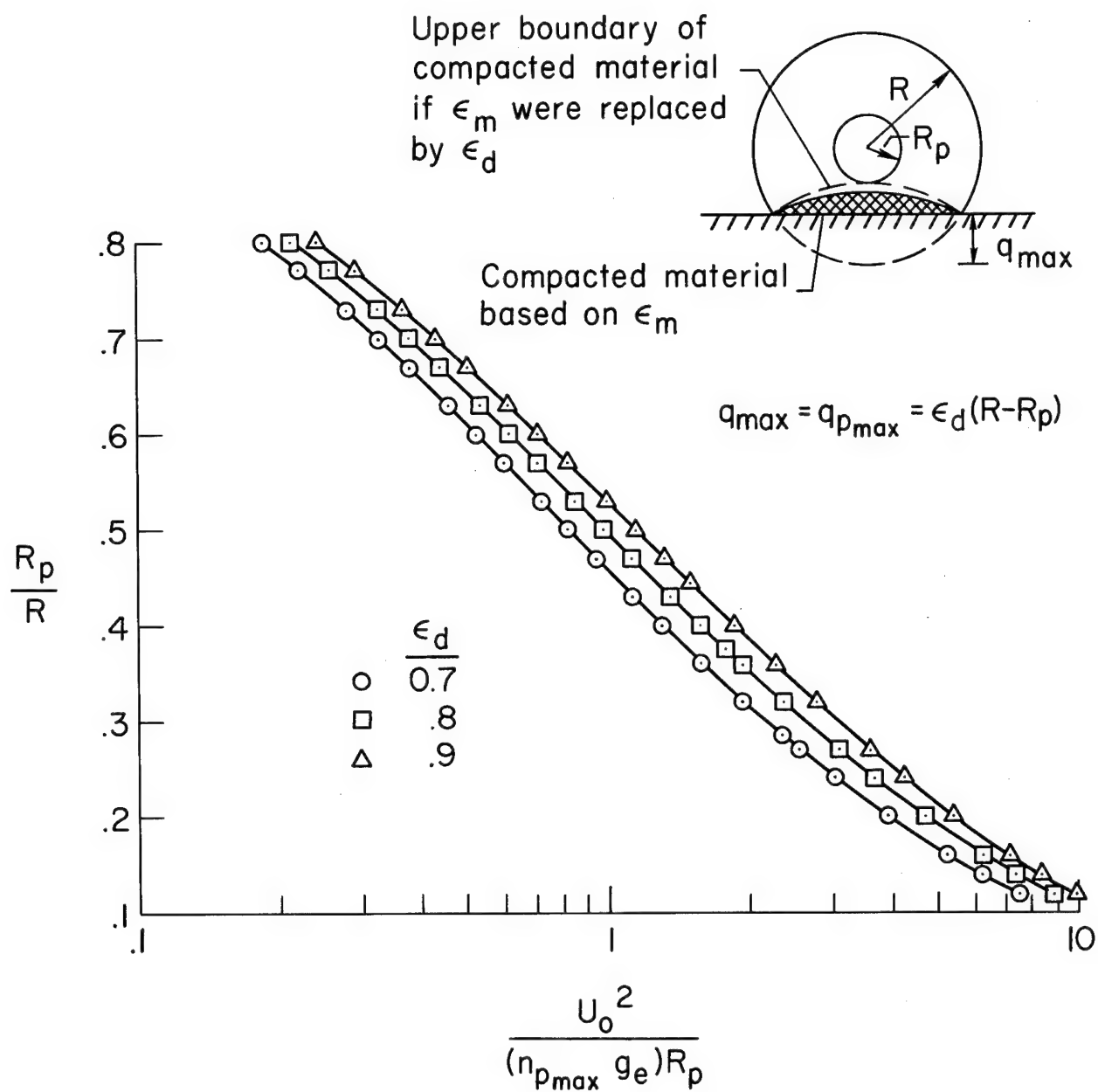


Figure 8.- Radius ratio design chart for simplified model without penetration when R_p is given.

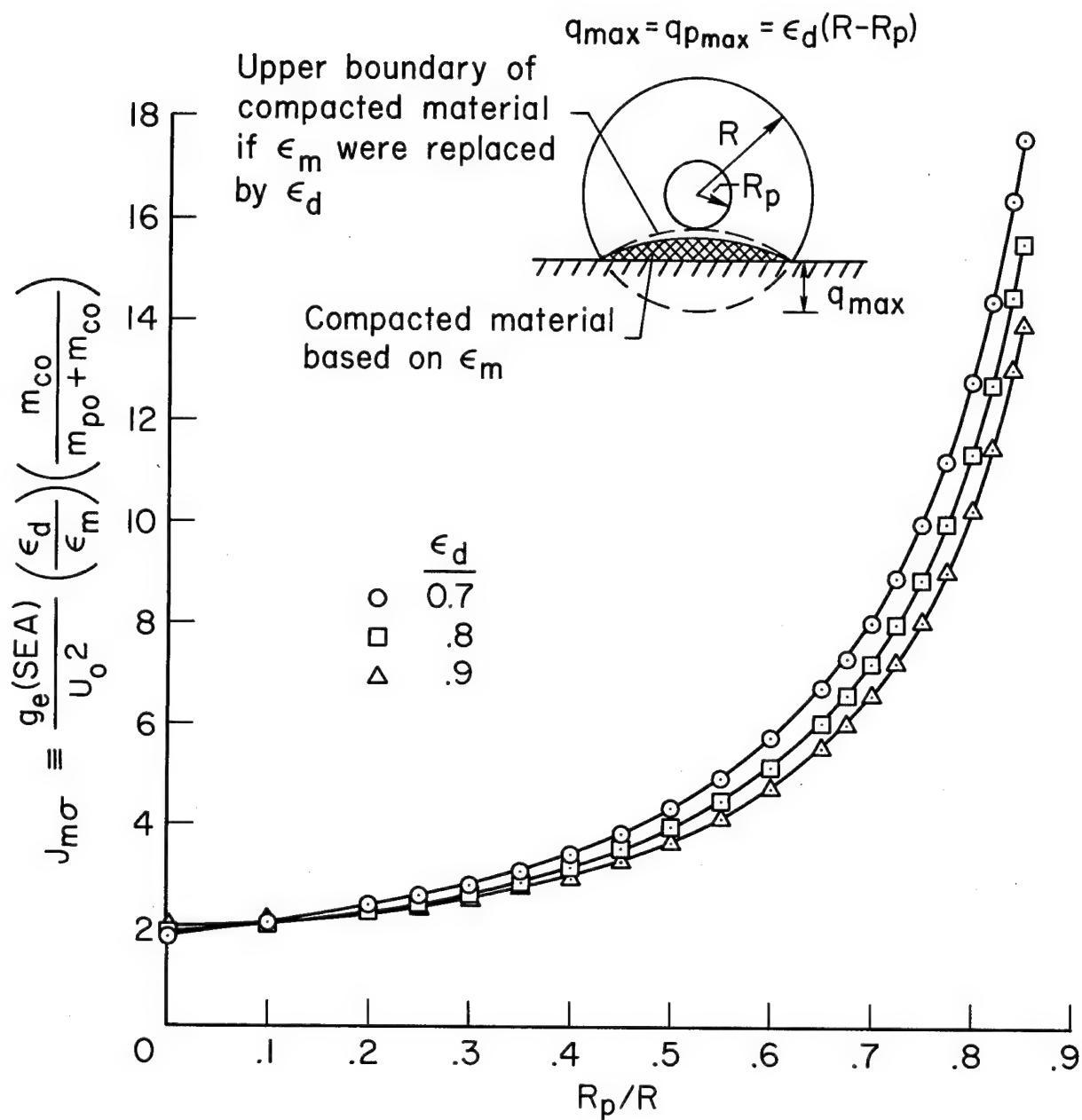


Figure 9.- Mass design chart for simplified model without penetration when R_p is given.

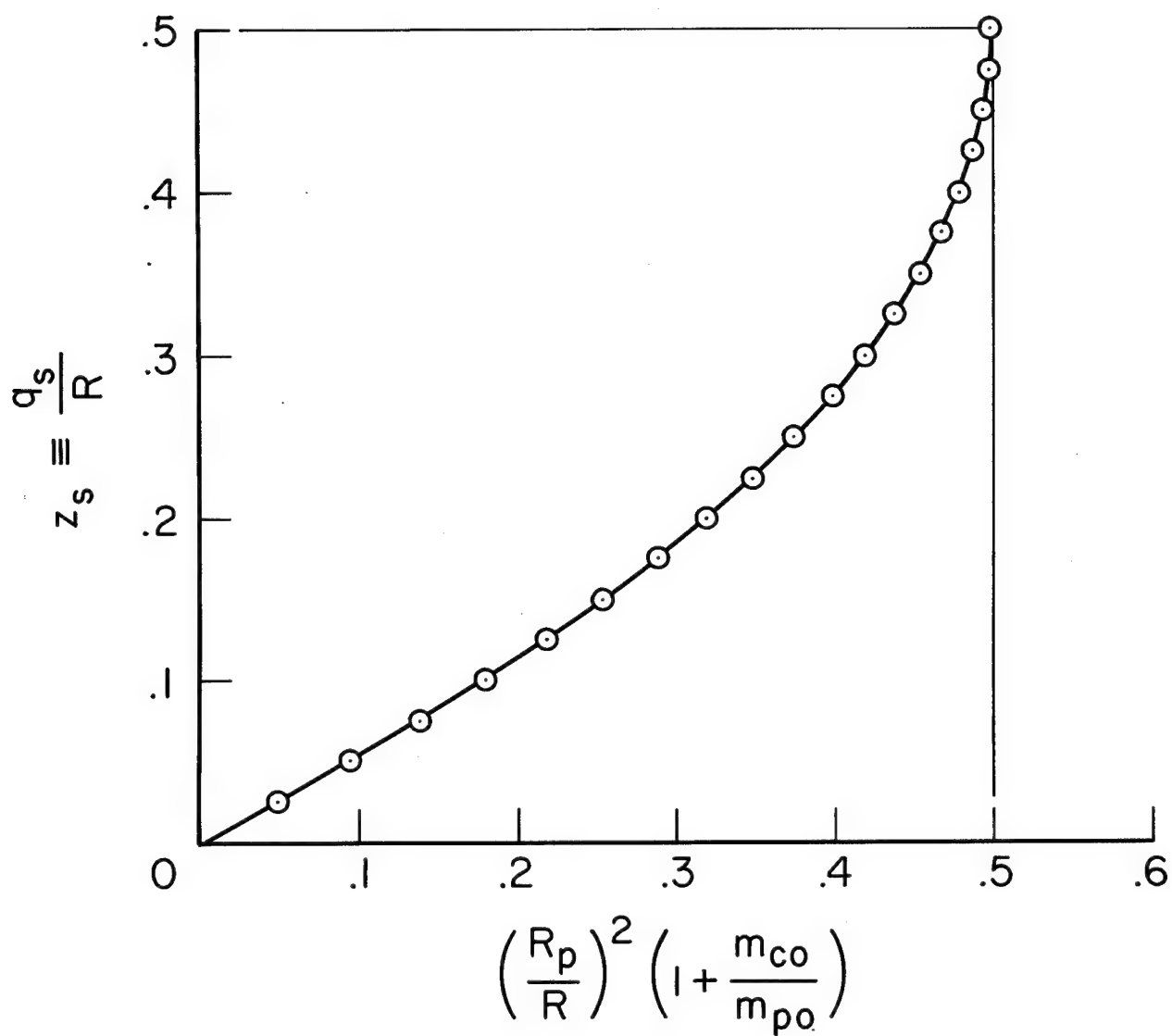


Figure 10.- Dimensionless stroke at which penetration begins for simplified model without bonding.

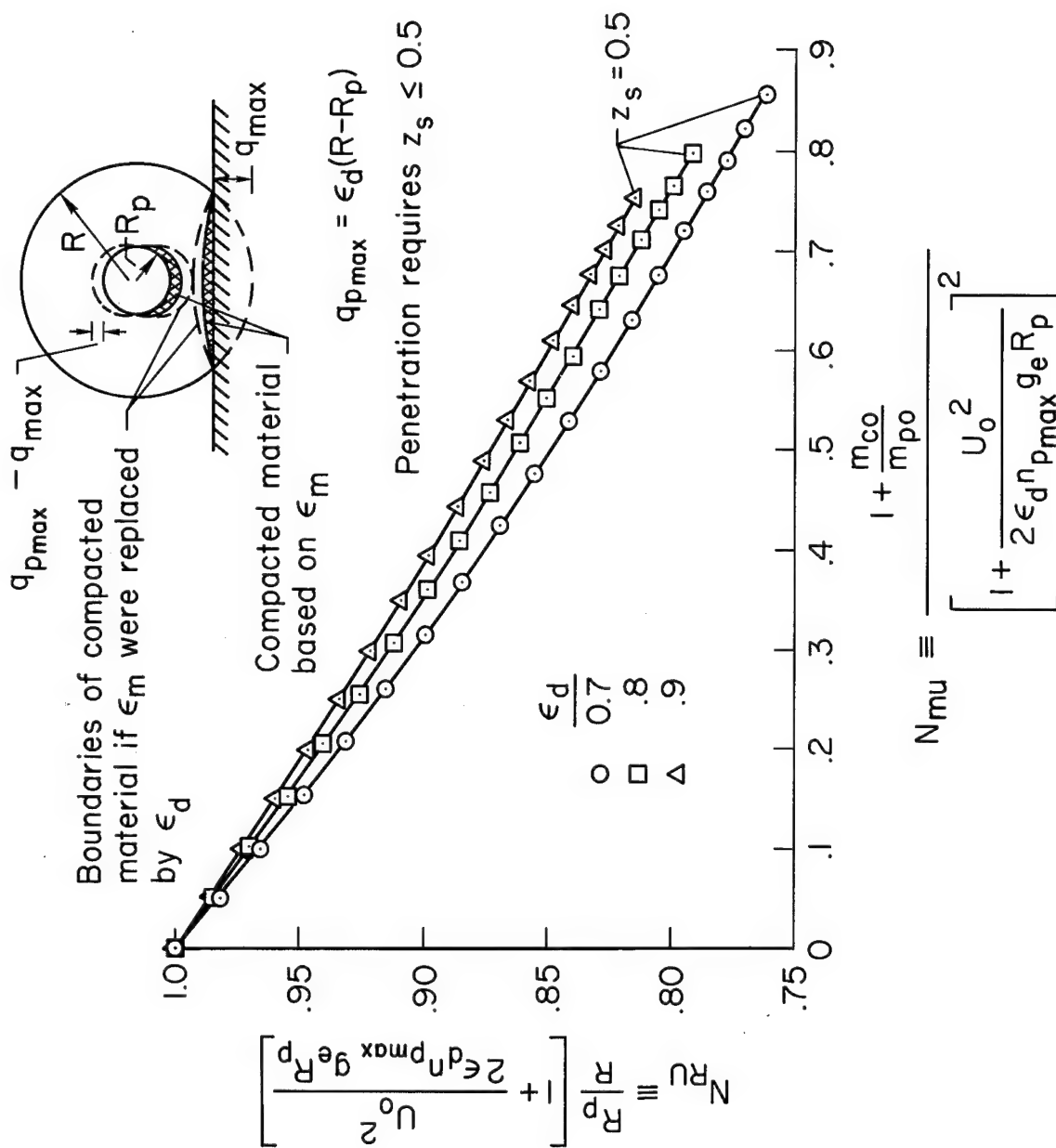


Figure 11.- Mass and radius ratio design chart for simplified model with penetration when R_p is given.

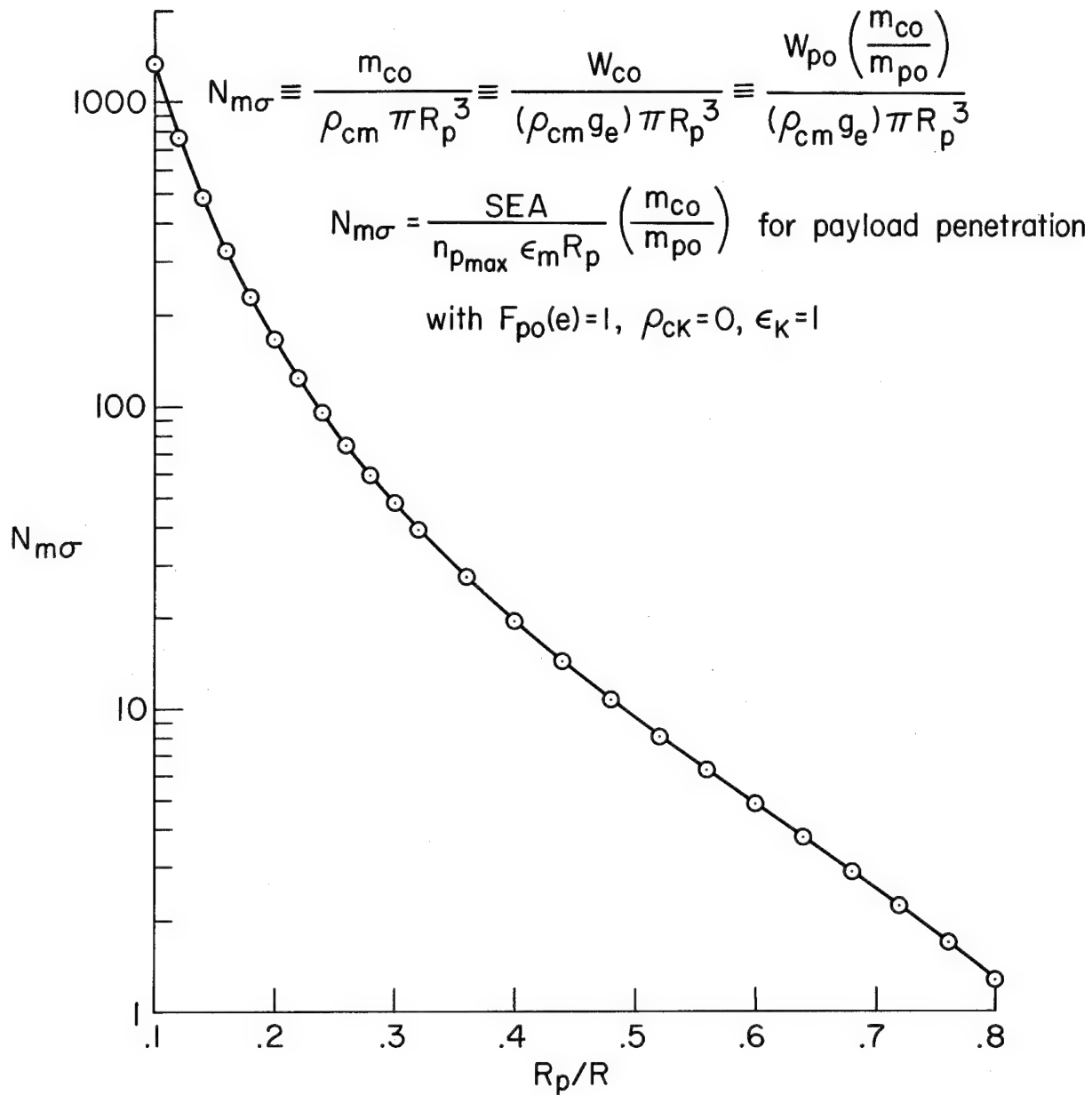


Figure 12.- Mass design chart for simplified model with penetration when R_p is given; also simple mass-volume relation.

Honeycomb-like material

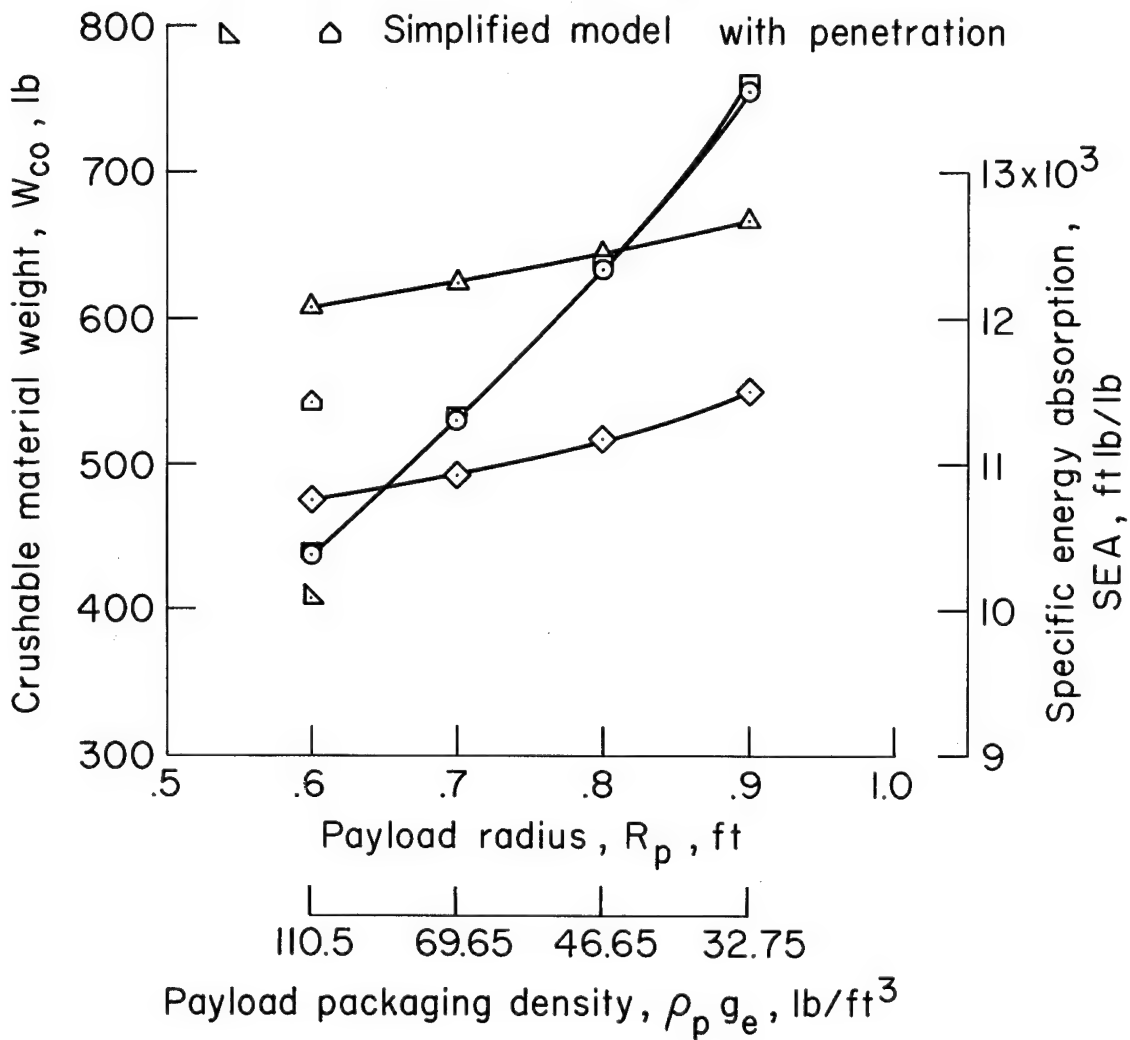
$$W_{po} = 100 \text{ lb} \quad \epsilon_m = 0.8$$

$$n_{pmax} = 2000 \quad \epsilon_d = 0.7$$

$$U_o = 300 \text{ ft/sec}$$

W_{co} SEA

- | | | | |
|---|---|------------------|-----------------------|
| ○ | ◇ | Simplified model | } without penetration |
| □ | △ | Detailed model | |
| ▽ | △ | Simplified model | with penetration |

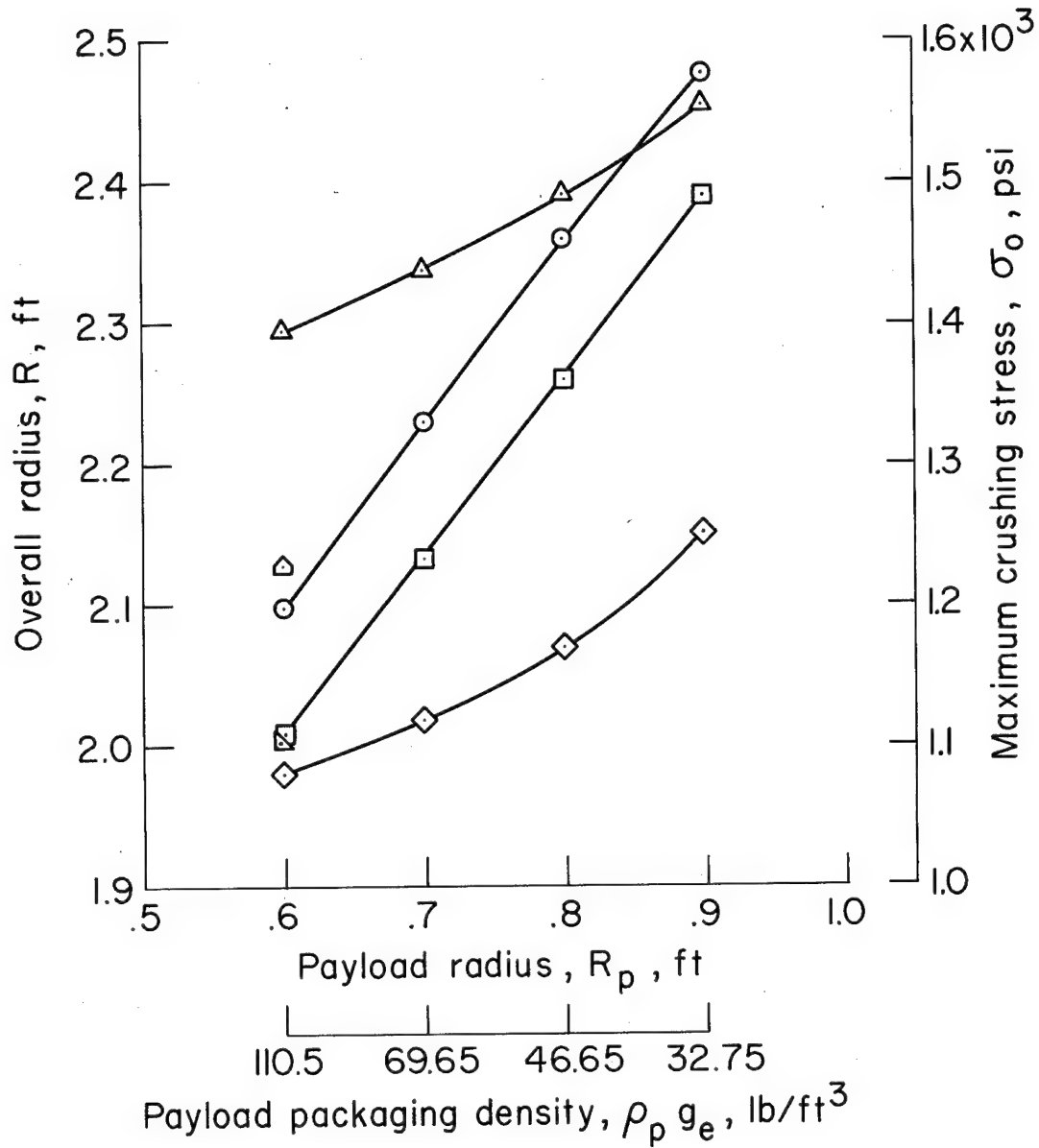


(a) W_{co} and SEA

Figure 13.- Crushable casing properties and performance as functions of R_p and ρ_{pge} for honeycomb-like material, a payload weight of 100 lb, and a payload maximum load factor of 2000.

See part (a) for design conditions

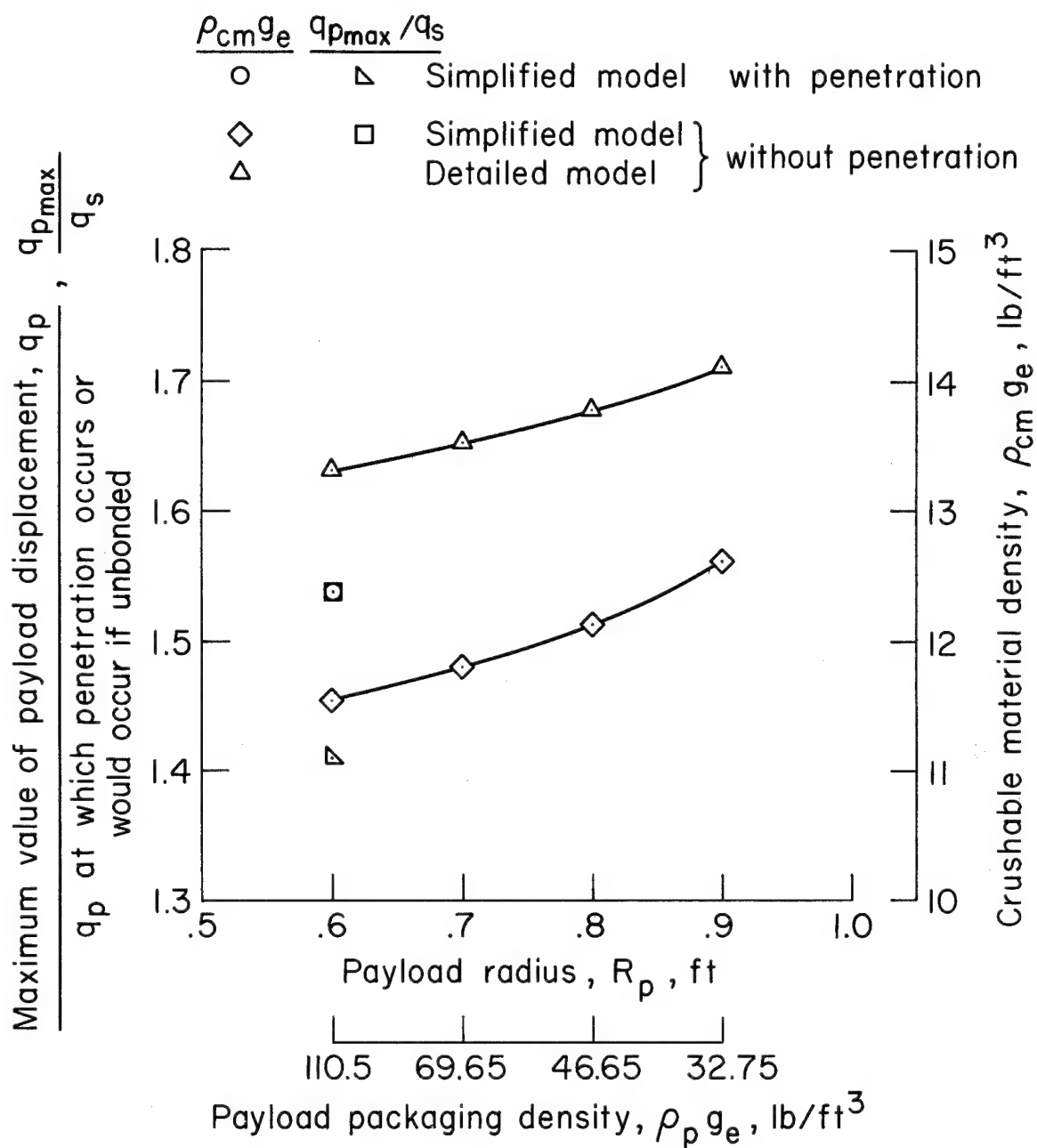
$\frac{R}{\sigma_0}$		
\circ	\diamond	Simplified model
\square	\triangle	Detailed model
\triangleleft	\triangleright	Simplified model
		without penetration
		with penetration



(b) R and σ_0

Figure 13.- Continued.

See part (a) for design conditions



(c) q_{pmax}/q_s and $\rho_{cm} g_e$

Figure 13.- Concluded.

Balsa-like material

$$W_{po} = 450 \text{ lb}$$

$$\epsilon_m = 0.8$$

$$SEA = 24,000 \text{ ft lb / lb}$$

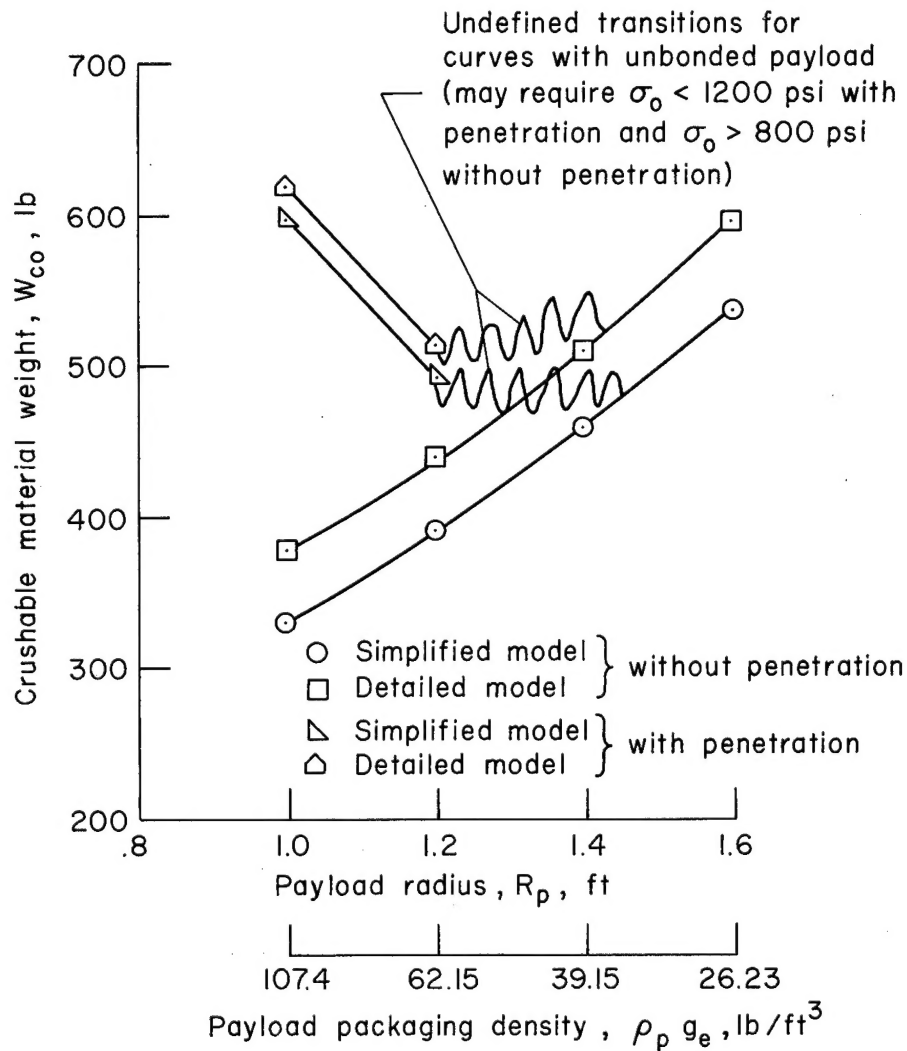
$$\epsilon_d = 0.7$$

$$U_o = 300 \text{ ft/sec}$$

$$\eta_{pmax} \leq 2000$$

$$\left. \begin{array}{l} \sigma_o = 800 \text{ psi} \\ \rho_{cm} g_e = 3.84 \text{ lb/ft}^3 \end{array} \right\} \text{without penetration}$$

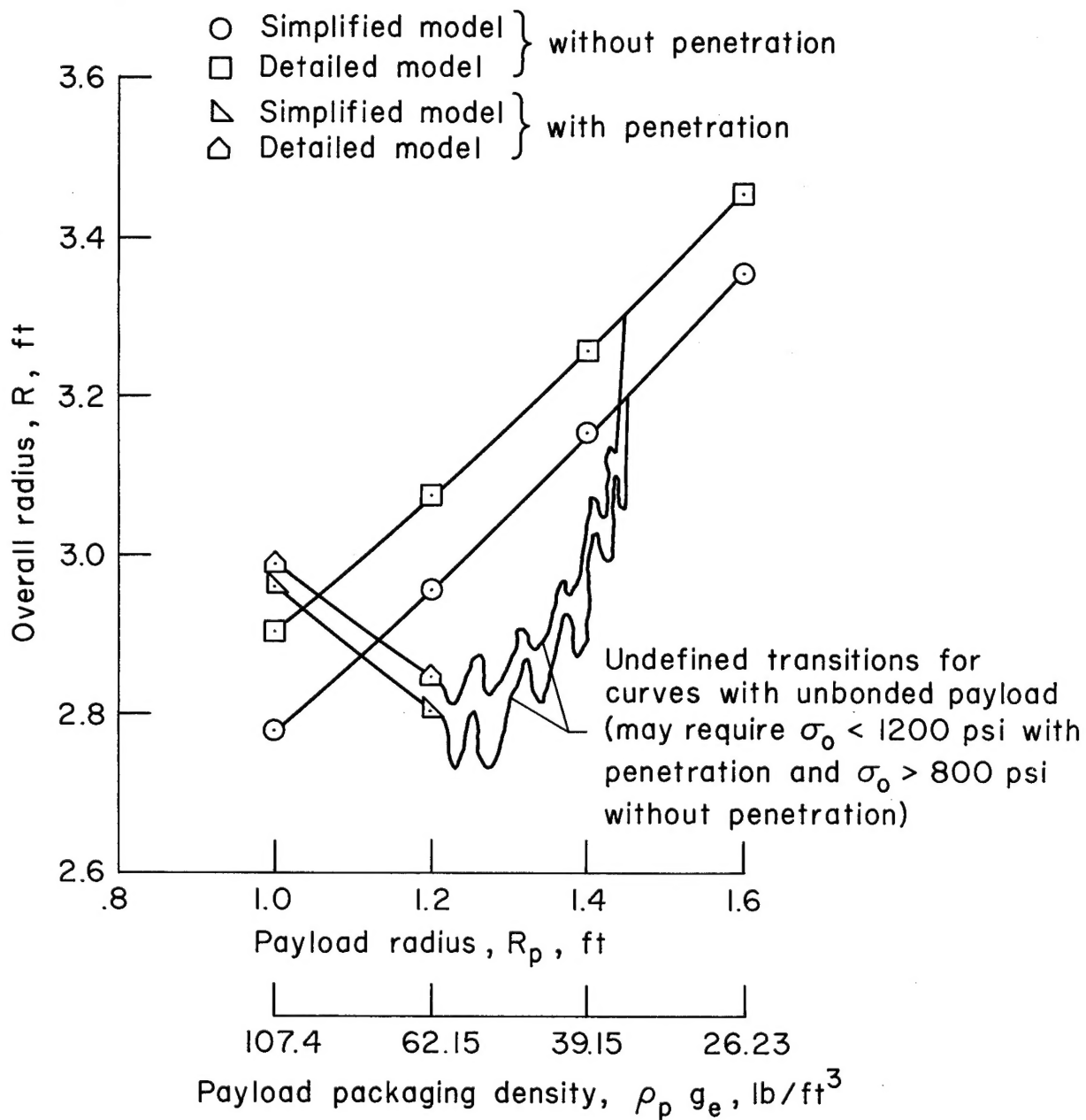
$$\left. \begin{array}{l} \sigma_o = 1200 \text{ psi} \\ \rho_{cm} g_e = 5.76 \text{ lb/ft}^3 \end{array} \right\} \text{with penetration}$$



(a) W_{co}

Figure 14.- Crushable casing properties and performance as functions of R_p and $\rho_p g_e$ for balsa-like material and a payload weight of 450 lb.

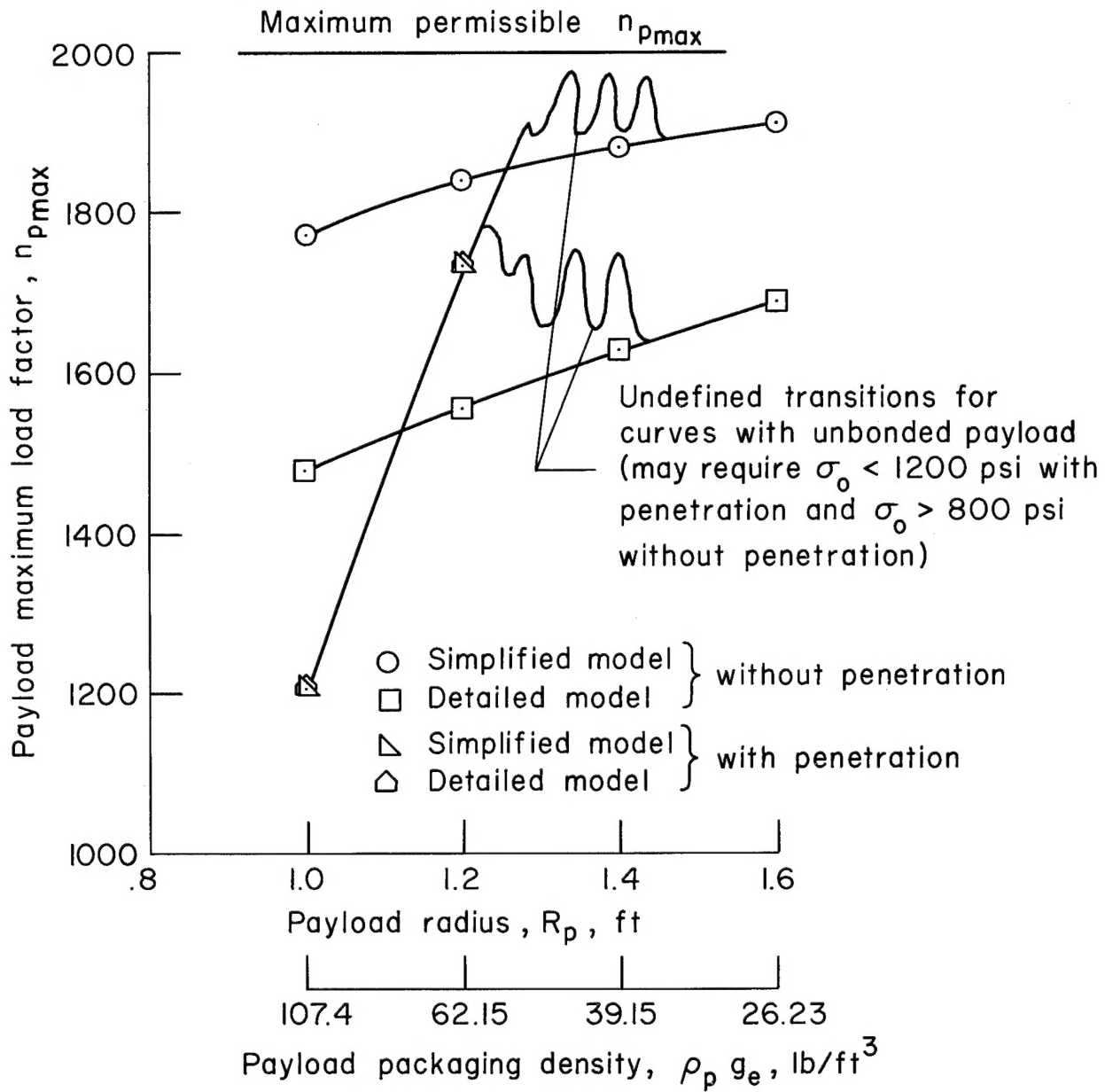
See part (a) for design conditions



(b) R

Figure 14.- Continued.

See part (a) for design conditions

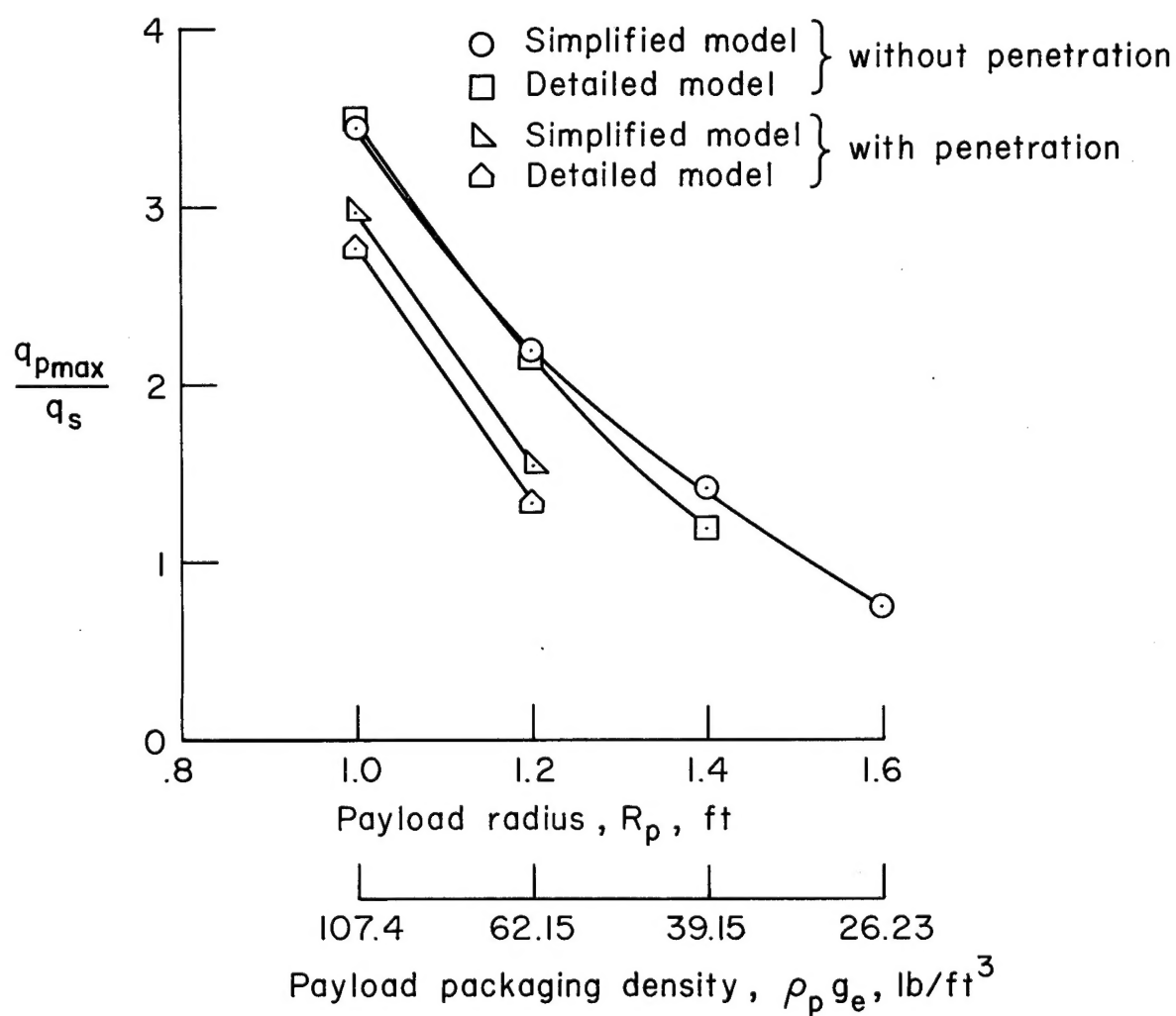


(c) n_{pmax}

Figure 14.- Continued.

See part (a) for design conditions

$$\frac{q_{p\max}}{q_s} = \frac{\text{Maximum value of payload displacement, } q_p}{q_p \text{ at which penetration occurs or would occur if unbonded}}$$



(d) $q_{p\max}/q_s$

Figure 14.- Concluded.